ROLE OF INTERFACES ON SEVERE PLASTIC DEFORMATION AND HE-IRRADIATION TOLERANCE IN CU-NB NANOCOMPOSITES

BY

TIMOTHY GERALD LACH

DISSERTATION

Submitted in partial fulfillment of the requirements
for the degree of Doctor of Philosophy in Materials Science and Engineering
in the Graduate College of the
University of Illinois at Urbana-Champaign, 2016

Urbana, Illinois

Doctoral Committee:

Professor Pascal Bellon, Chair
Professor Robert S. Averback
Assistant Professor Shen J. Dillon
Professor James Stubbins

ABSTRACT

Interface structure in immiscible metal nanocomposites plays a key role in deformation tolerance and radiation damage tolerance. Interface structure, just like microstructure, can vary within the same material system depending on the processing route; the properties of a material can also vary depending on the interface structure. The role of interface structure on the tolerance to severe plastic deformation in Cu-Nb nanocomposites was investigated by comparing the microstructural evolution after high pressure torsion (HPT) of multilayer nanocomposites grown by physical vapor deposition (PVD) with low shear strength interfaces and fabricated by accumulative roll bonding (ARB) with high shear strength interfaces. And the role of interface structure on the trapping of He was studied by comparing He-bubble formation in nano-multilayers grown by PVD, nanolaminates fabricated by ARB, and three-dimensional nanocomposites obtained by high pressure torsion (HPT); each of these has a different preferred orientation relationship.

The stability of PVD-grown multilayers when subjected to HPT is significantly better to high shear strain than the ARB-fabricated multilayers. The PVD-grown multilayers remain largely stable up to a strain of ~81 and still have regions of multilayers at a strain of ~357 before transforming to a 3D nanocomposite by a strain of ~685; the ARB multilayer composites meanwhile become unstable at shear strain of ~10 and completely transform to a 3D interconnected composite at a strain of ~278. The mechanisms for deformation depend on the interface character; the PVD-grown material with low shear strength interfaces deform by interfacial sliding while the ARB-fabricated material deforms by dislocation glide across the interface. In both layered systems, there is kink and shear banding of layers at higher shear strain that changes the local orientation of layers relative to the shear direction resulting in a route to transition to a 3D nanocomposite structure.

Likewise under He-ion irradiation, the critical He dose per unit interfacial area for bubble formation was largest for the PVD multilayers, lower by a factor of ~1.4 in the HPT nanocomposites annealed at 500 ˚C, and lower by a factor of ~4.6 in the ARB nanolaminates relative to the PVD multilayers. The high concentration of free volume at interfaces in PVD-grown multilayers is excellent for trapping He atoms and point defects, and the amount of trapped He at the interface scales with interface area density. A combination of efficient interfaces and high density of interfaces is ideal for trapping He atoms and point defects.

The results of both high shear strain using HPT and He implantation indicate that the (111)FCC||(110)BCC Kurdjumov-Sachs (KS), or {111}KS, interfaces predominant in PVD provide more effective traps for both point and line defects than the {112}KS interfaces predominant in ARB nanolaminates. The steady-state microstructural stability, good trapping efficiency, and high interface area of 3D structures processed by severe plastic deformation make them most attractive for structural applications such as nuclear energy.

ACKNOWLEDGEMENTS

Graduate school is a long and arduous adventure with many difficulties, but achieving the goal of graduating with a doctoral degree can be achieved with hard work, perseverance, and help from many people. I would like to extend my upmost gratitude to my adviser, Prof. Pascal Bellon, and co-adviser, Prof. Robert S. Averback. They have helped me as advisers, mentors, and collaborators. With their insight and knowledge, they have helped me weave my way through graduate school and my research to make this dissertation a possibility. I would also like to thank and acknowledge my other dissertation committee members, Prof. Shen Dillon and Prof. James Stubbins, for their contributions to this dissertation and my prior preliminary examination.

I would also like to thank my collaborators at Los Alamos National Laboratory, Northwestern University, and Karlsruhe Institute of Technology, especially Dr. Amit Misra, Dr. Nathan Mara, and Dr. Irene Beyerlein at LANL, Dr. Dieter Isheim at NU, and Dr. Julia Ivanisenko at KIT. They have provided valuable insights and helped conduct experiments that made the research I have taken possible.

I must also thank the staff at the FS-Material Research Lab for assisting me with all aspects of my research and for making life in the MRL much easier. In particular, I am thankful for the help and guidance of Doug Jeffers, Dr. Mauro Sardela, Dr. Wacek Sweich, Dr. James Mabon, and Dr. Matthew Bresin.

I thank all the group members that accompanied me on my adventure through graduate school. Being able to bounce both ideas for research and ideas for having a great time and making it through the grind that grad school made my experience in grad school a great one. In particular, I would like to thank Dr. Elvan Ekiz-Stumphy, Dr. Miao Wang, and Dr. Salman Arshad. Our research collaborations ultimately pushed me forward on my research efforts; Elvan in particular

was extremely beneficial in her help on analyzing XRD and texture measurements. I would also like to thank the past and current group members that were most important to my work and my time in graduate school: Dr. Brad Stumphy, Dr. Shipeng Shu, Dr. Sezer Ozerinc, Dr. Nhon Vo, Dr. Xuan Zhang, Dr. Fuzeng Ren, Calvin Lear, Jae Yel Lee, John Beach, Sung Eun Kim, Dr. Madhavan Radhakrishnan, and Rannesh Lokesh. I count them not just as colleagues but also friends.

I would like to thank the multitude of friends I have gained while in graduate school both within the Illinois MatSE department and outside the department. They have brought great joy to my time in Champaign-Urbana.

Finally I would like to thank my family: my brother Tommy, my sister Julie, my mom Kathy, and my dad Tom. They have all been a beacon of great inspiration and support my entire life. My dad, who passed many years ago, was the one who inspired me to work to improve the world. He is a big reason I chose to study materials science and engineering and work on materials for clean energy applications.

Correspondence with the author can be made via e-mail at tlach2@illinois.edu or timothy.lach@gmail.com.

TABLE OF CONTENTS

CHAPTER 1

INTRODUCTION

Next generation fission and fusion nuclear power plants are being designed to improve and replace current nuclear power plants to produce electricity more effectively, efficiently, and cleanly than current nuclear and fossil fuel power plants. Compared to current generation II-III reactor designs, future generation IV fission and fusion reactor designs will operate at much higher temperatures and radiation damage levels, see Fig. 1.1; many of these designs require materials to withstand up to double the temperature (in Kelvin) and up to four times as much irradiation dose as current reactor designs [1]. In any reactor environment, material is bombarded by energetic particles such as neutrons, ions, and other fission products which create a multitude of defects such as those in Fig. 1.2 that can be deleterious to mechanical properties of the material [2, 3]. These defects are created by high energy collision cascades created by neutrons and heavy elements and/or by the supersaturation of point defects, such as interstitial and vacancy pairs and impurity elements, which can promote solute segregation, grain growth, void growth, and boundary de-cohesion among other microstructural changes within component materials that could lead to component failure [4-7].

To maintain the desired mechanical properties and prevent component failure, the defects that are created must be reduced in number and size or prevented from forming. A particularly intriguing way of maintaining these excellent properties is potentially achieved by processing materials to a fine scale – tens of nanometers or less – thus, creating a material with a high density of interfaces via grain and phase boundaries which can serve as sinks for point defects, He atoms, and dislocations [8-10]. This considerably reduces the distance for defects to migrate to sinks

where they are annihilated by recombination in the case of vacancies and interstitial atoms, or are trapped or prevented from moving further in the case of impurity atoms and dislocations [11, 12].

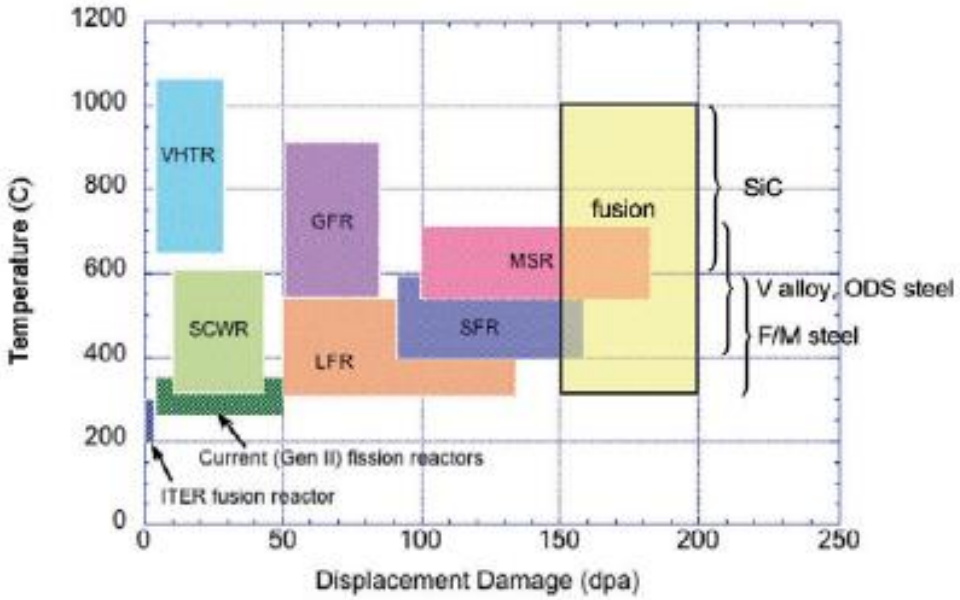

Fig. 1.1: Overview of temperature and operating displacement damage dose for various fusion and fission reactor designs [1]

Most metals, however, are unable to retain this fine scale microstructure because it is energetically favorable for a material to have a coarse-grained microstructure relative to a fine-grained microstructure due to the excess free energy associated with grain boundaries [13]. This is true for many materials used at high temperatures without irradiation conditions, but it is a bigger problem during irradiation as irradiation accelerates grain growth due to an increase in the density of point defects [14, 15]. Therefore, material systems are being developed that can prevent or limit grain growth while still serving as efficient sinks for defects [16-19].

One strategy for combining coarsening resistance and radiation resistance is through the formation of a fine distribution of nanoscale oxycarbonitride precipitates that pin grain boundaries and serve as good sinks for defects, such as in oxide dispersion strengthened (ODS) steels [20-22]. Studies done with ferritic/ martensitic steels containing a fine dispersion of nano-scale oxide particles have shown that the incoherent oxide/ metal interfaces serve as good sinks for point

defects [23, 24]. These steels have high strength, high thermal stability, and high radiation resistance making them potentially very useful in many future reactor components [25, 26]. Their complexity in microstructure, chemistry, and processing, however, makes it difficult to study the underlying mechanisms for radiation and deformation resistance. Another strategy for radiation resistance is processing the material as a single crystal with coherent ordered precipitates, such as in Ni-based superalloys [27-29]. For ordered, coherent precipitates in a matrix, such as gamma-prime Ni_3Al in a gamma Ni-Al matrix, radiation resistance has strong temperature dependence; at low temperatures, radiation-induced disordering is highly prevalent and dominates over thermal re-ordering, and the opposite is true at high temperatures, where thermal re-ordering allows for ordered precipitates to remain stable or grow [28]. The self-organization of ordered alloys is related to the self-organization of immiscible metals during ion irradiation and severe plastic deformation, seen in Cu-based alloy systems such as Cu-V, Cu-Ag, and Cu-Fe [30, 31]. The defect sink efficiency of these ordering-disordering materials may be limited by the coherency of the interface and temperature-dependent stability. Research on the processing and radiation resistance of these two material systems, ODS alloys and ordering-disordering materials is ongoing, but the mechanisms for the behavior of these materials under severe plastic deformation and ion/ neutron radiation can be challenging to determine. That leads to a third strategy that utilizes immiscible metal nanocomposites, such as Cu-based binary and ternary alloys systems, to form a high density of efficient interfaces that can remain stable under extreme thermal, mechanical, and radiation conditions; these material systems will be the focus of this dissertation.

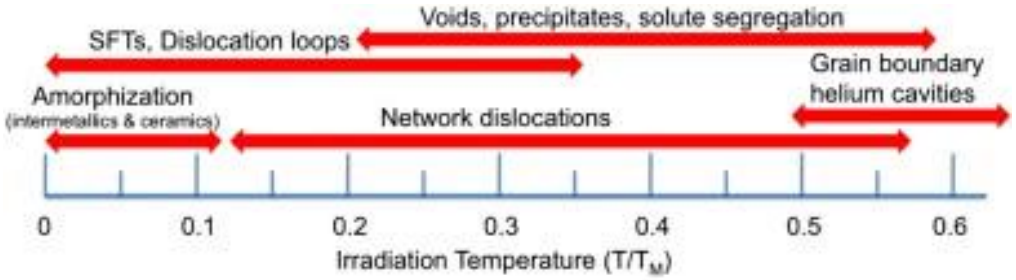

Fig. 1.2: Defect microstructures created in irradiated materials [2]

As such, immiscible binary and ternary alloy systems with semi-coherent interfaces, like Cu-Nb, Cu-V, and Ag-V, are being studied as model systems for resistance to deformation and radiation damage, with favorable results [32-35]. The effects of phase boundary interfaces, however, have not fully been investigated within these materials, and ongoing research aims to elucidate the importance and role that such interfaces play in enhancing deformation and radiation damage resistance. As will be discussed later, two metal composites of the same composition, grain size, and morphology can behave very differently under deformation or particle radiation depending upon the differing character of the interfaces, in that the orientation relationship (OR) between coexisting phases and the interface or habit plane may differ [36]. It is thus important to control the interface character to achieve the best possible properties. Many alloy systems allow for the interface character to be controlled by different means of processing, particularly among materials with semi-coherent or incoherent interfaces, such as those found in the systems of face-centered cubic (FCC) and body-centered cubic (BCC) phases. Cu-Nb is a model system for this class of materials [37]. In this dissertation, the dependence of interface character on both radiation resistance and plastic deformation tolerance in the Cu-Nb system has been investigated. First, by investigating how multilayer nanocomposites deform under large shear strain, and how this deformation depends on the interface character between layers. Second, by demonstrating experimentally that these materials exhibit resistance to bubble and void growth via trapping of helium atoms into 1-2 nm bubbles at interfaces, and how this trapping ability depends on the

trapping efficiency of interfaces as well as the density of those interfaces. This research will be discussed in detail in the Chapters 4 and 5 of this dissertation. Prior to these results chapters, a background chapter synthesizes the previous works that are relevant to the research undertaken in this dissertation. Following the background is a detailed description of the methods and procedures used to produce the results and should allow an experienced researcher to reproduce the results.

1.1: References

[1] S.J. Zinkle and J.T. Busby. Materials Today 12 (2009) 12.

[2] S.J. Zinkle, J.P. Blanchard, R.W. Callis, C.E. Kessel, R.J. Kurtz, P.J. Lee, K.A. McCarthy, N.B. Morley, F. Najmabadi, R.E. Nygren, G.R. Tynan, D.G. Whyte, R.S. Willms, and B.D. Wirth. Fusion Engineering and Design 89 (2014) 1579.

[3] S.J. Zinkle and L.L. Snead. The Annual Review of Materials Research 44 (2014) 241.

[4] K.Y. Yu, Y. Liu, C. Sun, H. Wang, L. Shao, E.G. Fu, X. Zhang. Journal of Nuclear Materials 425 (2012) 140.

[5] P.J. Maziasz. Journal of Nuclear Materials 205 (1993) 118.

[6] S.J. Zinkle, P.J. Maziasz, and R.E. Stoller. Journal of Nuclear Materials 206 (1993) 266.

[7] P.J. Maziasz. Journal of Nuclear Materials 200 (1993) 90.

[8] T. Hochbauer, A. Misra, K. Hattar, R.G. Hoagland. Journal of Applied Physics 98 (2005) 123516.

[9] W. Han, E.G. Fu, M.J. Demkowicz, Y. Wang, and A. Misra. Journal of Materials Research 28 (2013) 2763.

[10] X. Zhang, N. Li, O. Anderoglu, H. Wang, J.G. Swadener, T. Hochbauer, A. Misra, and R.G. Hoagland. Nuclear Instruments and Methods in Physics Research B 261 (2007) 1129.

[11] M.J. Demkowicz and L. Thilly. Acta Materialia 59 (2011) 7744.

[12] A. Misra, M.J. Demkowicz, X. Zhang, and R.G. Hoagland. Journal of Materials (2007) 62.

[13] D.J. Rowenhorst and P.W. Voorhees. The Annual Review of Materials Research 42 (2012) 105.

[14] B. Radiguet, A. Etienne, P. Pareige, X. Sauvage, and R. Valiev. Journal of Materials Science 43 (2008) 7338.

[15] D. Kaoumi, A.T. Motta, and R.C. Birtcher. Journal of Applied Physics 104 (2008) 073525.

[16] G.R. Odette. Journal of Materials 66 (2014) 2427.

[17] J. Brodrick, D.J. Hepburn, and G.J. Ackland. Journal of Nuclear Materials 445 (2014) 291.

[18] G.R. Odette, M.J. Alinger, and B.D. Wirth. The Annual Review of Materials Research 38 (2008) 471.

[19] M.J. Demkowicz, R.G. Hoagland, and J.P. Hirth. Physical Review Letter 100 (2008) 136102.

[20] L. Dai, Y. Liu, and Z. Dong. Powder Technology 217 (2012) 281.

[21] L. Dai, Y. Liu, Z. Ma, Z. Dong, and L. Yu. Journal of Materials Science 48 (2013) 1826.

[22] H.K. Zhang, Z. Yao, Z. Zhou, M. Wang, O. Kaitasov, and M.R. Daymond. Journal of Nuclear Materials 455 (2014) 242.

[23] C. Lu, Z. Lu, R. Xie, C. Liu, L. Wang. Journal of Nuclear Materials 455 (2014) 366.

[24] J. Chen, P. Jung, J. Henry, Y. De Carlan, T. Sauvage, F. Duval, M.F. Barthe, W. Hoffelner. Journal of Nuclear Materials 437 (2013) 432.

[25] S.M. Gonzalez de Vincente, S. Dudarev, and M. Rieth. Fusion Science and Technology 66 (2014) 38.

[26] Y. Miao, K. Mo, Z. Zhou, X. Liu, K.C. Lan, G. Zhang, M.K. Miller, K.A. Powers, Z.G. Mei, J.S. Park, J Almer, and J.F. Stubbins. Materials Science and Engineering A 639 (2015) 585.

[27] Y. Ma and A.J. Ardell. Scripta Materialia 52 (2005) 1335.

[28] H.K. Zhang, Z. Yao, M.A. Kirk, and M.R. Daymond. Metallurgical and Materials Transactions A 45A (2014) 3422.

[29] S.M. Seyyed Aghamiri, H.R. Shahverdi, S. Ukai, N. Oono, K. Taya, S. Miura, S. Hayashi, and T. Okuda. Materials Characterization 100 (2015) 135.

[30] S.W. Chee, B. Stumphy, N.Q. Vo, R.S. Averback, and P. Bellon. Acta Materialia 58 (2010) 4088.

[31] S.N. Arshad, T.G. Lach, M. Pouryazdan, H. Hahn, P. Bellon, S.J. Dillon, and R.S. Averback. Scripta Materialia 68 (2013) 215.

[32] E.G. Fu, A. Misra, H. Wang, L. Shao, X. Zhang. Journal of Nuclear Materials 407 (2010) 178.

[33] Q.M. Wei, N. Li, N.A. Mara, M. Nastasi, A. Misra. Acta Materialia 59 (2011) 6331.

[34] S.N. Arshad, T.G. Lach, J. Ivanisenko, D. Setman, P. Bellon, S.J. Dillon, and R.S. Averback. Journal of Materials Research 30 (2015) 1943.

[35] B. Stumphy, R.S. Averback, and P. Bellon. Journal of Materials Research 30 (2015) 170.

[36] W. Han, M.J. Demkowicz, N.A. Mara, E. Fu, S. Sinha, A.D. Rollett, Y. Wang, J.S. Carpenter, I.J. Beyerlein, and A. Misra. Advanced Materials 25 (2013) 6975.

[37] I.J. Beyerlein, A. Caro, M.J. Demkowicz, N.A. Mara, A. Misra, and B.P. Uberuaga. Materials Today 16 (2013) 443.

CHAPTER 2

BACKGROUND

2.1 Interfacial Character of Immiscible Metal Nanocomposites

Interfaces between grains in single phase metals or between phases in multi-phase materials are well-known to be important to structural stability and mechanical properties in both near and far from equilibrium conditions [1-4]. Grain boundaries promote strengthening by limiting dislocation motion from one grain to the next; thus, reducing grain size is a highly effective means of strengthening, as captured by the Hall-Petch relationship [5]. Boundary strengthening is dependent on the size of the grains or phases, and on the coherency of boundaries and the orientation of grains on either side of boundaries [6]. The coherency of grain boundaries is the degree in which lattice sites match on either side of the boundary and is largely dependent on the relative size of the atoms, the atomic structure, and orientation of the grains or phases. In metallic composites, where the atomic structure between the elements is the same, such as in FCC-FCC bimetals like Cu-Ag and Cu-Ni, the phase boundaries can be highly coherent or fully coherent, even in systems that are immiscible in equilibrium [7]. In these systems, when a stress is applied, dislocation motion across the interface is relatively unimpeded, resulting in intermixing of the two elements; this has been shown both in simulation and experimentally [8-10]. High shear strain through the use of high energy ball milling or high pressure torsion (HPT), when performed at temperatures low enough to suppress thermally activated diffusion, resulted in the formation of a solid solution in the Cu-Ag system, as is seen in Fig. 2.1, where atom probe tomography (APT) reconstructions were used to determine the amount of strain necessary to homogenize an initially heterogeneous alloy [10]. In this case, it was shown that mixing is a result of dislocation motion across the interface and not due to diffusional processes. This is important to note as mechanical

deformation was able to mix the heterogeneous system relatively easily because dislocations were able to move across the interface. This was supported by molecular dynamics simulation of precipitate evolution in a Cu matrix, see Fig. 2.2. After a rather low amount of strain, the Ag particle dissolved and the Ag went fully into solid solution with the Cu matrix [8]. This is not the case, however, in most heterogeneous systems that have multiple phases, such as FCC and BCC phases, that reduce the level of coherency at the boundary; though in a unique case like Cu-Fe, a BCC Fe particle dissolves into a solid solution with the Cu matrix at a higher strain, likely as a result of Fe having a smaller positive heat of mixing with Cu and having an allotrope of FCC phase at high temperature [9].

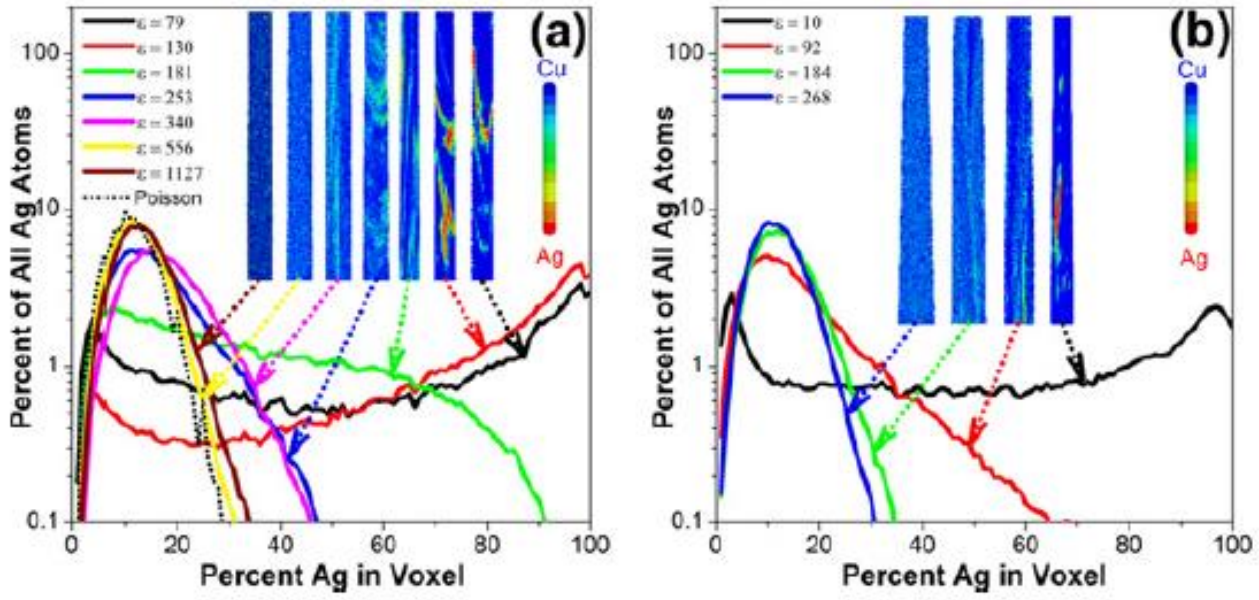

Fig. 2.1: Atom probe tomography reconstructions of Cu-10Ag alloys at increasing strains [9]. Graphs depict the normalized amount of silver relative to Cu. Initial average particle size is (a) 60nm and (b) 20nm.

In multi-phase materials, dislocation motion across the interface can be limited due to the lack of coherency at the boundary, just as in high angle grain boundaries in a polycrystalline metal [6]. Dislocations pile up at the boundary increasing the stress on the opposite grain until the stress is high enough to move dislocations in the opposite grain. This sort of strengthening is well

established in terms of the Hall-Petch relationship, in which the decreasing size of the grains increases the strength of the material. Also the microstructural stability of the material is enhanced because dissolution is only able to take place via diffusion of atoms from the particle surface rather than the dislocation-based mixing mechanism seen in the Cu-Ag system, where dislocations easily pass through the particle-matrix interface. In the FCC-BCC systems such as Cu-Nb and Cu-V, the microstructures remain relatively stable even to high strain. As seen in the MD simulation in Fig. 2.2, BCC particles like Nb or V in an FCC Cu matrix do not change much in size even to high strain because dislocations are not able to pass through the interface. Experimental evidence suggests in fact that shear strain in a Cu-matrix with Nb particles selects a steady-state particle size that depends on global concentration, see Fig. 2.3 [11]. Dislocations passing around particles can take Nb atoms with them, but they cannot split particles by the cutting mechanism; this is also confirmed by starting with a solid solution of material formed by PVD, where Nb atoms cluster and form particles, then reaching a steady-state size after a large HPT strain is applied. Nb particles grow due to Nb atoms attaching themselves to particles through motion of atoms in the matrix, but the Nb particles shrink by dislocations passing around them and not through them. This is the case for a three-dimensional particle in a matrix, where the particle-matrix interaction is dependent primarily on the positive heat of mixing and difference in atomic structure, though simulation showed there was a rotation of the BCC particles to a preferred orientation, predominantly with the Kurdjumov-Sachs orientation relationship, which will be discussed more shortly [8]. However, in two-dimesional mulitlayer materials, the interface structure or character plays a much more important role in deformation response beyond the atomic structure of the constituent phases [12-15]. The role of the interface character has thus far not been discussed, but as will be

shown throughout this dissertation, the interface character between phases in two-dimensional systems plays a pivotal role in a material's response to deformation and radiation.

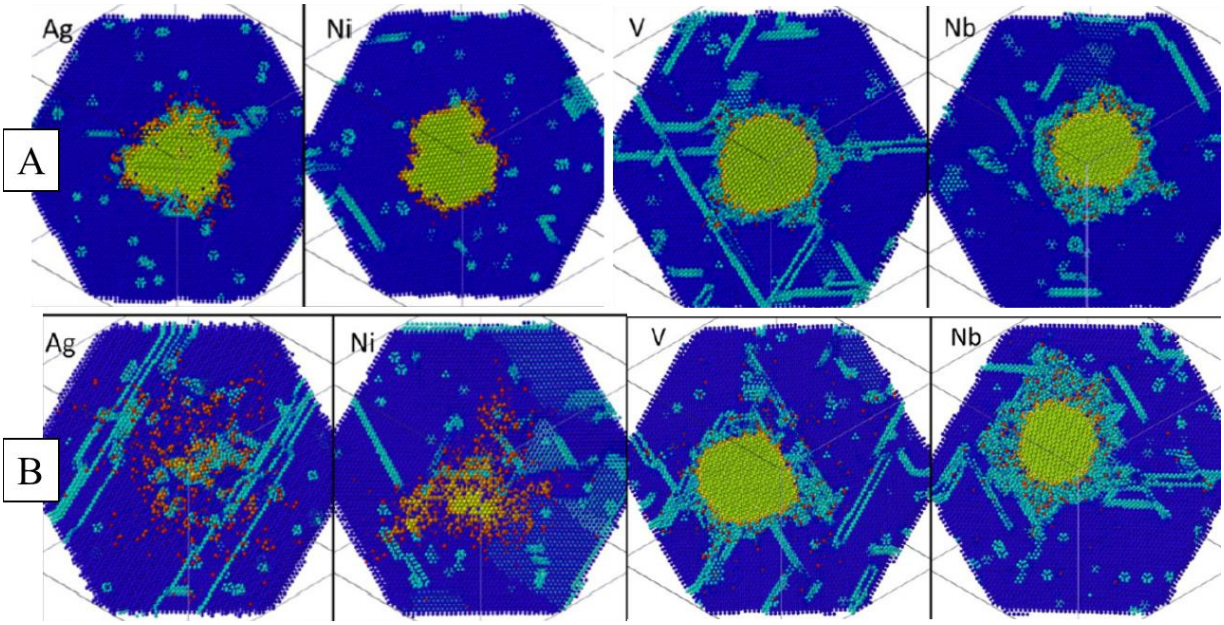

Fig. 2.2: Molecular dynamics simulation of initially spherical Ag, Ni, V, and Nb particles in a Cu matrix subjected to shear strain of (a) 6 and (b) 60 [8].

The interface character (IC) in materials, particularly in two-dimensional multilayer materials, is defined as the orientation relationship between the constituent materials as well as the habit plane, or interface plane. The interface between the Cu and Nb layers has the Kurdjumov-Sachs (KS) orientation relationship, where the crystallographic close-packed directions and closest packed planes of each metal are parallel with one another across the interface: the <-110>(111) for FCC Cu and the <1-1-1>(110) for BCC Nb [15]. The habit plane in the traditional KS interface is the closest-packed planes of each metal: {111} for Cu and {110} for Nb; see Fig. 2.4(a). This interface character, taken as the orientation relationship and habit plane, will be referred to as {111}KS. It is the dominant interface character in nano-multilayer samples fabricated by PVD via magnetron sputtering of Cu and Nb layers alternately grown on a single crystal substrate.

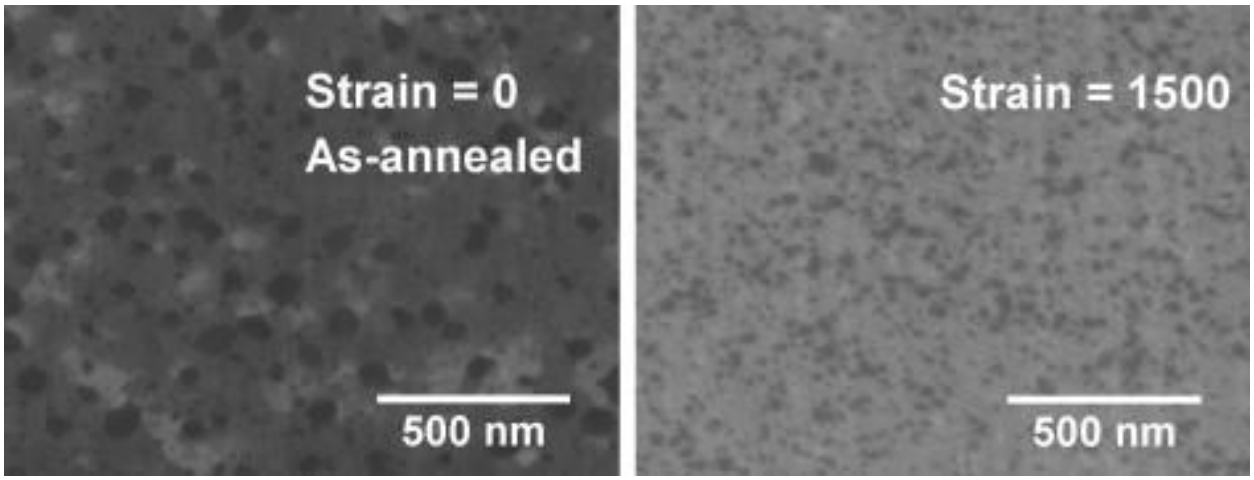

Fig. 2.3: Cu-10Nb-5Ag powder ball milled and then annealed. SEM images after HPT strain of (a) 0 and (b) 1500. Ag has dissolved but Nb particles are present at high strain [11].

Along with magnetron sputtering, various other processing techniques can be employed to control the microstructure and interface character of Cu-Nb nanocomposites, including thin film deposition techniques and severe plastic deformation techniques. I will focus on three such techniques: physical vapor deposition (PVD) by magnetron sputtering, accumulative roll bonding (ARB), and high pressure torsion (HPT). PVD and ARB produced multilayers of Cu-Nb that have atomically sharp interfaces with differing interface character; the details of which will be discussed later. HPT, along with ARB and other techniques like high energy ball milling, are a severe plastic deformation (SPD) techniques, apply large strains to materials. In HPT, extreme shear strains, with values from zero to thousands of strain, have been shown to form stable three-dimensional nanocomposites [16-18]. Its importance to this dissertation and previous studies is that it uses simple shear, which can more directly be compared to simulations [7-9, 19]. This technique was used on the Cu-Nb ARB nanolaminates previously [16], and prior to the research presented in this dissertation, had yet to be performed on the PVD-grown multi-layer composites; HPT on PVD-grown solid solution alloy samples has only recently been successfully performed [20]. The details of HPT-processing will be presented more in depth in Section 3.2 as it was used in this research to

determine and quantify the relative stability under simple shear of multilayer Cu-Nb nanocomposites with different interface character.

Another route for making Cu-Nb nanolaminates is by a bulk, severe plastic deformation (SPD) processing technique known as accumulative roll bonding (ARB). In this process, as done by researchers at Los Alamos National Laboratory, sheets of Cu and Nb measuring 1 mm in thickness are rolled together forming a metallic bond; the Cu-Nb sheet is then cut, stacked, and rolled again doubling the number of layers [21]. This process is repeated until the individual layer thickness is approximately 128 nm, after which rolling alone is performed to reduce the layers to a desired layer thickness as low as ~10 nm. As the individual layer thickness is reduced to a nominal layer thickness of ~18 nm, a unique texture is observed to stabilize; the OR is the same as the {111}KS interface seen in the films grown by PVD, but the habit plane is different: {112}Cu is parallel to the {112}Nb in the interface plane, see Fig. 2.4(b) [15]. The habit plane is thus rotated 90 degrees compared to that of the {111}KS. This interface will be referred to as {112}KS.

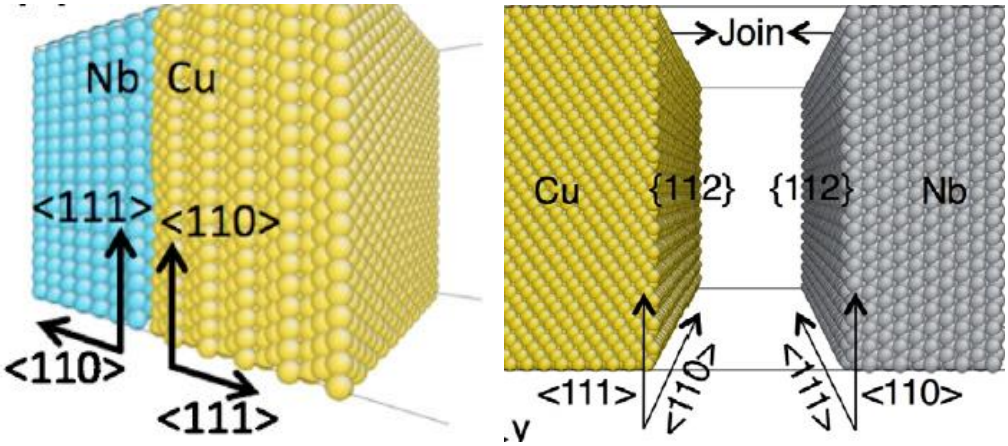

Fig. 2.4: Model of Cu-Nb (a) {111}KS and (b) {112}KS interface character [15]

Similarities and differences in the interface structure between these two ICs have a large effect on the response of the materials to various stimuli like elevated temperature, strain, and radiation [15]. The interface structure at semi-coherent interfaces, such as FCC-BCC interfaces, can be modeled as a set of misfit dislocations. These misfit dislocations are necessary to relieve

the strain energy that would accompany the formation of a fully coherent interface. The spacing between misfit dislocations or area of coherency is dependent upon the relative size of the constituent atoms and orientation relationship; in both Cu-Nb ARB and Cu-Nb PVD interfaces, the spacing is ~1-2 nm, and areas of coherency between Cu and Nb do not exceed ~2 nm^2 for both interfaces [22]. The density of misfit dislocation intersections (MDI's) is dependent on the relative difference in lattice parameters; thus Cu-Nb interfaces have a higher density of MDI's than Cu-V, and therefore, tend to have better response to deformation and radiation [15]. In cases where multiple sets of misfit dislocations are present, the dislocation lines may intersect if the Burgers vectors and line directions are different, as shown in Fig. 2.5 for the case of Cu-Nb and Cu-V interfaces with the {111}KS interface character. The black dotted lines represent the interface misfit dislocations that run lie within the habit plane between the FCC Cu and BCC Nb or V represented by the yellow and blue circles. Where the two sets of non-parallel misfit dislocations intersect, there is an amount of free volume, represented by the purple circles. This free volume plays an important role in the interface's ability to serve as a sink for defects. It has been shown, and as will be noted later, that the ability to trap He atoms and other defects depends at least in part on the density of free volume, or constitutional vacancies, at the interface [23]. Cu-Nb interfaces can trap more He atoms than Cu-Mo interfaces, which can trap more He atoms than Cu-V interfaces [24]. The proportionality of each is relative to the density of misfit dislocation intersections (MDI) as Cu-Nb has more MDI's than Cu-Mo and Cu-V, which can readily be seen in Fig. 2.5 between Cu-Nb and Cu-V. All MDI's do not necessarily have a localized free volume and is dependent on the orientation of the constituent sets of dislocations.

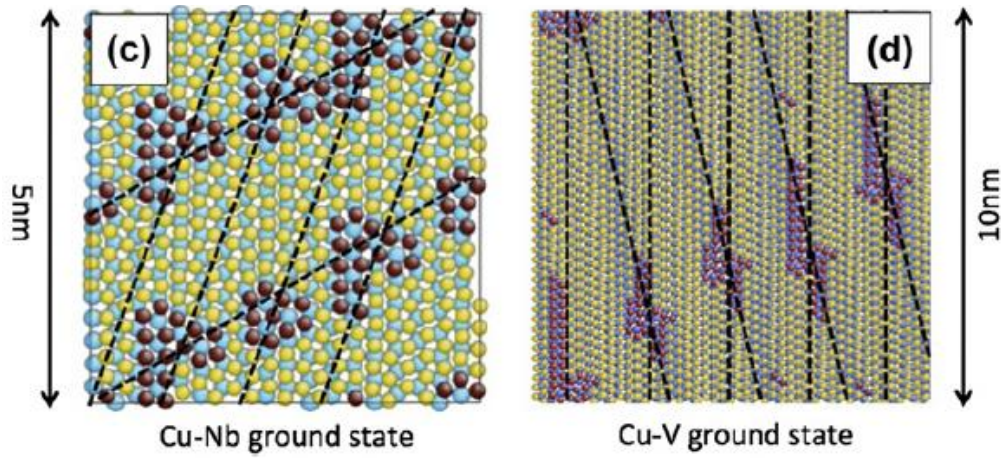

Fig. 2.5: Model of {111}KS interface character of (a) Cu-Nb and (b) Cu-V featuring constitutional vacancies (purple spheres) located at in-plane misfit dislocation intersections [15].

The orientations of the misfit dislocations of the ARB material with the {112}KS interface character and PVD material with the {111}KS interface character are different. Cu-Nb {111}KS interfaces have two sets of misfit dislocations with Burgers vectors that lie within the habit plane; and since these are not parallel, shearing of this interface can happen in any direction within the habit plane [15]. In contrast, Cu-Nb {112}KS interfaces have only one set of misfit dislocations with Burgers' vectors that lie within the habit plane; therefore, dislocation movement within the interface by glide can only occur in one direction, the direction of the Burgers vector [15]. As a result, the Cu-Nb {112}KS interface has an interface shear strength that is ~3-5 times higher than that of the Cu-Nb {111}KS interface. Weak interfaces, or interfaces with low shear strength, attract and adsorb dislocations into the interface plane more readily than high shear strength interfaces [25]. Therefore, it is expected that when high shear strain is applied that the PVD-grown Cu-Nb material with {111}KS interfaces and a low interface shear strength of ~300-550 MPa will remain more stable to higher strains than the ARB-fabricated Cu-Nb material with {112}KS interfaces and a high interface shear strength of ~1.5 GPa [26]. These differing interface structures affect the interface morphology as seen in the HRTEM micrographs in Fig. 2.6, where the

{111}KS interface grown by PVD has a flat interface while the {112}KS interface formed by ARB has a faceted interface that lies out of plane [27].

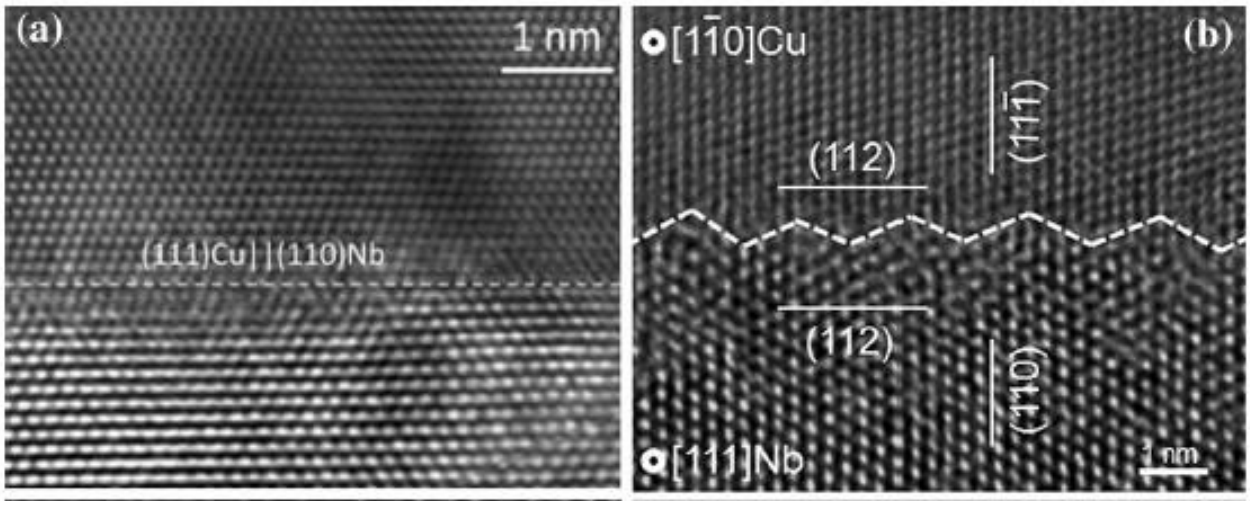

Fig. 2.6: HRTEM micrographs of predominant interfaces in Cu-Nb nanolaminates fabricated by (a) PVD with the {111}KS interface and (b) ARB with the {112}KS interface [27].

2.2 Plastic Deformation of Immiscible Metal Nanocomposites

The difference in misfit dislocation structure and interface shear strength leads to a difference in mechanical response and deformation behavior. Figs. 2.7 and 2.8 show results of in-situ micropillar compression tests of Cu-Nb PVD-grown material with individual layer thickness of 5 nm and 40 nm, and of Cu-Nb ARB material with a nominal individual layer thickness of 18 nm [27]. All three sets of pillars yield at a true stress of approximately 1.5-2.5 GPa, which is about an order of magnitude greater than the yield strength of pure Cu or Nb, which can be attributed to the Hall-Petch based strengthening of these thin multilayer materials. The yield strength, though, of the ARB material with a nominal 18nm individual layer thickness is roughly the same as a PVD-grown material with twice the individual layer thickness. However, after yielding, the PVD samples exhibit deformation via interfacial sliding while the ARB samples do not. The strain to failure is also much larger for the PVD-grown material than the ARB material, which fractured at a relatively small strain; the PVD-grown material did not exhibit any fracture up the strain that was tested.

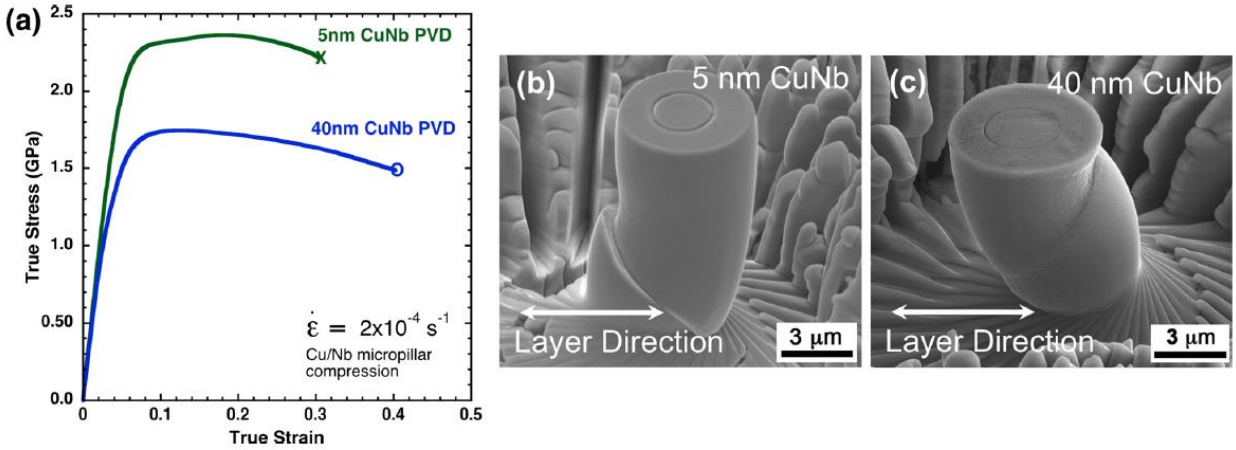

Fig. 2.7: Micropillar compression tests of 5 nm and 40 nm Cu-Nb multilayer composites formed by PVD. SEM images of final test condition for (b) 5 nm and (c) 40 nm samples where pillars have yet to fracture.

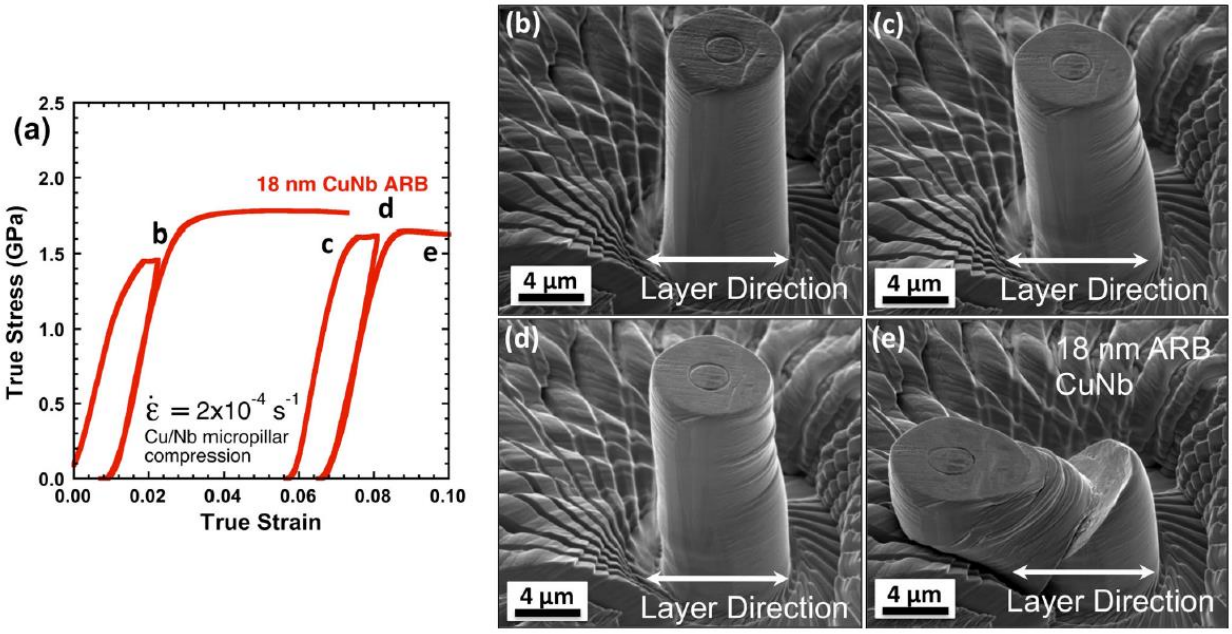

Fig. 2.8: Micropillar compression test of ARB material and SEM images after various stages of the test including final fracture [18].

These observations are supported by molecular dynamics (MD) simulation [19], as Zhou, et al, explored the effects of simple shear deformation on {111}KS, NW, and {112}KS interfaces [19]. Simple shear is directly comparable to HPT and can provide insights for other severe plastic deformation processes such as wire drawing and ECAP [28]. The simulation results provide additional insights into the structural stability of each interface type. Fig. 2.9 shows the structure of Cu-Nb bilayers with the NW and {112}KS interface before and after simple shear strain [19]. The NW interface, like the {111}KS, remains stable and deforms completely by interfacial sliding with negligible chemical mixing. In the {112}KS interface sample, plastic deformation is confined to the Cu layer, and the Nb layer deforms only elastically until an amorphous phase develops at the interface. Grain rotation also takes place resulting in the formation of a new orientation relationship [19]; as in the ARB material, the resistance to grain rotation is relatively small. As demonstrated in Fig. 2.10, Vo, et al, shows supporting evidence for the relative stability of {111}KS and lack of it in the {112}KS [7-9]. No chemical mixing occurs

in the {111}KS interface due to deformation by interfacial sliding, while chemical mixing occurs across the {112}KS interface [9].

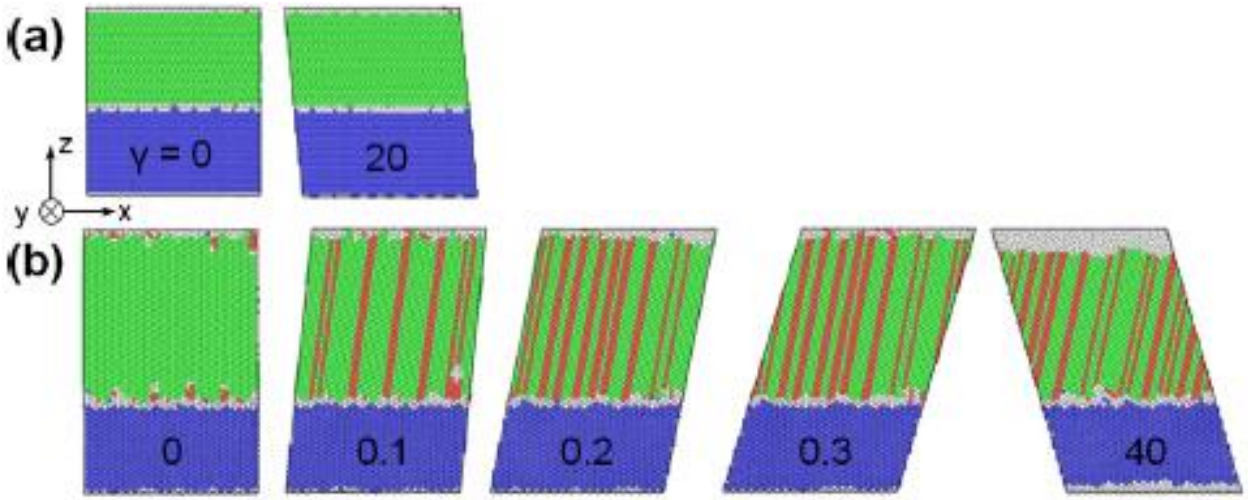

Fig. 2.9: Cu-Nb (a) NW OR and (b) {112}KS before and after simple shear along interface; Colors: green – FCC, blue – BCC, red – HCP, and gray – amorphous [19].

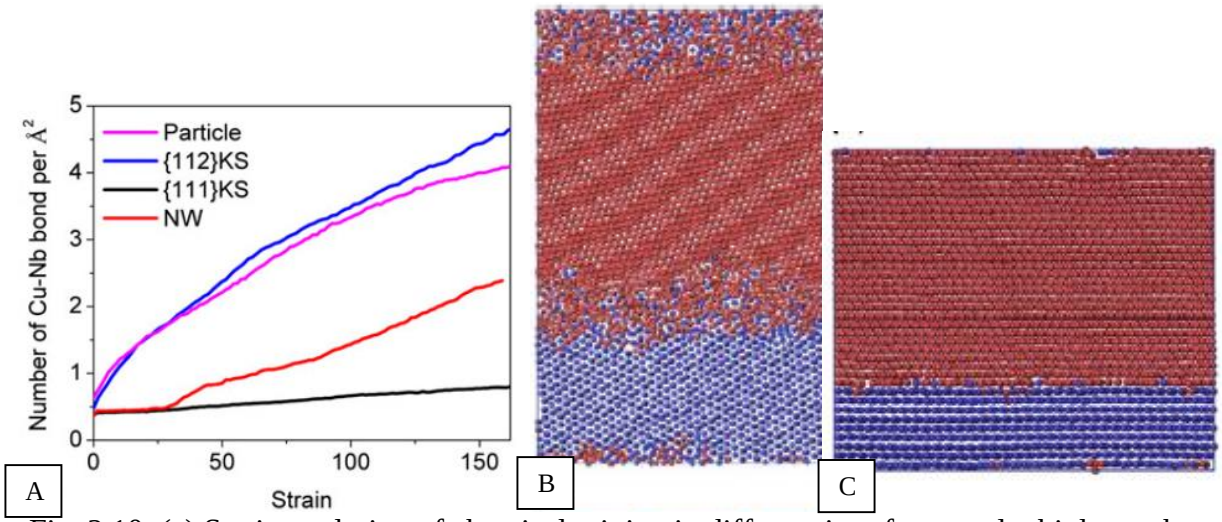

Fig. 2.10: (a) Strain evolution of chemical mixing in different interfaces under biplanar shear deformation. Atomic configuration at strain = 100 with starting configuration of (b) {112}KS and (c) {111}KS [9].

Experimental studies of HPT on Cu-Nb ARB nanolaminates support some of the conclusions put forth by the simulations, in particular, that the ARB interface becomes structurally unstable with increased strain. The microstructure of the Cu-Nb nanolaminates with an initial layer thickness of 18 nm evolved from a lamellar structure to a three-dimensional nanocomposite

consisting of interconnected Cu and Nb phases [16]. At a HPT strain of 4.2, the lamellar structure remains stable as seen in Fig. 2.11(a), but the {112}KS texture has been mostly removed. At a HPT strain of 10.8, the lamellar structure begins to destabilize at local instabilities with the formation of swirls as seen in Fig. 2.11(b); at this point the grain size is still approximately the same as the initial ARB material. These swirls and kinks are seen elsewhere in other multilayer materials subjected to shear deformation, such as in Cu-Nb and Cu-Ag nanocomposite materials subjected to wear, and even in sedimentary rock formations; these types of formations will be discussed in more detail in Chapter 4 to help describe the mechanism for the transition from two-dimensional multilayers to three-dimensional interconnected composites. From HPT strains of ~70 to ~290, the microstructure evolves from a mixed state to a fully three-dimensional microstructure with a corresponding reduction in the grain size to ~5 nm as is confirmed by X-ray diffraction with the Scherrer equation to determine crystallite size. This steady-state microstructure remains stable through HPT strains as high ~6000. This structure is shown in the atom probe tomography (APT) reconstruction in Fig. 2.11(c), where an interconnected Cu-rich phase is interspersed with an interconnected Nb-rich phase. A unique steady-state microstructure is stabilized regardless of the initial layer thickness. HPT strains greater than 10,000 result in the same three-dimensional steady-state for Cu-Nb ARB composites with initial layer thickness of 200 nm and 2 μm. Similar steady-state microstructures for the 50/50vol% Cu-Nb composition were also found in nanocomposites during high energy ball milling and HPT of Cu and Nb powders [11]. Not all of the aspects in the previous simulations on the {112}KS were in agreement with the experiments, where in particular as no amorphization at interfaces was found and plastic deformation was found to take place in both the Cu and Nb phases [16].

HPT of the {111}KS or NW interface has yet to be performed. It is this important missing information that will be investigated in this work and discussed in full later. It is expected based on the previously discussed simulation and experimental research that the Cu-Nb PVD interfaces will be more stable under high shear strain compared to the ARB interfaces. The microstructure is expected to retain a lamellar structure to higher strains than the ARB material, and only if local instabilities arise will the layered morphology change.

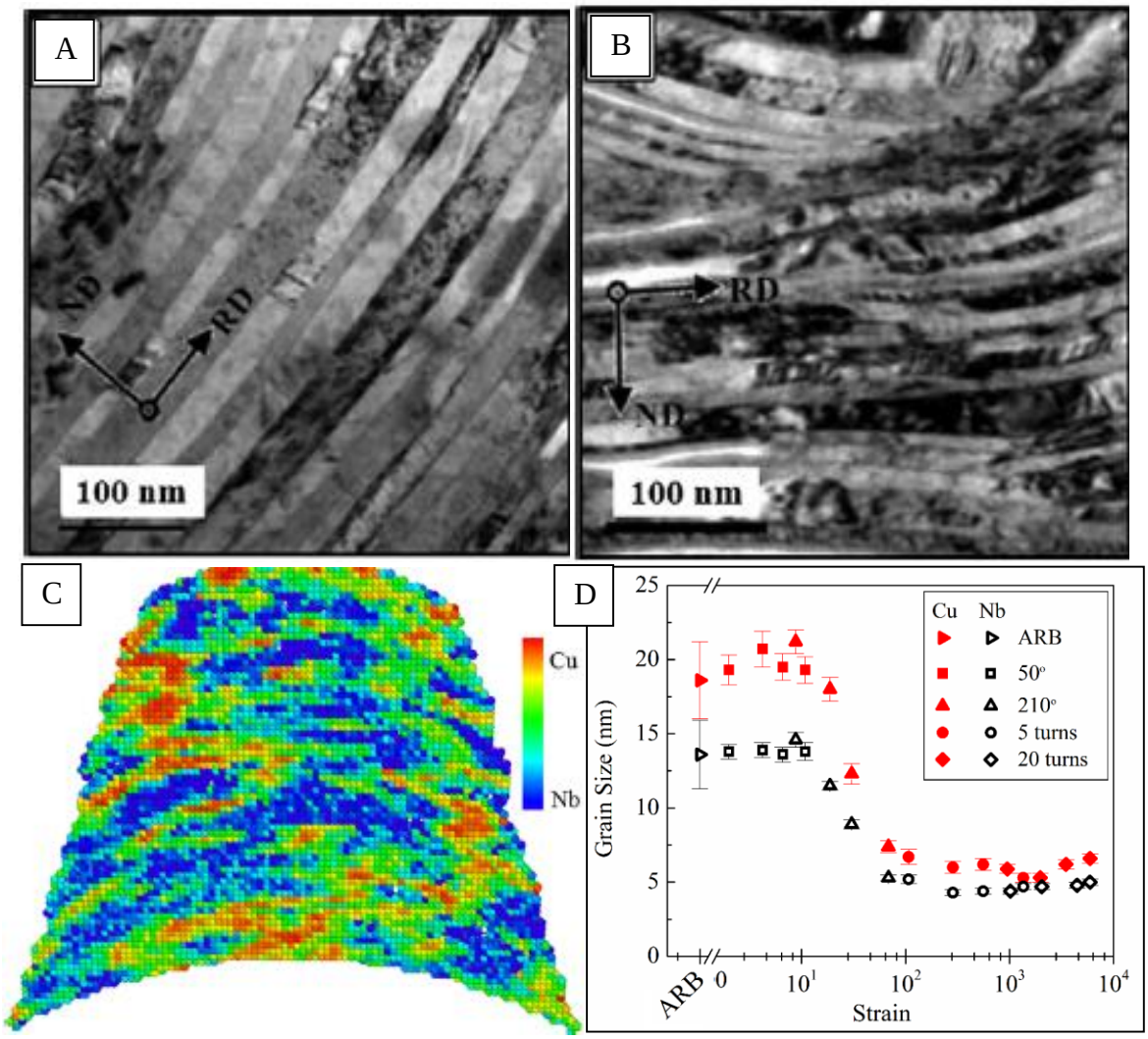

Fig. 2.11: Bright field TEM of Cu-Nb ARB subjected to HPT strain of (a) 4.2 and (b) 10.8. (c) APT reconstruction map of sample at HPT strain of 1990, and (d) grain size as a function of strain as determined by X-ray diffraction using the Scherrer equation [11].

2.3 He Irradiation of Metals and Immiscible Metal Nanocomposites

Implanted helium is known to have deleterious effects on the microstructure and mechanical properties of structural materials, as He is insoluble in most materials, coalesces into gas-filled bubbles, and helps to nucleate voids [29]. Among the detrimental effects are changes of the strength and ductility found in steels implanted with He, see Fig. 2.12. In these steels, implanted He increases the hardness and reduces the ductility because dislocation motion is greatly reduced and can lead to failure at low strain. Extensive research has focused on mitigating the detrimental effects of He, particularly in reactor materials where He is produced in n-α reactions [30-33].

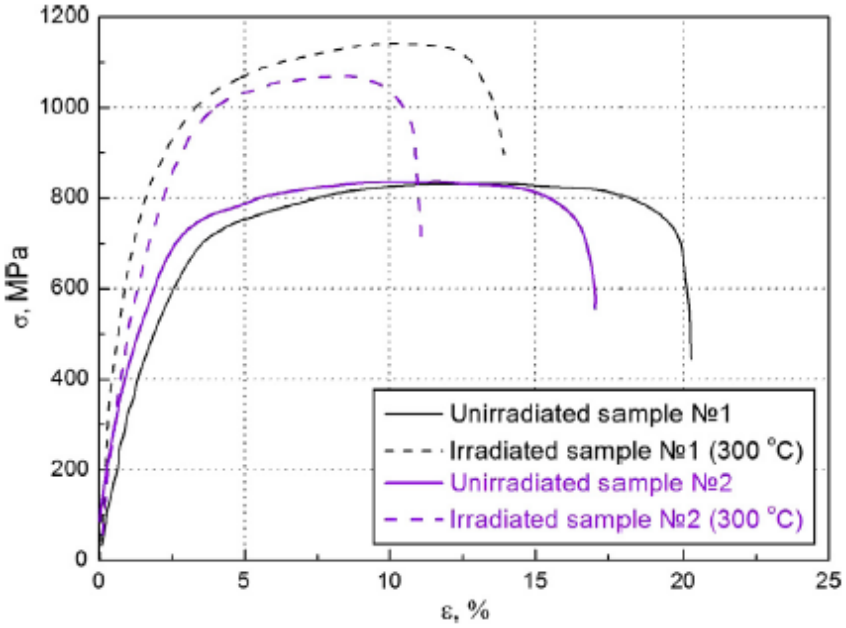

Fig. 2.12: Tensile stress-strain curves of ODS EUROFER steels at 300 ˚C for He-implanted and as-received samples [30]

Helium implantation is apparent in large quantities such as in first wall materials in fusion reactors with the concentration reaching ~10 appm He/dpa, but He concentration, at ~0.1 appm He/dpa, does not reach these relatively high levels in fission reactor designs even after many years [34]. For this reason, He implantation experiments have a two-fold purpose: determining the effects of large concentrations of He on a material and how to mitigate those

effects, as well as being used as an indirect method to quantitatively compare the sink strength and overall radiation damage tolerance of different materials. Implanted He produces damage mainly through the creation of vacancy and interstitial pairs, or Frenkel pairs, as well as being an immiscible solute, which diffuses quickly to form bubbles and voids, such as those formed in implanted tungsten, see Fig. 2.13 [35].

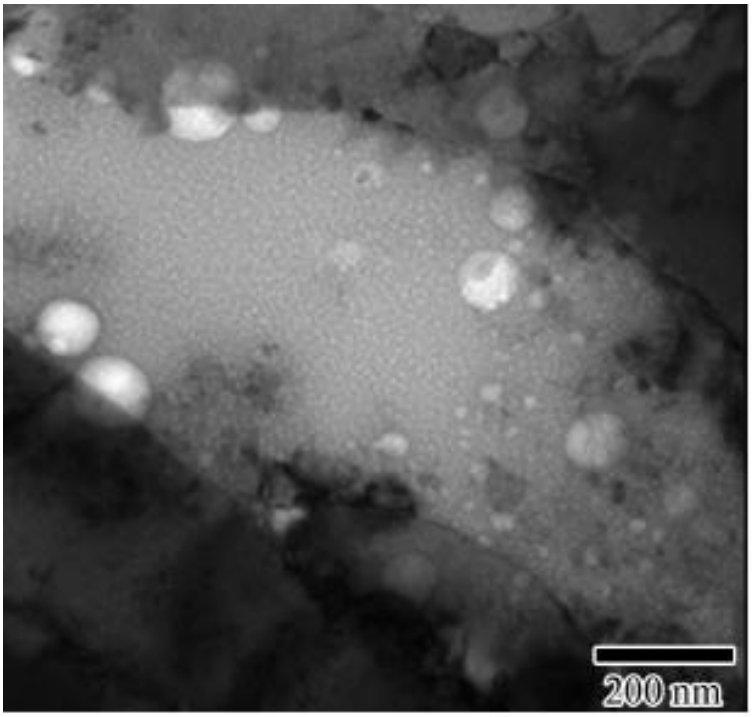

Fig. 2.13: Under-focus Bright-field TEM micrograph of He-implanted and subsequently annealed tungsten; both large voids and small bubbles are present [35].

While He-ions do create collision cascades, they are not the size that is apparent in neutron or heavy ion implantation. This difference is seen in the recoil spectrum of different particles in copper shown in Fig. 2.14, as the He spectrum lies between neon and protons; heavy ions like krypton more accurately simulate the displacement damage of neutrons that implant in fission reactor materials [36]. However, it can be difficult to quantitatively compare the effects of heavy ions and neutrons on different materials, particularly among materials that are bulk processed like those processed by severe plastic deformation in this dissertation. Based on experimental research

on Cu-Nb and Cu-V multilayer nanocomposites grown by PVD that will be described in more detail later in this section, the radiation damage tolerance of materials subjected to He implantation follows the same trend as being subjected to heavy ion irradiation in that materials that are more tolerant to heavy ion irradiation are also more tolerant to He-ion irradiation [37]. Therefore, it is reasonable to use He implantation to elucidate the relative response of different materials under heavy ion and neutron irradiation.

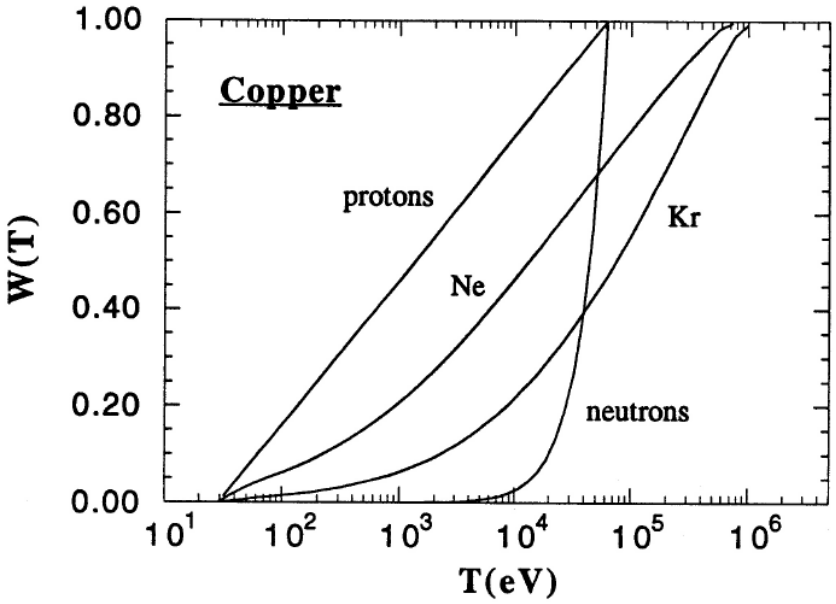

Fig. 2.14: Weighted average recoil spectrum of atomic and subatomic particles in copper [36].

Whether defects are created by heavy ions, neutrons, or He atoms, sinks such as surfaces, dislocations, grain boundaries, or other interfaces, are necessary to annihilate the defects and reduce the concentration of defects. Nanostructured metals should be advantageous for this purpose, as their high densities of grain boundaries and interphase boundaries can trap large amounts of He and point defects and thus suppress bubble nucleation [38-41]. Ultrafine-grained single phase materials have been shown to trap helium at grain boundaries. W. Han, et al, considered the case of nanocrystalline implanted with He at 450 ˚C, and as depicted in Fig. 2.15(a), they found that He-filled bubbles formed at grain boundaries and inside larger grains [42]. This

demonstrates that helium diffuses to sinks like grain boundaries, but only if the diffusion length sufficiently larger than the grain size. However, grain boundaries within pure metals and single phase alloys can coarsen at high temperatures or during irradiation due to the increased interfacial free energy added to the system resulting in a reduction in the density of defect sinks [42-45]. Therefore, materials that are microstructurally stable and resist coarsening for extended periods at high temperature and during irradiation are necessary; multiphase materials containing highly immiscible refractory elements or phases are an option to achieve damage tolerance with microstructural stability.

In particular, interphase boundaries in oxide dispersion strengthened (ODS) steels have been shown to be good defect sinks and to be stable in the extreme environment of a nuclear reactor making them strong candidate materials for next generation fission and fusion power plants [46-48]. In the ODS steel implanted with He shown in Fig. 2.15(b), a large number of bubbles that are relatively large in size have formed within the matrix; however, within the vicinity of the oxide particle, the bubbles are reduced in size and number density demonstrating that the oxide-matrix interface is a good sink for defects. The interface character at the oxide-matrix interface depends on multiple factors including the composition and size of the particles; also, these factors can vary among oxide particles due to the mechanical alloying processing that is used to produce the material [47, 48]. Owing to this complexity and heterogeneity of ODS alloys, they are not well suited for elucidating the relationship between interface structure and trapping point defects and He atoms.

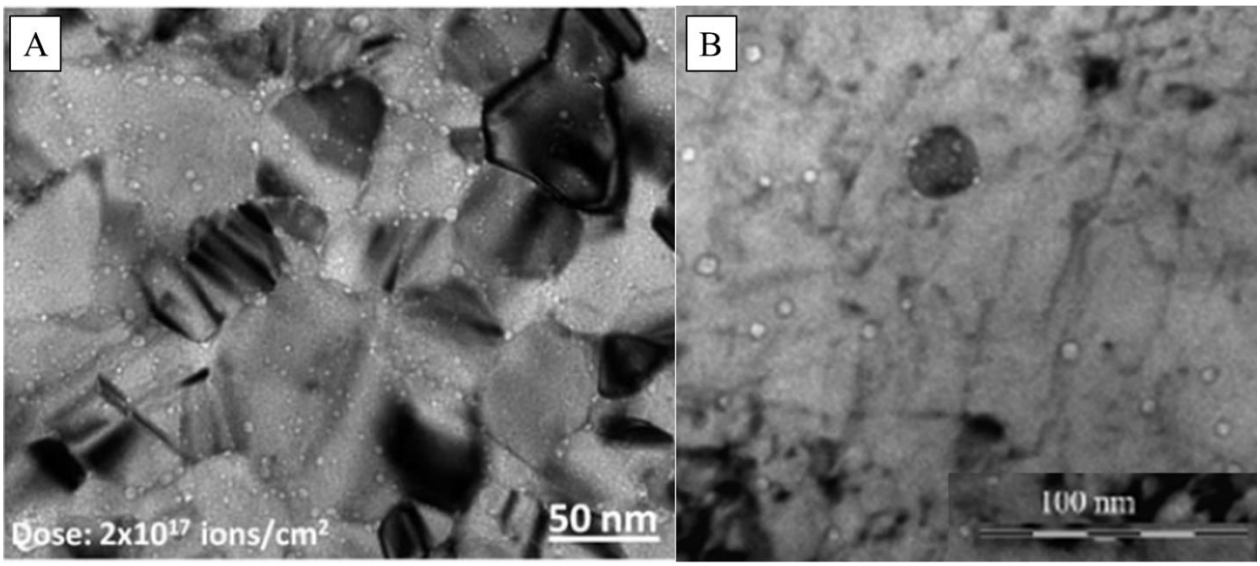

Fig. 2.15: Under-focus bright field TEM micrographs of (a) nanocrystalline Cu implanted with He at 450 ˚C with bubbles in bulk and at grain boundaries [42] and (b) EUROFER ODS steel implanted with He at 500 ˚C with bubbles in the bulk and at surface of oxide particle [30]

Interphase boundaries between immiscible metals with semi-coherent interfaces, such as in Cu-Nb [23, 49], Cu-V [50, 51], Cu-Fe [52], and Ag-V [53], are more appropriate for this latter purpose as they are good defect sinks, are stable under irradiation, and their interface structures can be controllably varied, characterized, and modelled [15, 38, 54, 55]. Previous research on Cu-Nb and Cu-V produced by PVD has indeed shown that the {111}KS interface character effectively suppresses He-filled bubble formation. This finding has been attributed to the large density of in-plane misfit dislocation intersections (MDI's) in this interface [15, 24]. In the {111}KS interface, atomistic simulations show that there is excess free volume in the form of constitutional vacancies, as seen in Fig. 2.5, with a concentration as high as 5 at% vacancies; whereas the {112}KS interface has zero constitutional vacancies due to its misfit dislocation structure [15]. As demonstrated in Fig. 2.16, there is a reduction in the formation energy of vacancies at the interface relative the bulk FCC Cu and BCC Nb and is spatially associated with the MDI's; thus defects are strongly attracted to the interface from both the Cu side and Nb side. There is not such a large drop in the vacancy formation energy in the {112}KS interface. Experimental research previously has looked to

confirm the importance of the drop in vacancy formation energy and free volume at MDI's in the {111}KS interface in trapping defects and He atoms.

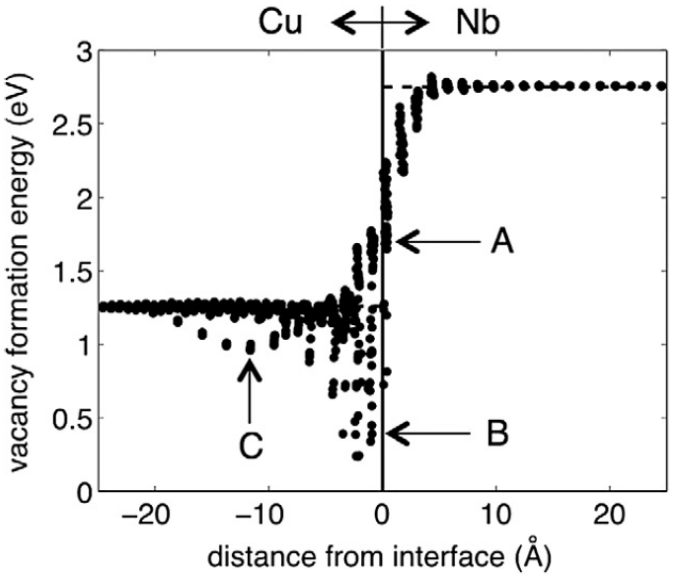

Fig. 2.16: Vacancy formation energy as a function of distance from the Cu-Nb {111}KS interface featuring an energy well on the Cu side of the interface [15]

Experimental research has quantified the effectiveness of immiscible metal nanocomposites with the {111}KS interface character at trapping defects when subjected to both heavy ion irradiation and He-ion irradiation, both of which show similar trends. Mao et.al determined the relative sink efficiency of interfaces in three metal nanocomposites (Cu-Nb, Cu-V, and Cu-Ni) subjected to Kr-ion irradiation by measuring the tracer-impurity radiation enhanced diffusion [37]. Cu-Nb and Cu-V both have the {111}KS interface character, and Cu-Ni has a fully coherent FCC {111} interface character. The sink efficiency was measured using Au-impurity diffusion in Cu, as seen in the schematic in Fig. 2.17(a) where the Cu_9Au layers, approximately 5 nm thick, were centered in 30 nm, 60 nm, and 120 nm thick Cu layers. The samples were irradiated at high temperature with Kr-ions that create cascade events resulting in a super-saturation of point defects, and then the distribution of Au was measured using Z-contrast STEM. If the density of vacancies available is large, the spread of the Au-containing layer will be large;

but if vacancies become trapped at sinks, the density of vacancies available for diffusion will be small and the spread of Au-containing layer will also be small. Comparing these profiles with rate-theory equations allows for the calculation of sink efficiency. In Fig. 2.17(b), vacancy concentration of each material as a function of layer thickness, and thus sink efficiency, is plotted. The Cu-Ni interface that is fully coherent has an extremely small efficiency for trapping any defects at the interface, while the {111}KS interfaces in Cu-Nb and Cu-V are very efficient, with the relative efficiency between the two proportional to the density of MDI's. This experiment is a great way of measuring sink efficiency of multilayers grown via PVD; however, this type of tracer diffusion experiment is difficult to use for 2D and 3D materials formed by bulk processing techniques such as ARB, HPT, and high energy ball milling.

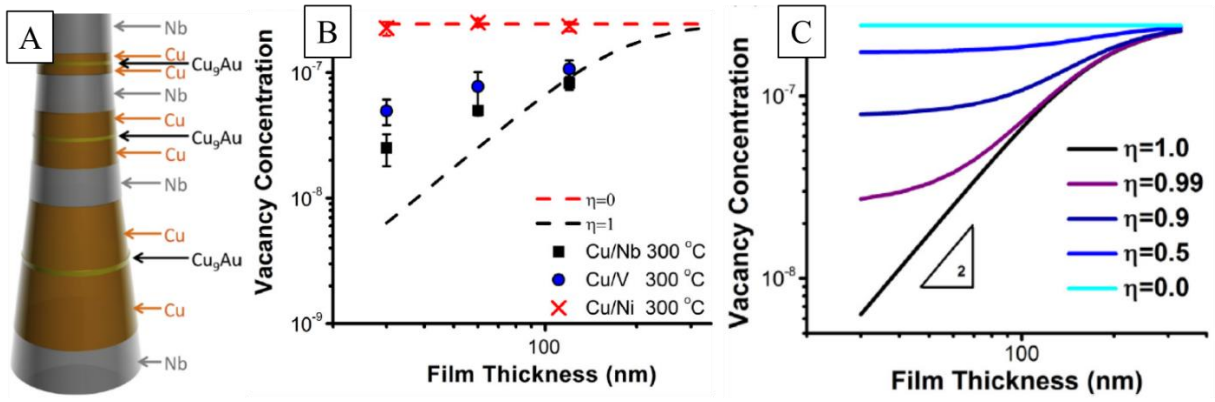

Fig. 2.17: (a) Schematic of Cu-Nb multilayer composite subjected to Kr-ion irradiation; Cu layers are 30, 60, and 120 nm thick and Cu_9Au layers centered in the Cu layers are 5 nm thick. (b) Vacancy concentration of Cu-Nb, Cu-V, and Cu-Ni films as a function of layer thickness of films subjected to Kr-ion irradiation at 300 ˚C. (c) Calculated vacancy concentration as a function of film thickness for interfaces with different sink efficiency [37].

A different experimental method must thus be used to measure the sink efficiency and the ability of these materials to tolerate radiation. As such, He-ion implantation can be used to measure the efficacy of non-deposition grown materials, as well as of PVD-grown materials. Demkowicz, et al, measured the concentration of He that can be stored at Cu-Nb and Cu-V interfaces before bubbles are visible in TEM [24]. Multilayer samples with the {111}KS interface character were

implanted with He; the depth and range at which bubbles are visible in under and over-focus TEM was measured and compared with the concentration of He measured by nuclear reaction analysis (NRA) or by comparison with the He-concentration profile determined by SRIM simulation. An example of this in Fig. 2.18 of Cu-Nb nanocomposites with the {111}KS interface with 5.6 nm individual layer thickness shows that bubbles form primarily at interfaces as He diffuses to these interfaces and becomes trapped. In this research, multiple individual layer thicknesses were tested, and it was shown that the trapping ability of the material scaled with interface area density. Cu-Nb interfaces trap ~8.5 He-atoms/ nm^2 before bubbles form and Cu-V interfaces trap ~1.9 He-atoms/ nm^2 before bubbles form; roughly a factor of 4 difference, which is also roughly the difference in MDI density between Cu-Nb and Cu-V.

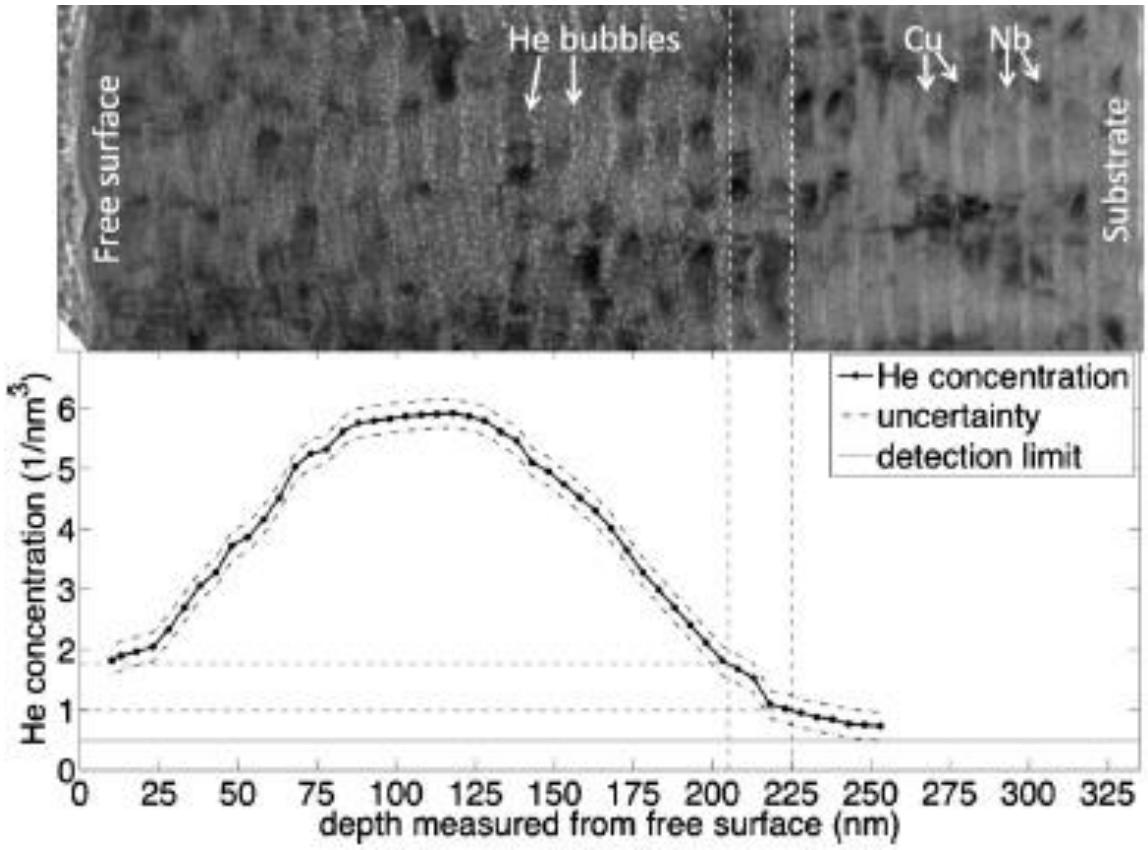

Fig. 2.18: (a) Under-focus BF TEM micrograph of Cu-Nb multilayers grown by PVD with 5.6 nm individual layer thickness subjected to He-implantation and (b) corresponding He concentration profile measured by nuclear reaction analysis. He bubbles are not found below a concentration of ~1.4 He atoms/ nm^3 at a depth of 215 nm [24].

These research examples examined specimens grown by physical vapor deposition (PVD) and thus just one specific interphase boundary structure. Some research has also considered microstructural effects of implanted He on Cu-Nb multilayer composites formed by ARB with the {112}KS interface character [56]. As is depicted in Fig. 2.19, the location, density, and size of He-filled bubbles is very similar that seen in PVD-grown Cu-Nb multilayers [56]. The bubbles are ~1-2 nm in diameter and form primarily at the interfaces and on the Cu side of the interfaces, just as is seen in {111}KS material, and therefore it is concluded that both {111}KS and {112}KS interfaces behave qualitatively in a similar fashion under He implantation. These materials have also been observed under implantation at high temperature, see Fig. 2.20 [56, 57]. Bubbles coalesce and grow primarily within the Cu layers, and the growth is limited to the layer thickness because the interface serves as a hard barrier and He energetically prefers to stay on the Cu side of the boundary.

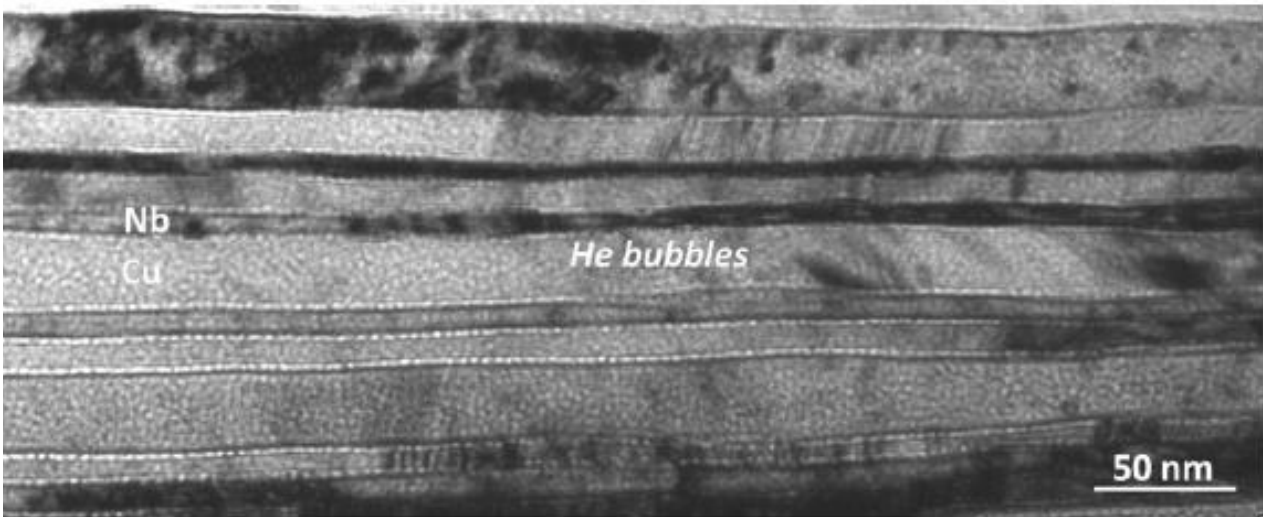

Fig 2.19: Under-focus BF TEM micrograph of Cu-Nb ARB material implanted with He. Bubbles are seen at the interface and within thicker Cu layers [56].

Though expected to not be as efficient as the {111}KS interface character due to the lack of constitutional vacancies at the interface, the efficacy of the {112}KS interface character has not

been quantified and compared experimentally in this prior research. Thus, the work presented in this dissertation examines the efficiency of interphase boundaries for trapping He more broadly: still focusing on nanocomposites of Cu-Nb, while also comparing trapping efficiencies of two-dimensional materials formed by PVD and ARB and of three-dimensional materials formed by other various severe plastic deformation (SPD) techniques such as HPT and high energy ball milling, as these procedures are highly conducive to bulk processing of materials [28].

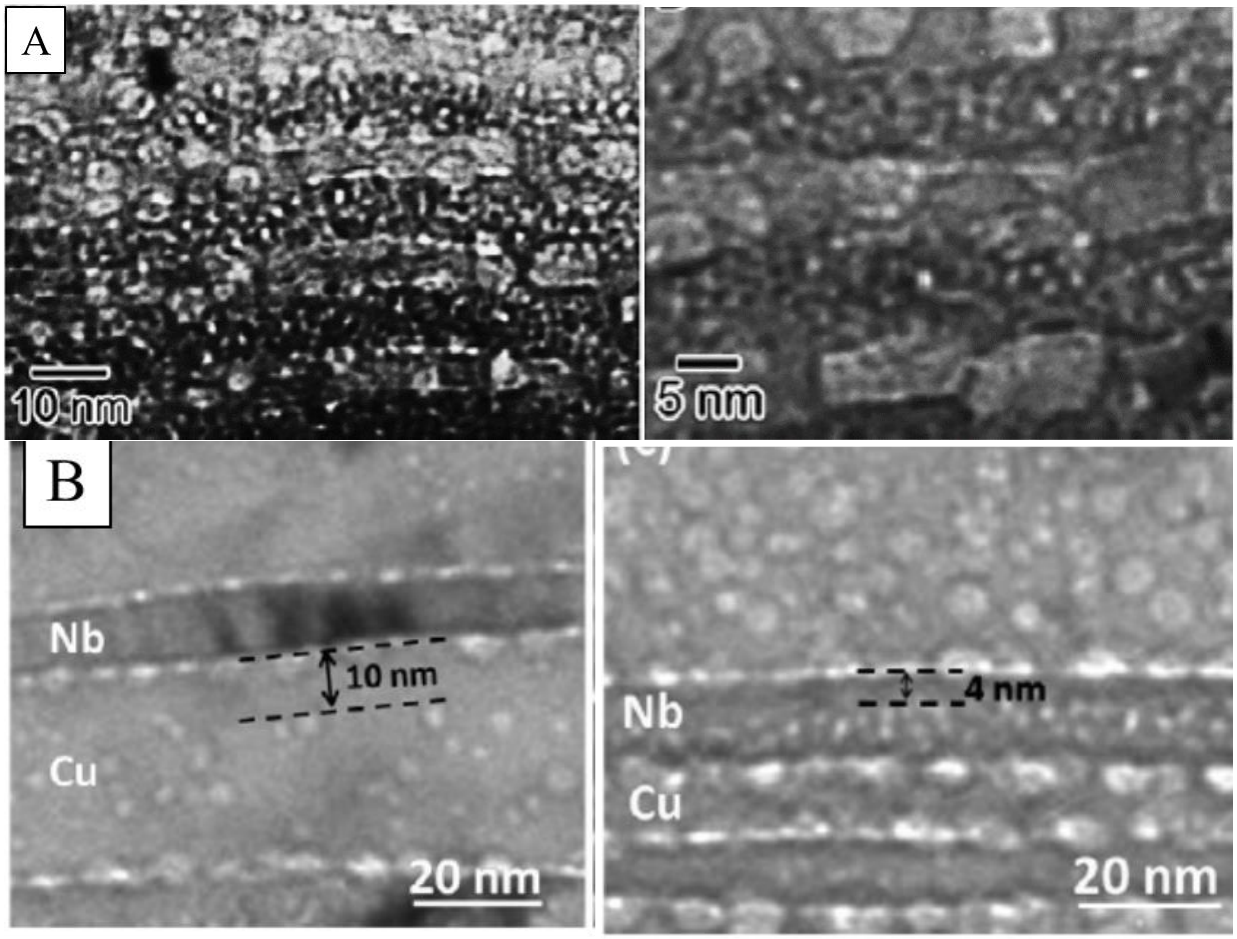

Fig. 2.20: Under-focus BF TEM micrograph of (a) Cu-Nb PVD material [57] and (b) Cu-Nb ARB material [56] implanted with He at high temperature. Bubbles grow largest in Cu layers and are limited in size by the thickness of the layers.

2.4 References

[1] E.G. Fu, N. Li, A. Misra, R.G. Hoagland, H. Wang, and X. Zhang. *Materials Science and Engineering A* **493** (2008) 283.

[2] A. Taisne, B. Decamps, and L. Priester. *Composite Interfaces* **13** (2006) 89.

[3] K. Edalati, J.M. Cubero-Sesin, A. Alhamidi, I.F. Mohamed, and Z. Horita. *Materials Science and Engineering A* **613** (2014) 103.

[4] Y.C. Wang, A. Misra, and R.G. Hoagland. *Scripta Materialia* **54** (2006) 1593.

[5] G. Saada. *Materials Science and Engineering A* **400-401**(2005) 146.

[6] N. Hansen. *Advanced Engineering Materials* **7** (2005) 815.

[7] N.Q. Vo, J. Zhou, Y. Ashkenazy, D. Schwen, R.S. Averback, and P. Bellon. *Journal of Materials* **65** (2013) 382.

[8] Y. Ashkenazy, N.Q. Vo, D. Schwen, R.S. Averback, and P. Bellon. *Acta Materialia* **60** (2012) 984.

[9] N.Q. Vo, R.S. Averback, Y. Ashkenazy, P. Bellon, and J. Wang. *Journal of Materials Research* **27** (2012) 1621.

[10] S.N. Arshad, T.G. Lach, M. Pouryazdan, H. Hahn, P. Bellon, S.J. Dillon, and R.S. Averback. *Scripta Materialia* **68** (2013) 215.

[11] M. Wang, R.S. Averback, P. Bellon, and S. Dillon. *Acta Materialia* **62** (2014) 276.

[12] A. Misra, J.P. Hirth, and R.G. Hoagland. *Acta Materialia* **53** (2005) 4817.

[13] I.J. Beyerlein, J.R. Mayeur, S. Zheng, N.A. Mara, J. Wang, and A. Misra. *Proceedings of the National Academy of Sciences* **111** (2014) 4386.

[14] R.G. Hoagland, J.P. Hirth, and A. Misra. *Philosophical Magazine* **86** (2006) 3537.

[15] M.J. Demkowicz and L. Thilly. *Acta Materialia* **59** (2011) 7744.

[16] E.H. Ekiz, T.G. Lach, R.S. Averback, N.A. Mara, I.J. Beyerlein, M. Pouryazdan, H. Hahn, and P. Bellon. *Acta Materialia* **72** (2014) 178.

[17] Y.B. Wang, J.C. Ho, Y. Cao, X.Z. Liao, H.Q. Li, Y.H. Zhao, E.J. Lavernia, S.P. Ringer, and Y.T. Zhu. *Applied Physics Letters* **94** (2009) 091911.

[18] M. Wang, N.Q. Vo, M. Campion, T.D. Nguyen, D. Setman, S. Dillon, P. Bellon, and R.S. Averback. *Acta Materialia* **66** (2014) 1.

[19] J. Zhou, R.S. Averback, and P. Bellon. *Acta Materialia* **73** (2014) 116.

[20] M. Wang. Doctoral Dissertation: *Severe Plastic Deformation in Highly Immiscible Cu Alloys* University of Illinois at Urbana-Champaign. (2014)

[21] J.S. Carpenter, S.C. Vogel, J.E. LeDonne, D.L. Hammon, I.J. Beyerlein, and N.A. Mara. *Acta Materialia* **60** (2012) 1576.

[22] N.A. Mara and I.J. Beyerlein. *Journal of Materials Science* **49** (2014) 6497.

[23] M.J. Demkowicz, A. Misra, and A. Caro. *Current Opinion in Solid State and Materials Science* **16** (2012) 101.

[24] M.J. Demkowicz, D. Bhattacharyya, I. Usov, Y.Q. Wang, M. Nastasi, and A. Misra. *Applied Physics Letters* **97** (2010) 161903.

[25] J. Wang, A. Misra, R.G. Hoagland, and J.P. Hirth. *Acta Materialia* **60** (2012) 1503.

[26] N. Li, N.A. Mara, J. Wang, P. Dickerson, J.Y. Huang, and A. Misra. *Scripta Materialia* **67** (2012) 479.

[27] N.A. Mara, I.J. Beyerlein. *Journal of Materials Science* **49** (2014) 6497.

[28] D. Raabe, P.P. Choi, Y. Li, A. Kostka, X. Sauvage, F. Lecouturier, K. Hono, R. Kirchheim, R. Pippan, and D. Embury. *MRS Bulletin* **35** (2010) 982.

[29] J. Laakmann, P. Jung, and W. Uelhoff. *Acta Metallurgica* **35** (1987) 2063.

[30] A.I. Ryazanov, O.K. Chugunov, S.M. Ivanov, S.T. Latushkin, R. Lindau, A. Moslang, A.A. Nikitina, K.E. Prikhodko, E.V. Semenov, V.N. Unezhev, and P.V. Vladimirov. *Journal of Nuclear Materials* **442** (2013) S153.

[31] S.I. Golubov, R.E. Stoller, S.J. Zinkle, and A.M. Ovcharenko. *Journal of Nuclear Materials* **361** (2007) 149.

[32] N. Li, E.G. Fu, H. Wang, J.J. Carter, L. Shao, S.A. Maloy, A. Misra, and X. Zhang. *Journal of Nuclear Materials* **389** (2009) 233.

[33] S. Frechard, M. Walls, M. Kociak, J.P. Chevalier, J. Henry, and D. Gorse. *Journal of Nuclear Materials* **393** (2009) 102.

[34] S.A Fabritsiev, A.S. Pokrovsky, S.J. Zinkle, and D.J. Edwards. *Effects of Radiation on Materials: 19th International Symposium, ASTM STP* **1366** (2000) 1226.

[35] K. Hattar, O. El-Atwani, M. Efe, T.J. Novakowski, A. Suslova, and J.P. Allain. *Materials Research Society Symp. Proc.* **1645** (2014).

[36] G.S. Was. Fundamentals of Radiation Materials Science: Metals and Alloys (2007) 130-131.

[37] S. Mao, S. Shu, J. Zhou, R.S. Averback, and S.J. Dillon. *Acta Materialia* **82** (2015) 328.

[38] M. Zhernenkov, S. Gill, V. Stanic, E. DiMasi, K. Kisslinger, J.K. Baldwin, A. Misra, M.J. Demkowicz, and L. Ecker. *Applied Physics Letters* **104** (2014) 241906.

[39] N. Li, M. Nastasi, A. Misra. *International Journal of Plasticity* **32-33** (2012) 1.

[40] X. Zhang, E.G. Fu, A. Misra, and M.J. Demkowicz. *Journal of Materials* **62** (2010) 75.

[41] I.J. Beyerlein, A. Caro, M.J. Demkowicz, N.A. Mara, A. Misra, and B.P. Uberuaga. *Materials Today* **16** (2013) 443.

[42] W. Han, E.G. Fu, M.J. Demkowicz, Y. Wang, and A. Misra. *Journal of Materials Research* **28** (2013) 2763.

[43] K.Y. Yu, Y. Liu, C. Sun, H. Wang, L. Shao, E.G. Fu, and X. Zhang. *Journal of Nuclear Materials* **425** (2012) 140.

[44] C. Sun, K.Y. Yu, J.H. Lee, Y. Liu, H. Wang, L. Shao, S.A. Maloy, K.T. Hartwig, and X. Zhang. *Journal of Nuclear Materials* **420** (2012) 235.

[45] O. El-Atwani, K. Hattar, J.A. Hinks, G. Greaves, S.S. Harilal, and A. Hassanein. *Journal of Nuclear Materials* **458** (2015) 216.

[46] C. Lu, Z. Lu, R. Xie, C. Liu, and L. Wang. *Journal of Nuclear Materials* **455** (2014) 366.

[47] J. Chen, P. Jung, J. Henry, Y. de Carlan, T. Sauvage, F. Duval, M.F. Barthe, and W. Hoffelner. *Journal of Nuclear Materials* **437** (2013) 432.

[48] J. Chen, P. Jung, and W. Hoffelner. *Journal of Nuclear Materials* **441** (2013) 688.

[49] T. Hochbauer, A. Misra, K. Hattar, and R.G. Hoagland. *Journal of Applied Physics* **98** (2005) 123516.

[50] E.G. Fu, H. Wang, J. Carter, L. Shao, Y.Q. Wang, and X. Zhang. *Philosophical Magazine* **93** (2013) 883.

[51] E.G. Fu, A. Misra, H. Wang, L. Shao, and X. Shang. *Journal of Nuclear Materials* **407** (2010) 178.

[52] P. Landau, Q. Guo, K. Hattar, and J.R. Greer. *Advanced Functional Materials* **23** (2013) 1281.

[53] Q.M. Wei, N. Li, N. Mara, M. Nastasi, and A. Misra. *Acta Materialia* **59** (2011) 6331.

[54] A. Kashinath, A. Misra, and M.J. Demkowicz. *Physical Review Letters* **110** (2013) 086101.

[55] A.Y. Dunn, M.G. McPhie, L. Capolungo, E. Martinez, and M. Cherkaoui. *Journal of Nuclear Materials* **435** (2013) 141.

[56] W.Z. Han, N.A. Mara, Y.Q. Wang, A. Misra, and M.J. Demkowicz. *Journal of Nuclear Materials* **452** (2014) 57.

[57] K. Hattar, M.J. Demkowicz, A. Misra, I.M. Robertson, and R.G. Hoagland. *Scripta Materialia* **58** (2008) 541.

CHAPTER 3

METHODS AND EXPERIMENTAL PROCEDURES

3.1 Fabrication of 2D Cu-Nb Multilayer Nanocomposites by Accumulative Roll Bonding and Physical Vapor Deposition

Two-dimensional Cu-Nb multilayered nanocomposites were fabricated for both studies covered in this dissertation. These were fabricated by two different processes: accumulative roll bonding (ARB) and physical vapor deposition (PVD) by magnetron sputtering. Nano-layered ARB Cu-Nb bulk composites were prepared by a combination of rolling and annealing steps starting from Cu and Nb 1-2 mm thick sheets and finishing with individual layer thicknesses of as small as 9 nm, as seen in Fig. 3.1, following the method detailed in ref. [1, 2]. The samples were composed of 50/50 volume fraction Cu/Nb, using starting materials of 99.99% (Cu) and 99.97% (Nb) purity, corresponding to a 60/40 ratio based on molar fractions. The material selected for the He implantation work was processed to a rolling strain of 10.93, resulting in a nominal layer thickness of 18 nm for each of the Cu and Nb layers, although the average individual layer thickness measured in this work is ≈ 25 nm. The average specific Cu/Nb interfacial area, or Cu/Nb interfacial area per unit volume, is thus 0.04 nm^{-1}.

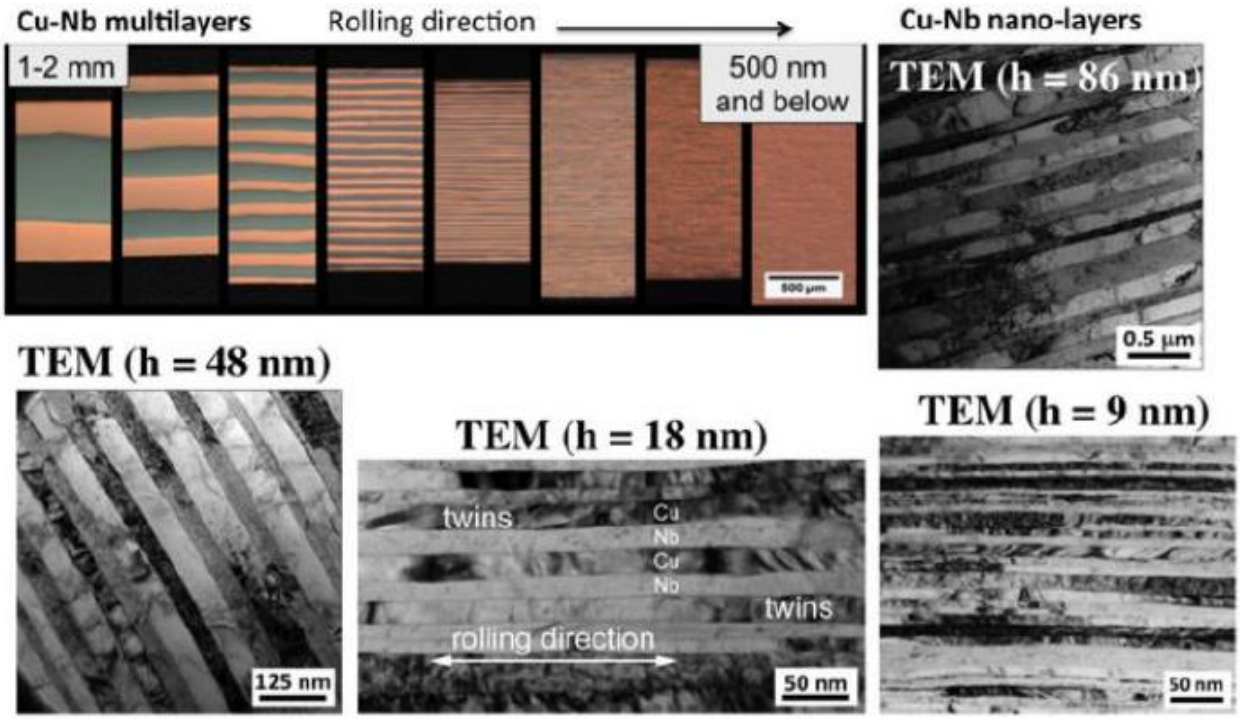

Fig. 3.1: Microstructure of ARB material at different stages of processing. In the experiments performed in this dissertation, the nominal individual layer thickness is 18 nm [2].

For comparison, multilayered Cu-Nb nanocomposites were also prepared by PVD using magnetron sputtering. Films were grown using argon gas at a pressure of 2.1×10^{-3} torr with a background vacuum pressure of 2×10^{-8} torr. For the He implantation study, the films were grown to a thickness of 2.5 μm with individual layer thicknesses of 20 nm and 90 nm on $[11\bar{2}0]$ single crystal sapphire, thus resulting in specific interfacial areas of 0.050 nm^{-1} and 0.011 nm^{-1}, respectively.

For the HPT study, films were also grown to a thickness of approximately 2.5 μm with individual layer thickness of 20 nm on 50 μm thick 110 (99.9% pure) Cu foil and to a film thickness of 6 μm on [100] single crystal Si, with a bottom layer and top layer of Ag of 25-100 nm to limit oxidation, ease welding of pieces together during HPT, and ease delamination from Si substrate. These films are shown in the SEM images in Fig. 3.2; the individual layers are flat near the substrate, but as the film increases in thickness, the layers develop a waviness. Previous research

by M. Wang performed HPT on solid solution films grown on Si [100] which were then delaminated from the substrate and stacked randomly to a thickness of about 100 μm, which is the minimum thickness to perform HPT [3]. This was also done in this study with the multilayer film grown on Si. This limits the number of samples that can be made; films grown on Cu foil allow multiple samples to be grown at one time, and HPT is easily performed sandwiching of two sets of films between thick Cu foils. However, the analysis of the samples grown on Cu foil is not thoroughly discussed in this dissertation as the deformation is predominately localized in the softer Cu foil, thus preventing analysis of the deformation mechanisms within the Cu-Nb multilayers.

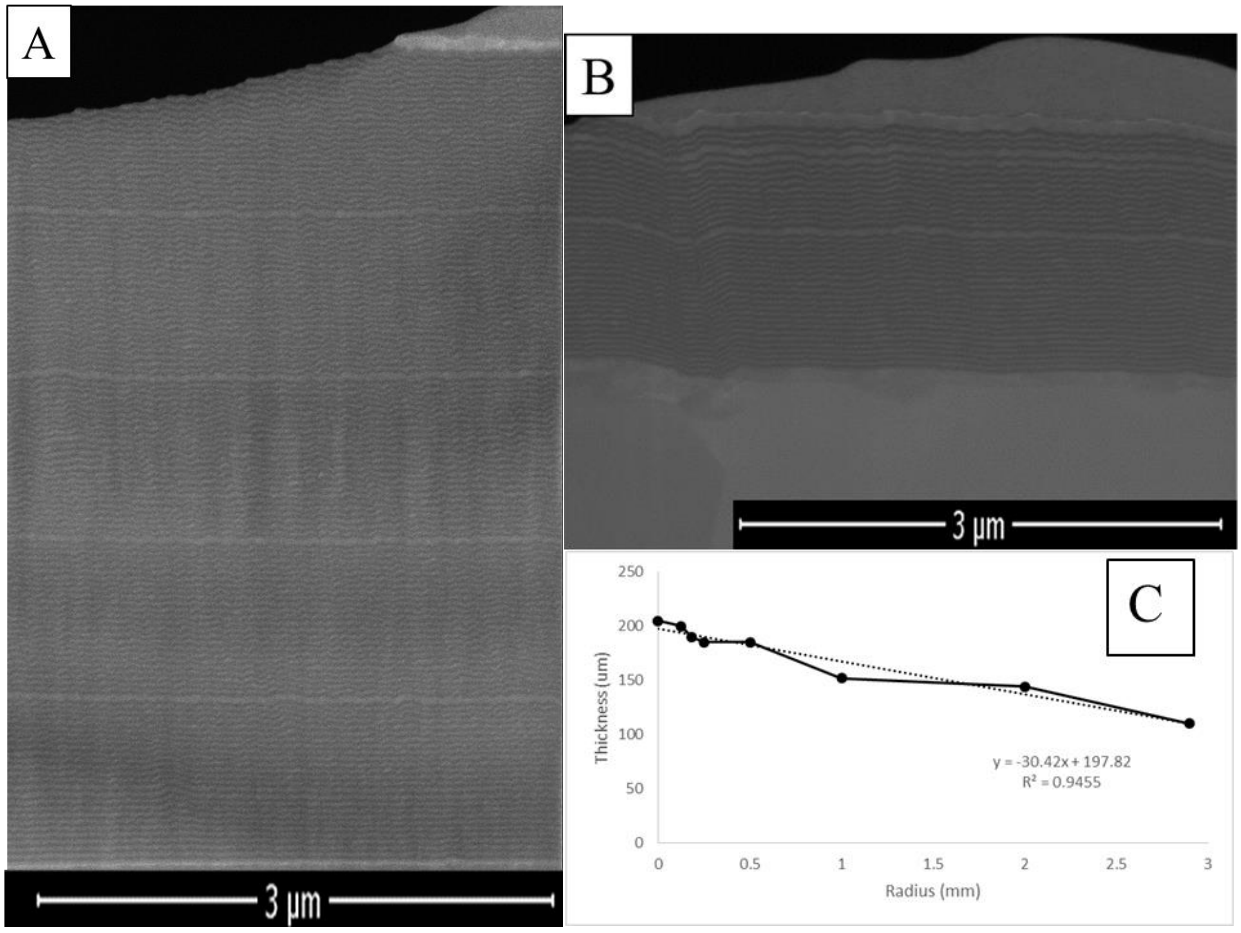

Fig. 3.2: SEM images of as-grown PVD Cu-Nb 20 nm samples grown on (a) single crystal Si and (b) Cu foil; the total thickness of the films are ~6 μm and ~2.5 μm, respectively. (c) The thickness as a function of the radius of the sample from the delaminated and stacked film after being subjected to HPT.

3.2 Fabrication and Testing of 3D Cu-Nb Nanocomposites by High Pressure Torsion and Annealing

For the SPD study, high pressure torsion (HPT) using the unconstrained geometry in Fig. 3.3 was applied to the PVD films grown on Cu foil and the stacked delaminated film pieces for comparison to previous research of HPT of ARB multilayer nanocomposites. During the HPT with an anvil diameter of one cm, pressure normal to the discs was 5 GPa; and using a rotation speed of one turn per minute, the number of turns for the films grown on Cu foil were 0.5 and 2.5 and for the delaminated material, the number of turns was five. Based on previous research in the Cu-Ag system, the unconstrained geometry allows material to flow out to the sides during deformation with a reduction in sample thickness, but the deformation is more uniform through the thickness of the samples. With the constrained geometry, the thickness remains near constant; thus the strain is calculated using equation 3.1,

$$\gamma = \frac{2\pi r N}{d} \qquad (3.1)$$

where γ is the shear strain, r is the radius of the HPT disc, N is the number of turns, and d is the thickness of the sample after HPT. However, in the unconstrained geometry, the sample thickness is not constant along the radius. Therefore, an adjusted version of equation 3.1 that takes into account the thickness variation must be used. Ekiz et al [2, 4], used equation 3.2 to account for changes in sample thickness as a function of the number of turns,

$$\gamma = \frac{2\pi r}{t(N)} dN \qquad (3.2)$$

where a calculated thickness is used based on fitting the actual local thickness as a function of the number of turns at a given radius, see Fig. 3.4. In this study with the stacked film pieces, only one sample was used with five turns; therefore, the fit from Fig. 3.4 was scaled to the geometric center thickness of ~205 μm instead of the initial ARB thickness of 380 μm.

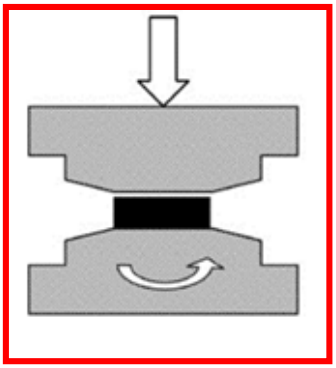

Fig. 3.3: Unconstrained HPT geometry. The anvil diameter is one cm and the normal pressure is 5 GPa.

For the He implantation study, HPT was applied to the ARB nanocomposite as described in ref. [4]; the maximum shear strain was ~ 2000. This high strain stabilizes a 3D nanocomposite structure, with a Cu grain size of ≈ 6.2 nm, and a Nb grain size of ≈ 4.7 nm, as determined by transmission electron microscopy (TEM). The specific interfacial area for these samples, based on atom probe tomography (APT) reconstructions described in ref. [28], is ~ 0.30 nm^{-1}. After HPT, some samples were annealed for one hour at 500 ˚C under high vacuum conditions, 1 x 10^{-7} torr. From x-ray diffraction using the Scherrer equation, the Cu grain size was found to increase from 6 nm to 25 nm and the Nb grain size from 5 nm to 19 nm. Based on this increase of grain sizes by a factor 4, the specific interfacial area was estimated to be reduced to ~ 0.075 nm^{-1}.

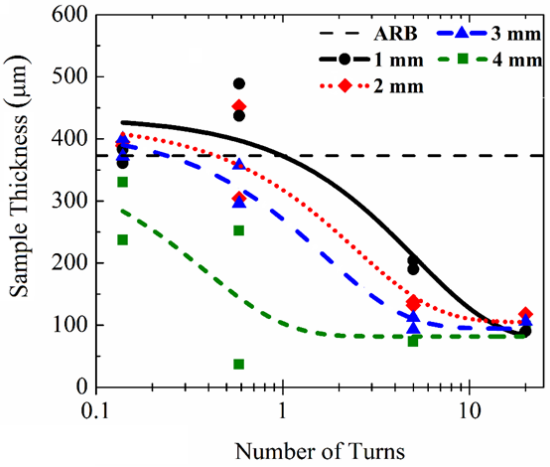

Fig. 3.4: Fitted thickness profiles of ARB material for positions of HPT samples measured at r=1, 2, 3, and 4 mm from the center of the disc after various HPT rotations. Dotted black line is the original ARB sheet thickness.

3.3 He Implantation and SRIM Simulation

The four sample sets, ARB, PVD, HPT, and HPT-annealed, were irradiated with 1 MeV He ions using a current density of ≈ 1 x 10^{13} cm^{-2}-s^{-1} to a dose of 0.8-1.6 x 10^{17} ions-cm^{-2}. To determine the distribution of the implanted He in each sample, downloadable Stopping and Range of Ions in Matter (SRIM) simulation software was used. The "Ion Distribution and Quick Calculation of Damage" model was used as it more accurately defines damage than the "Detailed Calculation with Full Cascades", according to ref. [5]. The simulation was of 1 MeV He ions implanted into 2.1 μm thick Cu-Nb 60-40 at% solid solution with a displacement energy of 25 eV for both Cu and Nb; this simulation is consistent with simulations of 50 nm thick layers and does not feature the spikes in the layered sample that result from a buildup at interfaces, as seen in the He-ion distribution plot in Fig. 3.5. The "ion/recoil distribution" file was used to plot the depth profile of He-ions to determine the He-ion density as a function of depth from the surface of the sample; a running average of the ion distribution was used to avoid the spikes seen especially at low ion concentrations due to the finite nature of the simulation. Although this method does not measure the actual He concentration, it does provide a relative measure of the critical He concentration for trapping He before bubbles form among each sample type and is accurate within ~20%, as determined in ref. [6] by using nuclear reaction analysis (NRA) that directly measures He concentration as a function of depth.

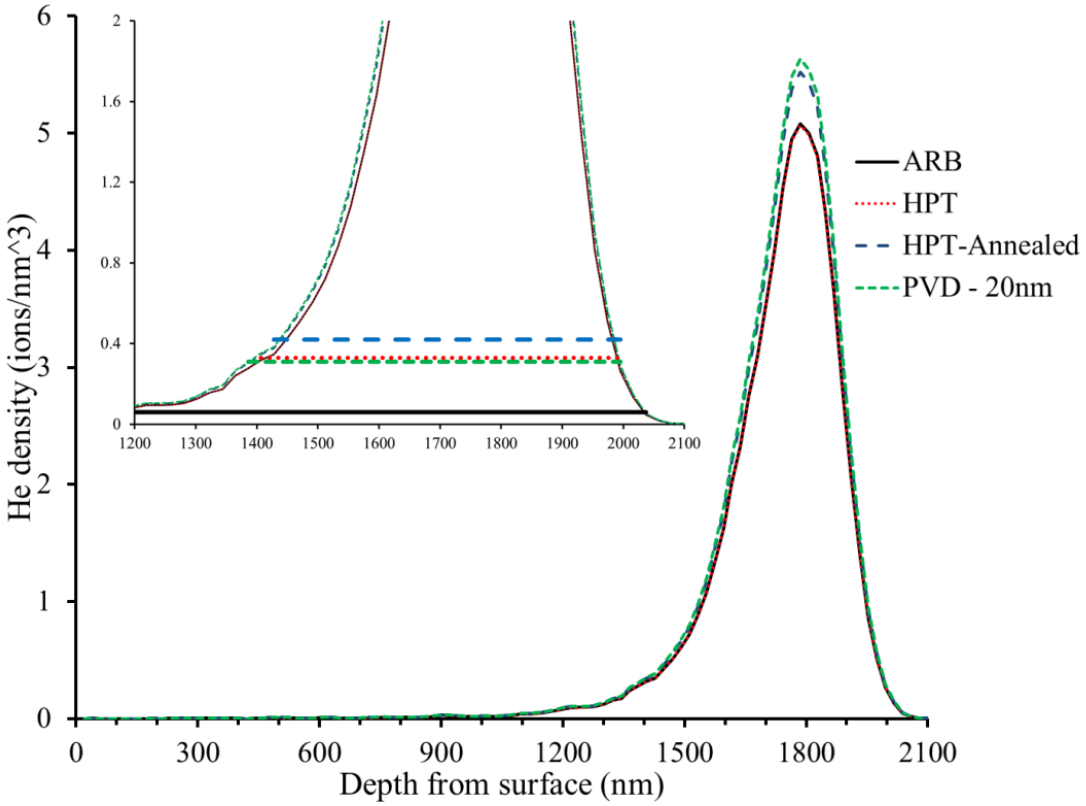

Fig. 3.5: He concentration profile in a 60-40 at% Cu-Nb alloy. Total dose ranges from 1.4×10^{17} ions/cm^2 to 1.6×10^{17} ions/cm^2.

3.4 Characterization Methods

Transmission electron microscopy (TEM) was the primary means of studying the changes the materials underwent when subjected to strain and He implantation. Bright field TEM micrographs along with selected area electron diffraction (SAED) patterns, using a JEOL 2010 LaB6 TEM, imaged the microstructural changes and diffraction contrast, in conjunction with Z-contrast scanning transmission electron microscopy (STEM), using a JEOL 2010EF STEM. Cross-sectional areas of the He-implanted regions and at various radii along the HPT'd discs were obtained using a focused ion beam (FIB) (FEI Strata Dual Beam 235 and Helios NanoLab^{TM} 600i) and conventional lift-out methods. Operating voltages from 2 kV to 30 kV and currents from 20 nA to 1 pA were selected to optimize sample quality while minimizing gallium implantation and damage.

Specifically for imaging He-filled bubbles, through-focus TEM was used for imaging the He-implanted samples. The thicknesses of the foils were between 50 and 100 nm, as measured by electron energy loss spectroscopy (EELS) on the JEOL 2010EF STEM. As the He bubbles were only a few nm in diameter, they were observed using TEM phase contrast, by acquiring bright-field images for different depths of focus, ranging from -500 nm to +500 nm [34]. In kinematic diffraction conditions, the He-filled bubbles appear bright with dark circular Fresnel fringes in under-focus and dark with bright Fresnel fringes in over-focus. Since it is difficult to achieve optimal imaging conditions everywhere at one time in nano-grained composites, the emphasis was put on achieving best visibility conditions near the transition zones defined in the next paragraph.

For each sample, under-focus and over-focus TEM micrographs were taken to determine the depths at which the first and last bubbles are visible. The widths of these regions were then compared to the He implantation profile from SRIM as shown in Fig. 3.5. The critical He concentrations for bubble formation could then be obtained from the SRIM profile as the He

concentration where the measured width of the bubble distribution equals the calculated width in the He implantation profile. The effectiveness of the interface for suppressing He bubbles was then determined by dividing the critical He concentration for bubble formation by the specific interfacial area, or interfacial area per unit volume, with the assumption that all He atoms at concentrations below the critical He concentration are absorbed at the phase boundaries.

3.5 References

[1] J.S. Carpenter, S.C. Vogel, J.E. LeDonne, D.L. Hammon, I.J. Beyerlein, N.A. Mara. *Acta Materialia* **60** (2012) 1576.

[2] E.H. Ekiz. Doctoral Dissertation: *Microstructural Evolution and Phase Stability of Cu-Nb Nanolaminates subjected to Severe Plastic Deformation by High Pressure Torsion* University of Illinois at Urbana-Champaign. (2014)

[3] M. Wang. Doctoral Dissertation: *Severe Plastic Deformation in Highly Immiscible Cu Alloys* University of Illinois at Urbana-Champaign. (2014)

[4] E. H. Ekiz, T.G. Lach, R.S. Averback, N.A. Mara, I.J. Beyerlein, M. Pouryazdan, H. Hahn, and P. Bellon. *Acta Materialia* **72** (2014) 178.

[5] R.E. Stoller, M.B. Toloczko, G.S. Was, A.G. Certain, S. Dwaraknath, and F.A. Garner. *Nuclear Instruments and Methods in Physics Research B* **310** (2013) 75.

[6] M.J. Demkowicz, D. Bhattacharyya, I. Usov, Y.Q. Wang, M. Nastasi, and A. Misra. *Applied Physics Letters* **97** (2010) 161903.

CHAPTER 4

ROLE OF INTERFACES ON MICROSTRUCTURAL STABILITY IN CU-NB NANOCOMPOSITES SUBJECTED TO HIGH PRESSURE TORSION

4.1 Introduction

Microstructural stability under harsh mechanical environments, like the large stress changes and high-temperature stress applied in nuclear reactor components, is important to ensure constancy of mechanical properties [1]. Nanocomposites of immiscible metals show great promise for use in extreme thermal, mechanical, and radiation environments; this is particularly the case for metal composites with semi-coherent interfaces [2]. As discussed in Section 2.2, research has investigated the stability of two-dimensional Cu-Nb nanolaminates when subjected to large plastic strains [3-5]. Experiments and atomistic simulation suggest that the strain path and the interface character play an important role in the stability of these nanolaminates [6-9]. One important prediction of the simulations is that interfaces with low shear strength have high stability under simple shear deformation [8]. This prediction has not yet been tested experimentally, and thus, this will be the focus of this chapter. Specifically in this study, we studied Cu-Nb multilayer nanocomposites grown by PVD for which the dominant interface is {111}KS, which is a low shear strength interface. These nanocomposites were then subjected to large shear strains via HPT. The microstructure of these nanocomposites is expected to retain a lamellar structure to a much higher strain than the ARB nanolaminates, for which the interfacial shear strength is large owing to its dominant {112}KS interface character [7, 8].

As reviewed in Chapter 2 and based on simulation, the stability of the {111}KS interfaces under shear was attributed to interfacial sliding enabled by its interface misfit dislocation structure (see Figs. 2.7 and 2.8) [6-8]. In this present work, this and other deformation mechanisms in multilayer materials subjected to HPT are sought for low interface shear strength materials in the

form of Cu-Nb multilayer nanocomposites with {111}KS interfaces grown by PVD. This work also looked to compare the deformation modes with Cu-Nb multilayer nanocomposites with high interfacial shear strength. In previous work with a collaborator, HPT has been subjected on Cu-Nb multilayer nanocomposites formed by ARB [9]. In these materials, when subjected to large shear strain using HPT, deformation takes place by dislocation motion across the interface eventually resulting in large-scale layer instability and formation of a three-dimensional structure [9]. This mechanism for deformation in high interface shear strength materials is also seen in simulation and micropillar compression experiments [8, 10]. The importance of the interface character on deformation mechanisms and structural stability in these two interfaces will be confirmed in this research.

In this chapter, the deformation tolerance and microstructural stability of the {111}KS multilayers subjected to HPT will be investigated using scanning electron microscopy (SEM), bright field transmission electron microscopy (TEM), and Z-contrast scanning transmission electron microscopy (STEM), and compared with the results of the previous study on {112}KS multilayers. Details of the procedure for sample growth using PVD and deformation using HPT were described in Chapter 3. Discussion will follow detailing the mechanisms for deformation in multilayered nanocomposites at both low and high shear strain, and contrasting these results with those of high shear strength {112}KS interfaces [9].

4.2 Results

The results presented here focus on HPT of the Cu-Nb multilayer films grown on Si, then delaminated from the substrate, cut into pieces, and stacked for HPT deformation. Films grown on Cu foil were also investigated but deformation was highly localized within the softer polycrystalline Cu even to high strain, thus limiting the information that could be obtained to the visualization of deformation mechanisms. The microstructure of the as-grown material, depicted in Fig. 4.1, and the material subjected to HPT were examined using SEM imaging, bright field TEM imaging along with electron diffraction, and Z-contrast STEM imaging. The starting material has individual layer thickness of 22±3 nm, and the film was grown to a total thickness of ~6 μm with a ~50 nm Cu layer at about every 40 layers, providing a useful marker in SEM to visualize deformation during HPT. In the as-grown samples, the morphology of the Cu-Nb nanolayers varies with the distance to the Si substrate. Near the substrate, the layers are flat and exhibit a diffraction pattern that is consistent with the {111}KS orientation relationship with one (110) reflection of Nb parallel to one (111) reflection of Cu, and normal to the interface as seen in Fig. 4.1(a). Away from the substrate in Fig. 4.1(b), the layers are wavy and periodic in nature with an amplitude of no more than the layer thickness. Development of wavy layers because of kinetic roughening is common among thick multilayer films grown by PVD [11], and the diffraction pattern in the wavy part of the film depicts a more random orientation. This variation will somewhat complicate the analysis of the interface and texture evolution after HPT deformation. Despite these variations in the local layered structure and texture, the overall stability of the layered structure and its potential transition to a three-dimensional morphology can still be clearly investigated.

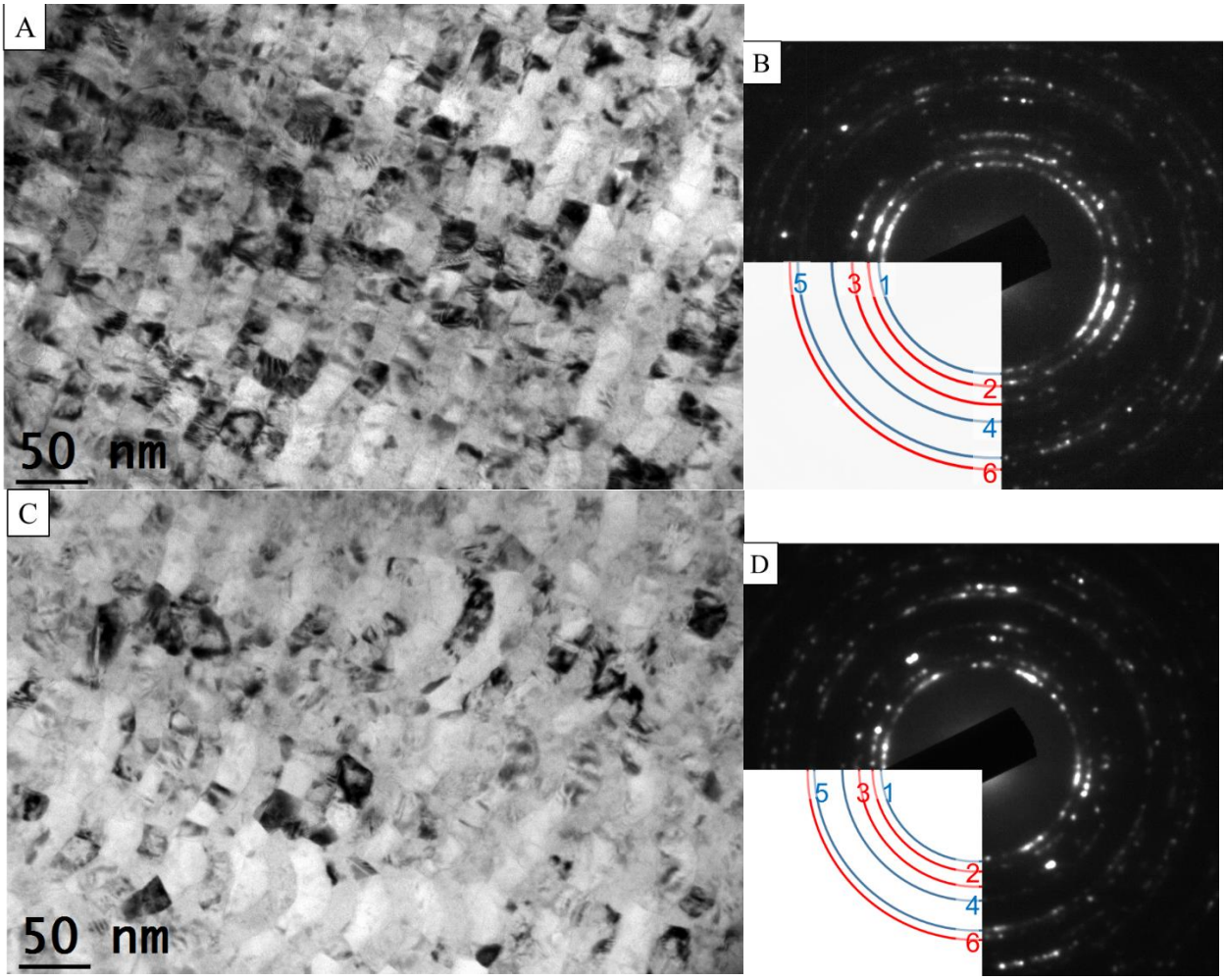

Fig. 4.1: Bright field TEM micrographs of Cu-Nb PVD material grown on Si substrate and delaminated. (a) Region near the initial layer growth: layers are flat, and diffraction pattern (b) shows consistency with the {111}KS OR. From inside out, the peaks are 1: Nb (110), 2: Cu (111), 3: Cu (200), 4: Nb (200), 5: Nb (211), and 6: Cu (220). (c) Region away from substrate: layers are wavy, and diffraction pattern (d) shows a more random orientation. Peak rings are the same as (b).

The film pieces were stacked and subjected to HPT as outlined in Section 3.2. Taken from the cross-section of the HPT'd material, cross-section TEM foils were prepared using dual-beam SEM/ FIB. SEM and TEM micrographs were produced at different radii imaged in the plane of the normal direction (ND) and shear direction (SD) of the sample disc, see schematic in Fig. 4.2, to analyze the microstructural evolution of the material with increasing shear strain and to determine the mechanism for deformation. The radii at which SEM/ TEM foils were taken for this study are shown in Table 4.1; the thickness was measured by SEM, and the strain was calculated

using equation 3.2, which assumes the strain is homogeneous through the thickness. This assumption will be revisited in the discussion section. In order to investigate the material after compression but without shear deformation we first analyze the center of HPT'd disc, since the shear strain is ideally zero at the geometric center. As depicted in Fig. 4.2, the microstructure has a strong texture consistent with the {111}KS orientation normal to the layers, as expected. The individual layer thickness has been slightly reduced to about 16-20 nm. There is some larger scale kinking and bending of layers as evidenced on the left side of Fig. 4.2(a), but at this point, it is due to the non-uniform nature at and near the center of the HPT'd disc.

Table 4.1: Radius of each SEM/ TEM sample studied, with corresponding thickness and calculated strain

Radius (mm)	**Thickness (μm)**	**Strain - Fit dγ/dN**
0	205	0
0.125	200	19
0.18	190	29
0.25	185	40
0.5	185	81
1.0	152	173
2.0	144	357
2.9	110	685

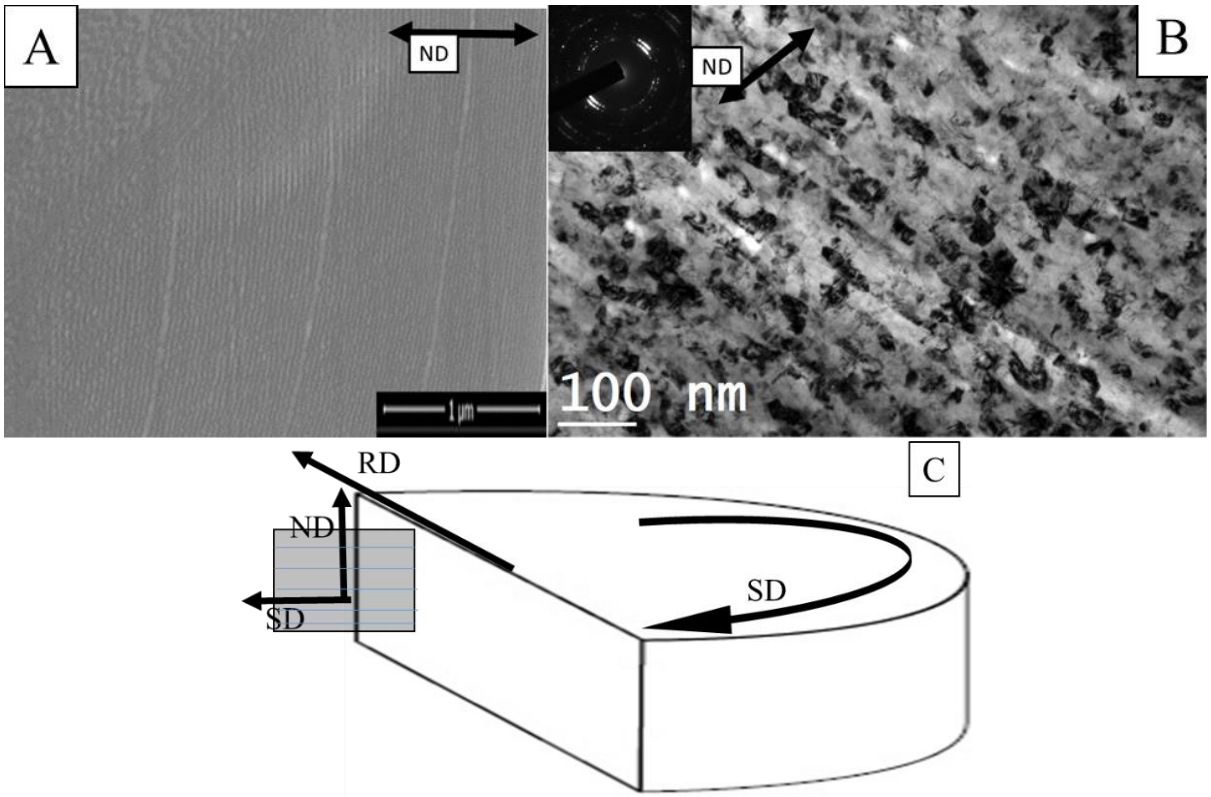

Fig. 4.2: (a) SEM and (b) bright field TEM micrographs of Cu-Nb PVD grown multilayer material at the geometric center of HPT'd disc; the disc normal is roughly along the arrows shown. The diffraction pattern (inset) shows consistency with {111}KS normal to the layers. (c) Schematic of image plane from sample after HPT taken at several points along radial direction (RD); image planes are formed by normal direction (ND) and shear direction (SD). Film pieces were stacked along ND.

The microstructural evolution of the material with increasing HPT shear strain was investigated using SEM, bright field TEM, and Z-contrast STEM. Using SEM imaging, there were large regions of multilayers approximately microns in size that remain relatively unchanged in structure up to strains of ~81. This is particularly the case when the layered structure is oriented near-parallel to the shear direction. As the orientation of layers changes to off-parallel at these strains, there is evidence of mechanisms – kink banding and grain rotation – in the local microstructure for the large scale deformation that exists at higher strains. As will be presented in this section, utilizing the higher resolution of TEM and STEM imaging, regions of multilayers

oriented near-parallel are still visible up to a strain of ~357. The layer stability and microstructural evolution with increasing strain will be detailed further at each strain studied.

At a strain of ~19, the film pieces are bent, as shown in Fig. 4.3(a), but locally the layered structure is still intact and appears similar to the geometric center, see Fig. 4.2. In these regions, the interfaces are sharp and the layer thickness has not changed further, as depicted in the bright field TEM micrograph in Fig. 4.3(b). The inset electron diffraction pattern exhibits consistency with the {111}KS orientation normal to the interface plane, though there are now additional weak (110)Nb and (111)Cu reflections parallel to each other. In other parts of the sample, there are regions where the layered structure is destabilized; as depicted in the boxed regions in Fig. 4.3(c), kink bands cause the layers to bend and buckle and in some regions form swirls. The layers near these bends, such as in Fig. 4.3(d), are slightly wavy, and the layer thickness has been reduced to ~10-15 nm; the interfaces are sharp, but the texture of these layers has changed as represented in the inset electron diffraction pattern. The texture, though, cannot be fully quantified by electron diffraction in these nanostructured materials. Z-contrast STEM imaging, as shown in Fig. 4.3(e, f), confirms that near bent regions, layers exhibit waviness and/ or are reduced in thickness, though the amount of waviness is approximately the same as in the as-grown material away from the substrate. At the center of these regions, swirl-like features are pronounced depicting rotation of layered regions, see Fig. 4.3(f).

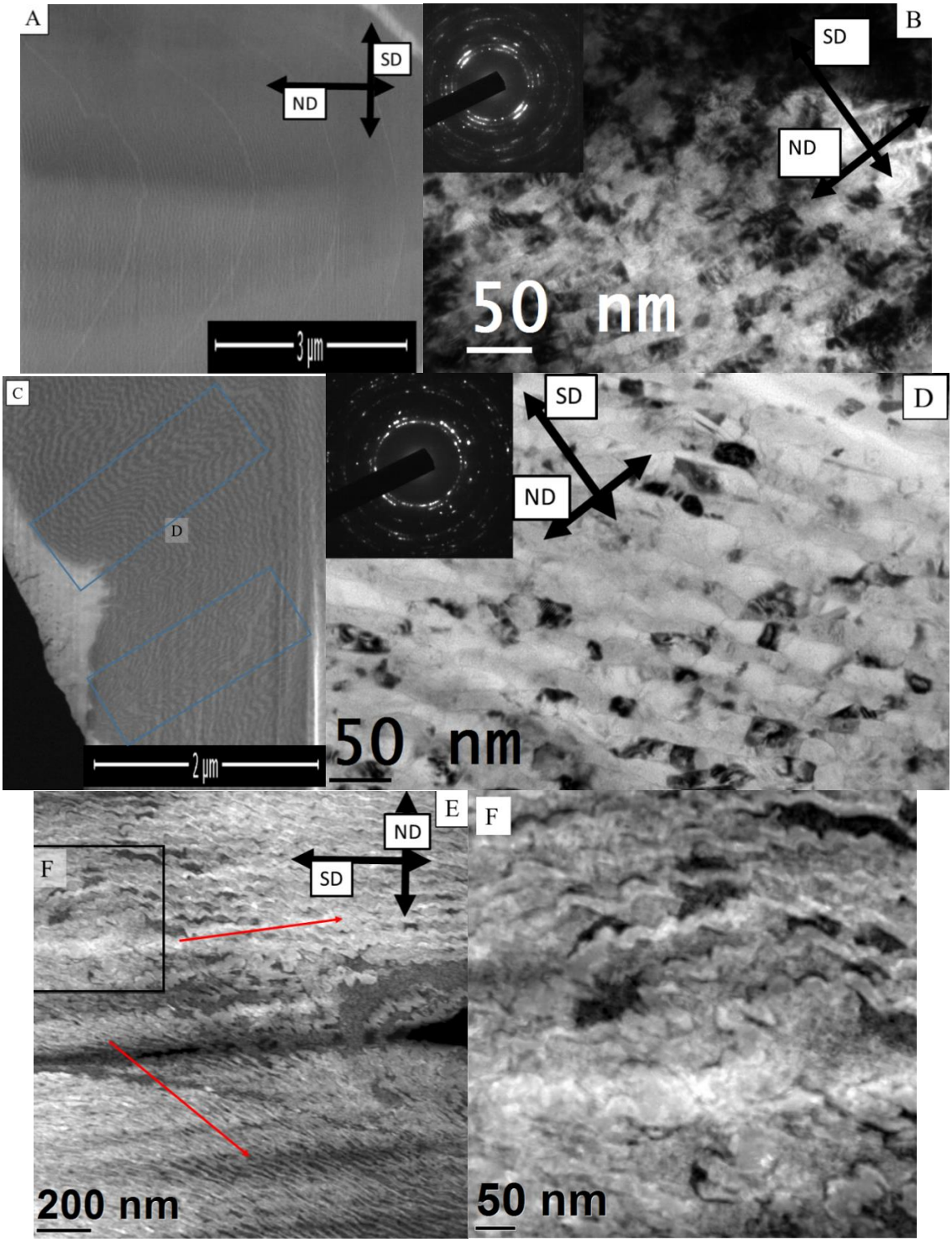

Fig. 4.3: Cu-Nb PVD sample HPT'd, taken at radius of 0.125 mm with a strain of ~19. SEM images (a) depicting slightly bent film piece. Bright field TEM micrograph (b) of layered region that has flat layers with sharp interfaces; inset electron diffraction pattern shows strong texture consistent with {111}KS OR. SEM image (c) of kink bands that bend and buckle layers. Bright field TEM micrograph (d) near kink band showing thinned layers and rotation of diffraction pattern away from {111}KS OR. Z-contrast STEM micrographs (e, f) of swirl-like features apparent at location of a bend in layers.

At a strains of ~29 and ~40, layered regions comprise a large portion of the samples as seen in Figs. 4.4(b) and 4.5(b); though there are still noticeable regions that have bends, swirls, and kink bands as depicted in Figs. 4.4(a) and 4.5(a). There is still some texture normal to the interfaces that is consistent with the {111}KS OR in layered regions, see diffraction patterns in Figs. 4.4(e) and 4.5(b); though particularly at a strain of ~40, there are other weaker (110)Nb and (111)Cu reflections indicative of some grain rotation. In the SEM image in Fig. 4.5(b), it is clear that the shear direction is not necessarily parallel to the layers throughout the sample as two pieces are oriented at a non-trivial angle to one another. The original purpose of this research was to observe the evolution of the multilayers parallel to the shear direction, but the orientation of film pieces non-parallel to the shear direction provides an opportunity to evaluate the stability of interfaces non-parallel to the shear direction. At many locations there is evidence of kink and shear banding, multiple layer bending, layer orientation changes (parallel vs. normal to shear direction), or impingement of two non-parallel sections on each other, as evidenced in the SEM images in Fig. 4.4 (a, b) of the material at strain of ~29. In some regions the layers are bent or rotated and in other large regions, the layers remain parallel to each other and the shear direction. But in other locations, there is a loss of the local layered structure, where there is large scale bending and kinking, see Fig. 4.4(c, d) or impingement of two regions on each other, see Fig. 4.5(d). There is also a noticeable reduction in layer thickness and grain size to ~10-16 nm at a strain of ~40, see Fig. 4.5(c, d), and a move towards a more random orientation in the diffraction pattern seen in Figs. 4.4(d) and 4.5(d) as there is now six-fold symmetry of both the (110)Nb and (111)Cu reflections.

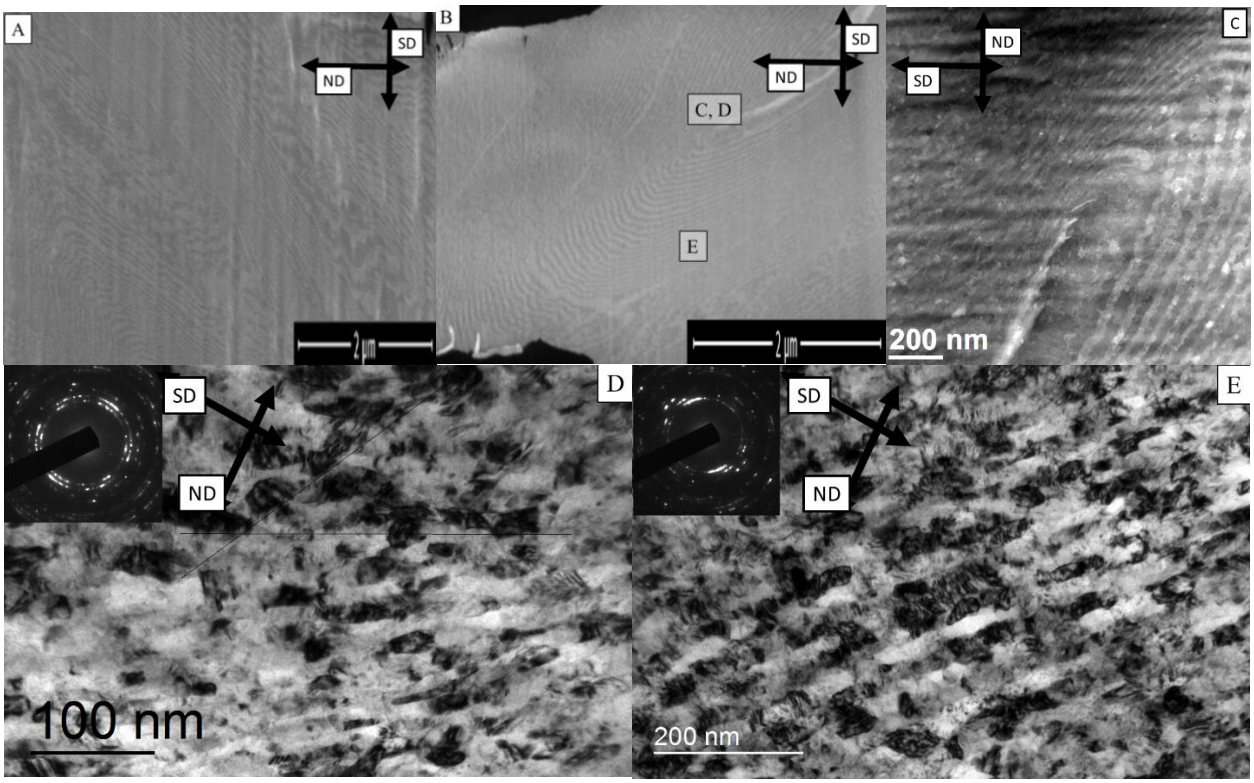

Fig. 4.4: Cu-Nb PVD sample HPT'd, taken at radius of 0.18 mm with a strain of ~29. SEM images (a, b) with Z-contrast STEM (c) and bright field TEM micrographs (d) taken from sharp bend seen in (b); location at sharp bend results in loss of layered structure and move towards a random orientation. Away from bend (d), diffraction pattern is strong normal to the layers.

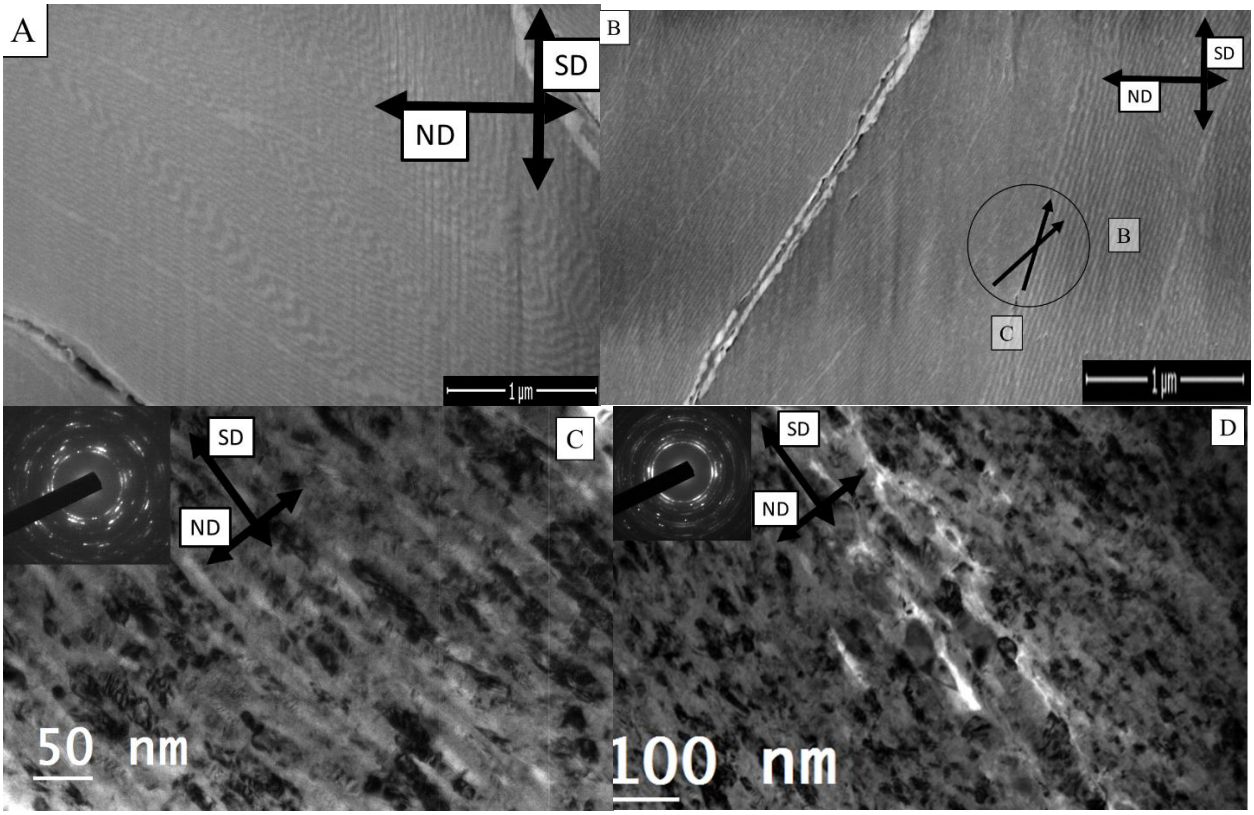

Fig. 4.5: Cu-Nb PVD sample HPT'd, taken at radius of 0.25 mm with a strain of ~40. SEM images of (a) kink bands running through layered regions of sample and (b) of layered sections oriented along shear direction but not parallel and impinging on each other, see arrows within circled region indicating layer orientation. In layered area (c) bright field TEM micrograph and diffraction pattern show not much evolution. At impinged area in (d), the grain size is reduced and orientation becomes more random.

The microstructure gradually evolves as the strain is increased to ~81. The same features displayed at lower strains are still present at a strain of ~81; large regions of multilayers near parallel to the shear direction coexist with large regions that have kinks and bends, see Fig. 4.6. On the left side, a full set of layers appear to be parallel to each other, while on the right side, there is large scale bending and kinking of layers. Based on the large light layer, which is the Ag layer the Cu-Nb multilayers were grown on, these two areas are two separate pieces of film that have impinged on each other, showcasing that deformation is localized resulting in layers with different orientation with respect to the shear direction. It is interesting to notice that the layers non-parallel to the shear direction are more irregular in shape. As depicted in the boxed region, a shear-induced

kink band has caused the layers to rotate because the layers are still connected to regions outside the box but appear thicker; this appearance is likely a result of the limitations of SEM imaging through the thickness of the image plane.

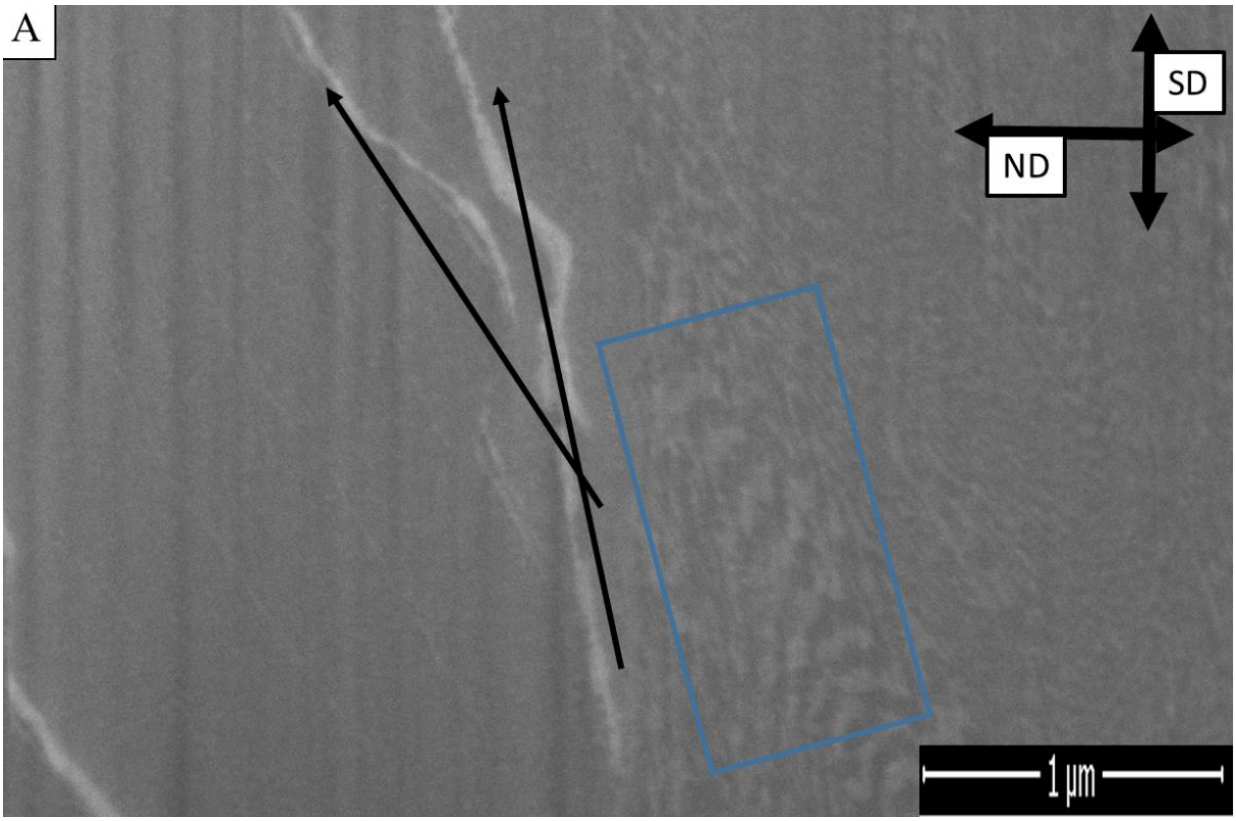

Fig. 4.6: Cu-Nb PVD sample HPT'd, taken at radius of 0.5 mm with a strain of ~81. SEM image of layered sections on left oriented along shear direction impinging on another region that shows large scale kinking and layer bending. Boxed region depicts layer rotation within kink band.

As strain is increased to ~173, the stability of the layered structure on a large scale is reduced. In the SEM image in Fig. 4.7(a), there are no regions with relatively flat layers, whereas kinked and bent layers are visible throughout. However, utilizing bright field TEM and Z-contrast STEM shown in Figs. 4.7(b-e), layered regions oriented parallel to the shear direction coexist with swirl-like regions and regions that have a three-dimensional, equiaxed microstructure. This is the first strain at which a "mixed" state in the microstructure is observed in bright field TEM, where layers coexist with large regions of three-dimensional, equiaxed grains, as is depicted in Fig.

4.7(b). The corresponding diffraction patterns in Fig. 4.7(b) show that the texture in the layered structure has rotated slightly away from the {111}KS OR, as the strongest (110)Nb reflections are no longer entirely parallel with the strongest (111)Cu reflections and are not normal to the interface. This is still in contrast to the three-dimensional region that exhibits a more random diffraction pattern. The Z-contrast STEM micrograph in Fig. 4.7(c) also show the layered structure coexisting with equiaxed grains; there is evidence of layers pinched off in some locations, which serves as the onset the transformation to the three-dimensional structure and for the swirl-like features, which are more clearly depicted in Fig. 4.7(e); these features display Cu and Nb phases swirling together. The feature size in all three regions is approximately the same, as both the layer thickness and grain size in the three-dimensional regions have been reduced to ~5-10 nm in thickness or diameter, another likely reason why layered regions can no longer be seen in SEM imaging, despite the layered region in Fig. 4.7(d) is about 2 μm across.

Further increasing the HPT strain to ~357, see Fig. 4.8(a), the "mixed" state in the microstructure resembles that of the microstructure at a strain of ~173. The microstructure consists of a layered structure with thinned layers coexisting with three-dimensional regions of both equiaxed as well as elongated grains, as observed in the bright field TEM micrographs Fig. 4.8(b, c) and the Z-contrast STEM micrographs in Fig. 4.8(d, e). The equiaxed region has a similar electron diffraction pattern to the 3D state at a strain of ~173; however, the diffraction pattern for the layered region is slightly different as two sets of (110)Nb and (111)Cu reflections are entirely parallel with each other, with one set lying normal to the interfaces. This is not necessarily consistent with the {111}KS texture, but it does show the microstructure potentially evolves at different rates in different regions. At this strain, many regions with a three-dimensional structure

have not become equiaxed and have elongated grains parallel with the shear direction, see Fig. 4.8(e).

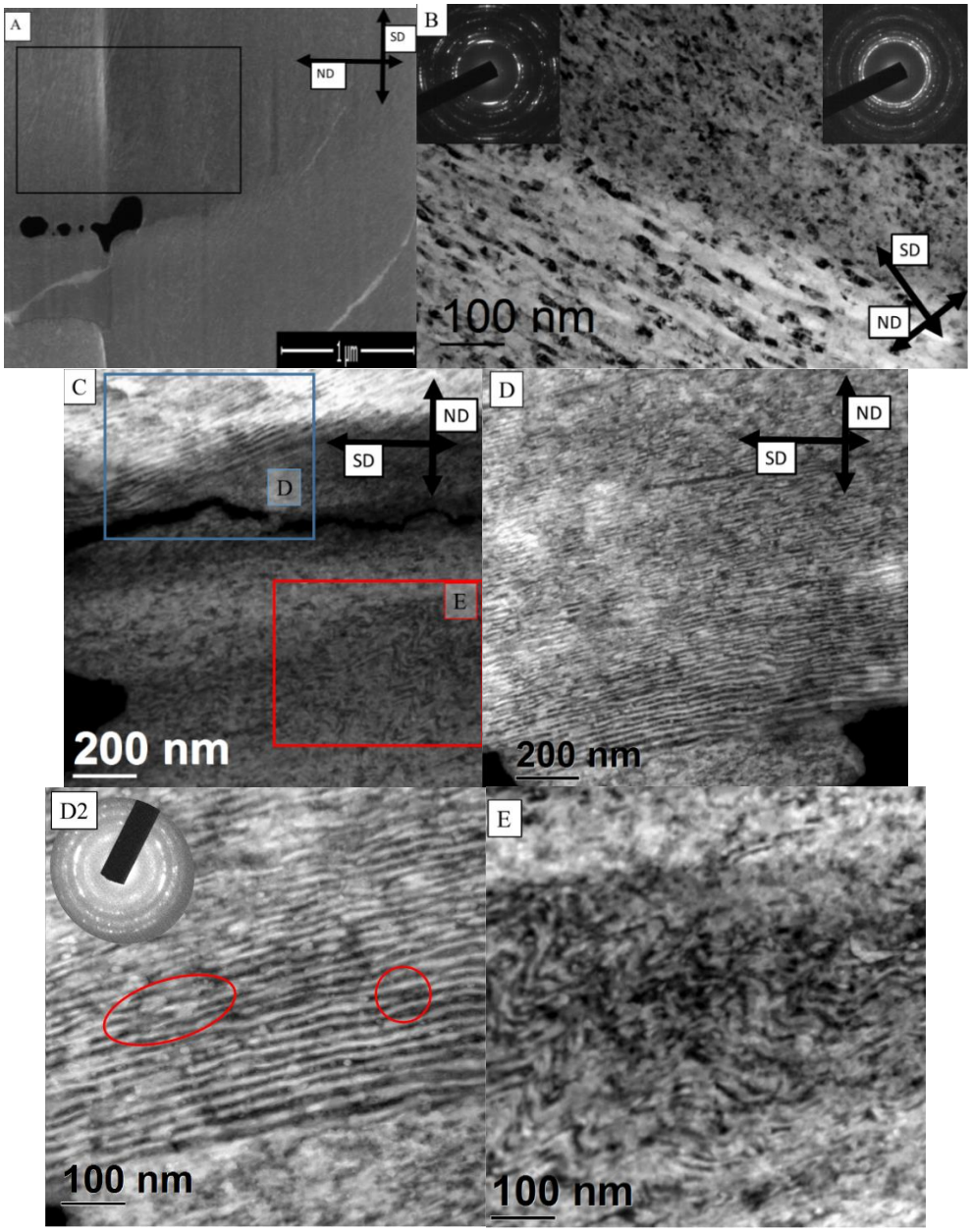

Fig. 4.7: Cu-Nb PVD sample HPT'd, taken at radius of 1.0 mm with a strain of ~173. SEM image (a) with some layered regions oriented along shear direction but mostly large scale kinking and layer bending. Bright field TEM micrograph (b) showing layered structure coexisting with equiaxed 3D structure. Inset diffraction patterns show that layers still have {111}KS-like orientation and 3D structured regions appear randomly oriented. Z-contrast STEM micrograph (c) from boxed region in (a) depicting layers (d, d2) with pinched regions (circled in red), swirls (e), and 3D equiaxed structures coexisting near each other.

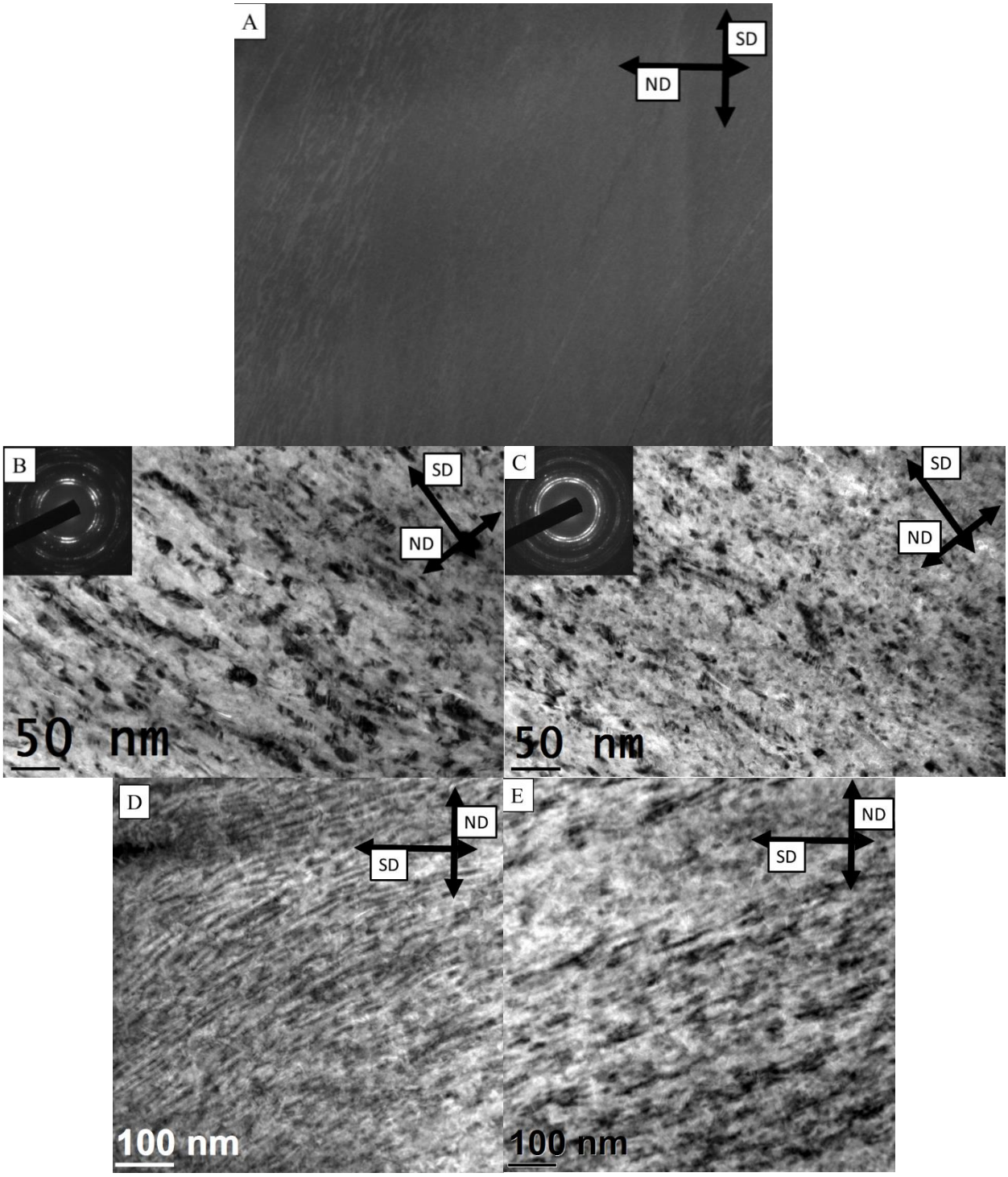

Figure 4.8: Cu-Nb PVD sample HPT'd, taken at radius of 2.0 mm with a strain of ~357 as seen by SEM imaging (a). Bright field TEM micrographs showing layered region (b) and 3D structure (c). Inset diffraction patterns show that layers exhibit strong texture between Cu and Nb, and 3D structure appear randomly oriented. Z-contrast STEM micrographs showing layered region (d) and 3D structure with remnants of initial structure (e).

At a large strain of ~685, the microstructure has almost been fully transformed into a three-dimensional nanocomposite. As depicted in Fig. 4.9, there are no observed regions of multiple layers lying parallel to each other. The material has mostly equiaxed grains, but there are instances where there are elongated grains, see the bright field TEM micrographs in Fig. 4.8(b, c). The inset diffraction patterns indicate that the orientation of the grains is almost random. At this strain, the material has not reached a steady-state microstructure, as there are regions that still appear to align with the shear direction, see the elongated streaks and grains in the Z-contrast STEM micrographs in Figs. 4.9(d, e).

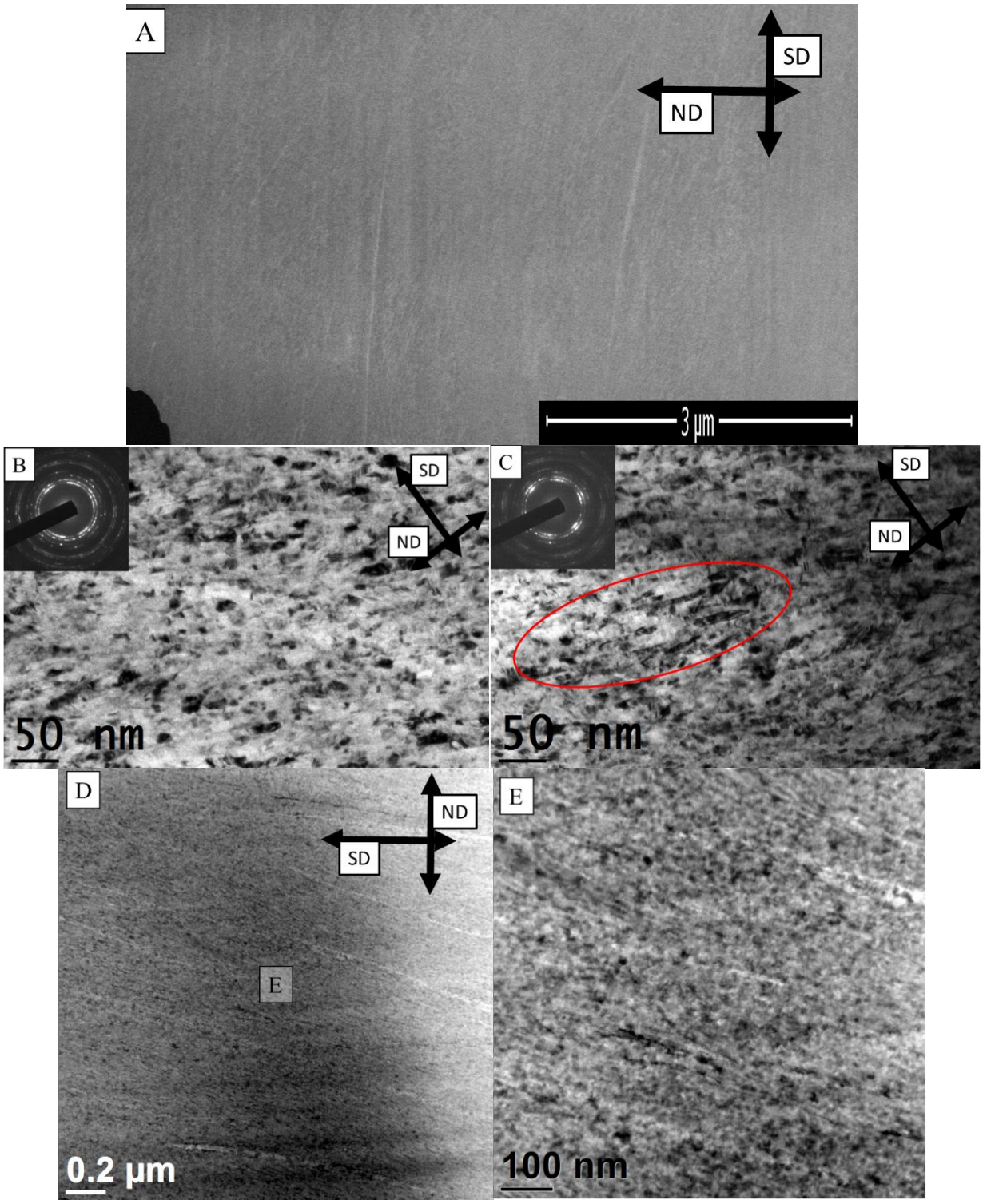

Fig. 4.9: Cu-Nb PVD sample HPT'd, taken at radius of 2.9 mm with a strain of ~685. SEM image (a) showing nearly fully transformed 3D equiaxed microstructure, though much of the region appears oriented parallel to the shear direction. Sample bright field TEM (b, c) and Z-contrast STEM (d, e) micrographs of microstructure show nearly fully transformed 3D structure, though some grains appear to be elongated from left to right, see red circled region, and elongated streaks in (d).

XRD was performed on the general area of nearly transformed material, roughly in the region of 1-3 mm radius which represents a strain of ~200 - ~800, see the pattern in Fig. 4.10. This pattern is characteristic of immiscible metal composites subjected to severe plastic deformation with broadening of all peaks and drastic decrease in the intensity of high-angle peaks noise due to a grain size reduction and some chemical mixing. Using the Scherrer equation on the Nb(110) peak and Cu(111) peaks, at roughly 39º and 43º, respectively, the grain size is approximately 4.9 nm and 6.5 nm, respectively; this is consistent with the grain size and layer thickness at ~5-10 nm of the material at and above a shear strain of ~173.

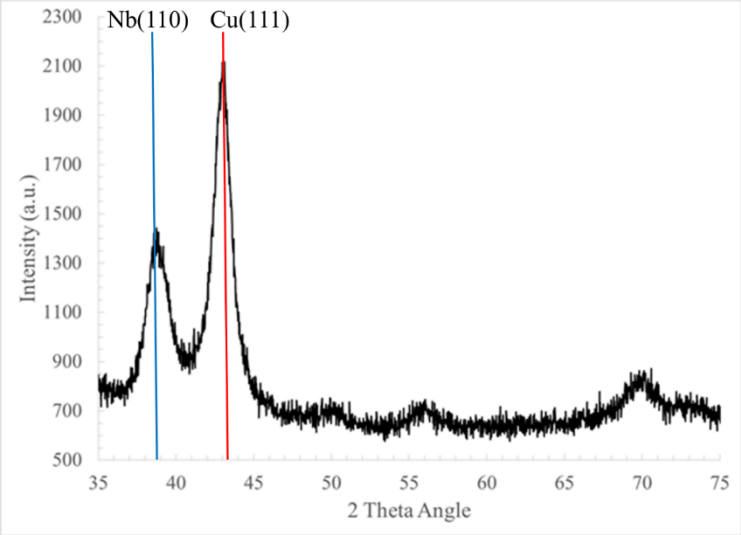

Fig. 4.10: X-Ray Diffraction pattern of whole sample. Characteristic of a highly deformed material with reduced grain size, which was about 4.9 nm for Nb and 6.5 nm for Cu.

4.3 Discussion

HPT has been employed to evaluate the stability of PVD-grown Cu-Nb multilayered nanocomposites with the {111}KS interface character to large shear strains. HPT shear strain led to drastic morphological and microstructural evolutions of the Cu-Nb multilayered nanocomposite, eventually leading to the destabilization of the two-dimensional multilayers in favor of an ultrafine three-dimensional nanocomposite, similarly to the Cu-Nb multilayered nanocomposite formed by accumulative roll bonding (ARB) with {112}KS interface character [9]. The path or mechanisms to reach the three-dimensional structure, however, are different and take place over a much larger strain range; thus we will discuss the deformation mechanisms found in the PVD-grown multilayers. For PVD-grown material with an initial layer thickness of ~20 nm investigated here, the deformation modes of the layered structure subjected to high shear strain via HPT, as revealed by SEM, bright field TEM, and Z-contrast STEM analysis, can be broken up into two related but different regimes: regions where the layered structure is oriented near-parallel to the shear direction and regions where the layered structure is aligned off-parallel to the shear direction. The original intention of this project was to investigate the deformation mechanism of {111}KS interfaces subjected to shear strain parallel to the interface plane; however, as seen in SEM and bright field TEM imaging, the effects of the stacking of film pieces and the HPT process itself has caused layers to be oriented both near-parallel and off-parallel to the shear direction. At relatively high strain, in all regions where layers remained, the layering direction is nearly parallel to the shear direction; thus, suggesting that any layers that existed non-parallel to the shear direction at low strain either re-aligned or deformed into a three-dimensional structure. Therefore, first, we will focus our attention on the deformation mechanisms seen in the layered structure oriented near parallel to the shear direction for direct comparison with the ARB-fabricated Cu-Nb

multilayer nanocomposites investigated previously, with an initial nominal layer thickness of 18 nm and oriented initially parallel with the shear direction. After which, we will discuss the interesting features of the deformation in regions oriented off-parallel to the shear direction.

The multilayered structures oriented near parallel to the shear direction remained mostly stable up to strains of ~81 as seen in SEM imaging and large regions were still visible in bright field TEM and Z-contrast STEM imaging up to strains of ~357, though at higher strains it is evident that the layer thickness had been reduced by about a factor of two. This is in stark contrast to the ARB-fabricated material which remained globally stable only up to strains of ~10 before destabilizing into a "mixed state" at a strain of ~70 and a fully three-dimensional nanocomposite by a strain of ~286 [9]. This large difference is essentially consistent with simulation on shear strain of weak {111}KS interfaces and strong {112}KS interfaces, as presented in Chapter 2 [6-8]. Furthermore, compared to this same ARB material, the PVD-grown material had yet to transform to a fully three-dimensional structure at a strain of ~685; a factor of 2-3 times larger than the ~286 for the ARB-fabricated material. The similarities and differences in layer stability, deformation mechanism, and microstructural evolution between the two materials will now be discussed in detail.

In previous molecular dynamics simulations, under simple shear strain parallel to interfaces, the primary deformation mechanism is interfacial sliding for multilayered materials with weak interfaces, such as the Cu-Nb {111}KS interface, where layers slide along the interface plane as dislocations are attracted to the interface and are accommodated within the interface plane without crossing through the interface [12, 13]. This is in contrast to strong interfaces, such as the Cu-Nb {112}KS interface, where dislocations are able to pass through the interface with relative ease, promoting chemical mixing and layer destabilization [6, 7, 9]. Using HPT on PVD-grown

material where multiple pieces are stacked imperfectly, it is difficult to directly observe this deformation mechanism. However, insights from the results presented here strongly suggest that interface sliding is a prominent deformation mechanism. As seen in Figs. 4.2 – 4.4, at strains of 0 - ~29, large regions of parallel layers are observed regardless of whether the interface alignment is normal or parallel to the shear direction. As the strain is increased, where layered regions remained, the layering direction is only aligned nearly parallel to the shear direction, and up to a strain of ~173, the electron diffraction patterns in layered regions exhibit some consistency with the {111}KS OR, though there is clearly evidence of grain rotation away from this texture. Elsewhere, the layers have transformed into a three-dimensional structure, likely due to the orientation of the layers with respect to the shear direction. In addition, the layered structure is still locally stable up to very high shear strains, up to ~357, before the morphology is changed completely to a three-dimensional structure, suggesting stability of the layered structure with low shear strength interfaces. Since the interfaces have a low shear strength, they are prone to be sheared more easily than in other directions; thus stabilizing the layered structure relative to other regions oriented off-parallel to the shear direction. The heterogeneity of the microstructural evolution, though, may be a result of multiple deformation mechanisms beyond interfacial sliding that also includes grain rotation and reduction of layer thickness, kink and shear banding, and shielding by preferred deformation in nearby regions.

While interfacial sliding is likely present, the evolution of the electron diffraction patterns away from patterns consistent with the {111}KS orientation with increasing strain means that grain rotation must have taken place; this rotation is a form of deformation itself. It also correlates with a reduction in layer thickness. The initial compression with limited shear strain at the geometric center reduces the layer thickness slightly to about 16-20 nm but with no change in texture.

However, as the strain increases, the layer thickness decreases most when the electron diffraction patterns begin to change away from the {111}KS OR. Away from any bends or folds, as the layer thickness decreases to about ~10-16 nm at a strain of ~40, the diffraction patterns also exhibits more (110)Nb and (111)Cu reflections that are either non-parallel with each other or are not oriented normal to the interfaces, see Fig. 4.5(c). This is further realized with increasing strain to ~173 and ~357, as reflections in the diffraction patterns rotate further away from {111}KS or other reflections become stronger, and the layer thickness is reduced to ~5-10 nm – the same size of grains in three-dimensional, equiaxed grain regions. The disorientation of layers along with layer waviness likely make it easier for dislocations to cut through the interface, and thus allowing for layer thickness to be reduced and grains to be rotated. This same phenomenon has been seen in simulation where interface roughness and large step sizes allows for interfacial mixing to happen more readily [6].

Another deformation mechanism that is prominent in the multilayers oriented near-parallel to the shear direction is multilayer kink or shear banding. The kink and shear bands are localized plasticity perpendicular to the layers that causes the layers to bend and fold on each other. These kinked or buckled regions are visible in multiple locations at different strains in the sample, such as at a strain of ~29 in Fig. 4.4(a) and a strain of ~81 in Fig. 4.6. Near the center of these bends and folds, the radius of curvature of the layers becomes very small and the layered structure is lost locally. These kinks are either induced by local microstructural inhomogeneities or by local changes in the shear direction. Similar features are also seen in the Cu-Nb ARB-fabricated material with 18 nm and 2 μm initial layer thickness subjected to HPT, see Fig. 4.11 [9, 14]. In both the PVD-grown material with 20 nm layer thickness and the ARB material with 18 nm layer thickness, the kinks appear similar and nearby layers are still flat, however the kinks in these materials are

on different length scales. The small scale kinking in the ARB-fabricated multilayers involves only a few layers, while the kinking in the PVD-grown multilayers involves many layers up to entire pieces of film. This may be a result of easier slip transmission across the interface in ARB-fabricated multilayers, and layers likely became destabilized at such a low strain before larger scale kink bands could form, whereas lack of slip transmission in the PVD-grown material may necessitate bending of several layers or whole pieces of film. It is interesting to note that the ARB-fabricated material with a much larger initial layer thickness of 2 μm exhibits kink or shear bands and larger scale layer bending, see Fig. 4.11(b), likely because more strain is required to destabilize the layer structure [14], thus suggesting that large scale kink or shear bands and multilayer bending only form if the layered structure is relatively stable.

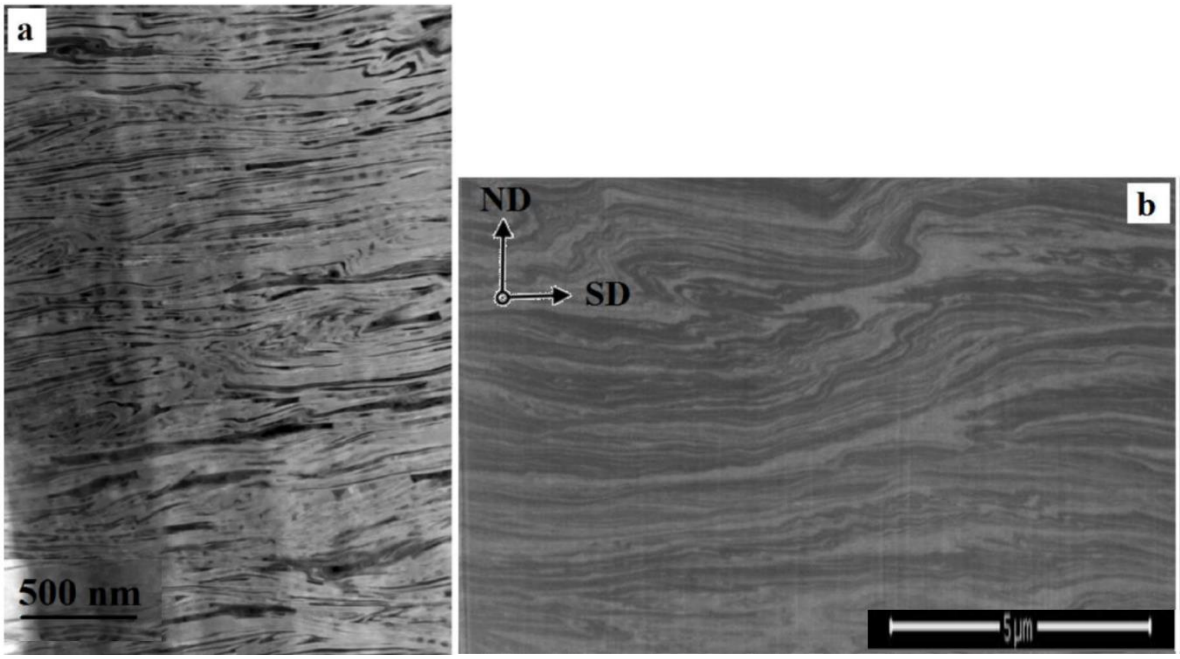

Fig. 4.11: (a) Z-contrast STEM micrograph of Cu-Nb ARB multilayer material with 18 nm initial layer thickness subjected to an HPT shear strain of ~10.8. Small scale bending and kinking of the layers are present locally. (b) SEM image of Cu-Nb ARB multilayer material with 2 μm initial layer thickness subjected to HPT shear strain of ~60. Larger scale layer bending near a kink band is present. The length scale difference of kinks may depend relative ease to destabilize layers.

The large scale bending and kinking of many layers is also found in geological formations of sedimentary rock that undergoes shear deformation by gravitational forces or shifting of tectonic

plates [15-17] and in other multilayer metals [18]. Though they are on drastically different length scales, the information gleaned from shear of rock formations may be helpful for understanding the deformation phenomena in the present study. Fig. 4.12 shows examples of folding (a) and simulation of these folds using viscous multilayers with alternating strong and weak layers subjected to simple shear (b) and gravity sliding (c, d) [17]. In the simulations, the layers are immiscible and have a difference in relative viscosity; this last assumption is likely to be valid in Cu-Nb, since this system has a moderate difference in strength and hardness between the phases. Under simple shear, a small perturbation, shown in the inset at $\gamma = 0$ in Fig. 4.12(b) as a small step at one interface, causes the folding to occur at this location, which grows in size as shear strain increases. This is consistent with simulation results on Cu-Nb multilayers discussed in Chapter 2 as the sudden transition from no mixing across the interface to large-scale mixing is compatible with a perturbation in the interface structure [6-8]. In the Cu-Nb system in this study, a similar perturbation could include the wavy layers that form away from the substrate, see Fig. 4.1(b). Similarly, folding results in viscous multilayers during "gravity sliding", as depicted in Figs. 4.12(c, d), where a perturbation is shown as a shear stress applied at an angle to the multilayers; the folding increases in size when the angle and magnitude of the shear stress increases. This mechanism could also operate in the present study as Cu-Nb film pieces are not always oriented parallel to the shear direction applied during HPT. This mechanism appears also to be consistent with the results that at high shear strain, where layered regions are only observed when the layers are oriented near parallel to the shear direction.

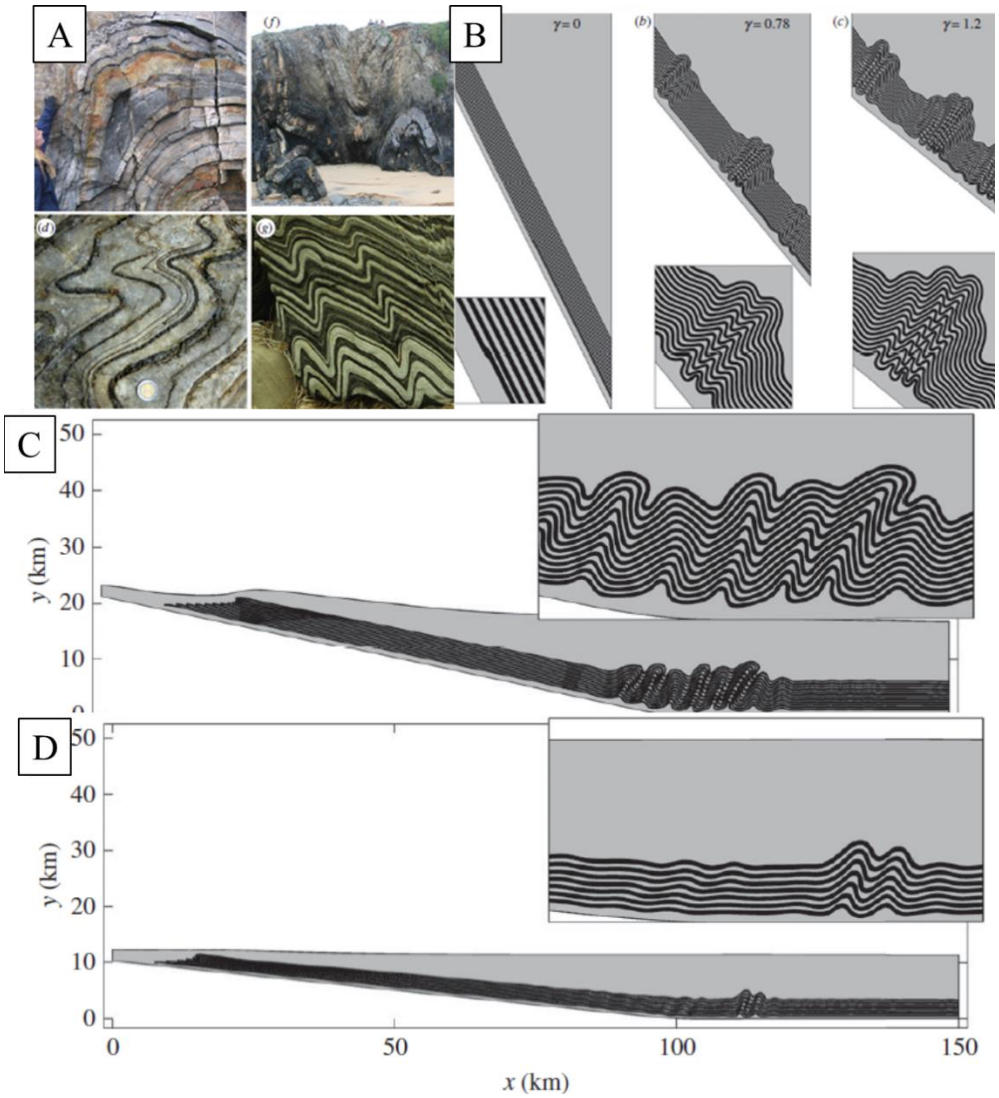

Fig. 4.12: (a) Examples of rock formations with shear-induced folding. (b) Simulation of viscous multilayers subjected to simple shear strain; folding size increases with increasing shear strain at location of local perturbation. (c, d) Simulation of viscous multilayers subjected to gravity sliding. Height of "hill" affects the size and orientation of the folds that are created at bottom of the "hill".

Another potential contribution to the heterogeneous microstructure evolutions observed in our study is that local regions may deform preferentially to other places around them, thus shielding them from deformation. This may be a result of the layer orientation relative to the shear direction, or a result of the HPT process, where samples do not always deform homogeneously, though these inhomogeneities are often localized at the geometric center and far edge of the HPT disc. For instance, as seen in Fig. 4.13, HPT of duplex stainless steel, with initial feature sizes

approximately ten to hundreds of microns, results in macroscale shear patterns that include vortices and swirls that are an effect of the HPT process [19, 20]. The S-shaped swirl in Fig. 4.13(b) at the center of the disc is also present in the current study and is partially the reason for the odd-shaped layer bending seen in Figs. 4.2 and 4.3 which are at or near the center of the disc. Because the localized instabilities due to the HPT process are localized at the center and edge, see locations B and C in Fig. 4.13(a), the results and discussion presented are still likely valid.

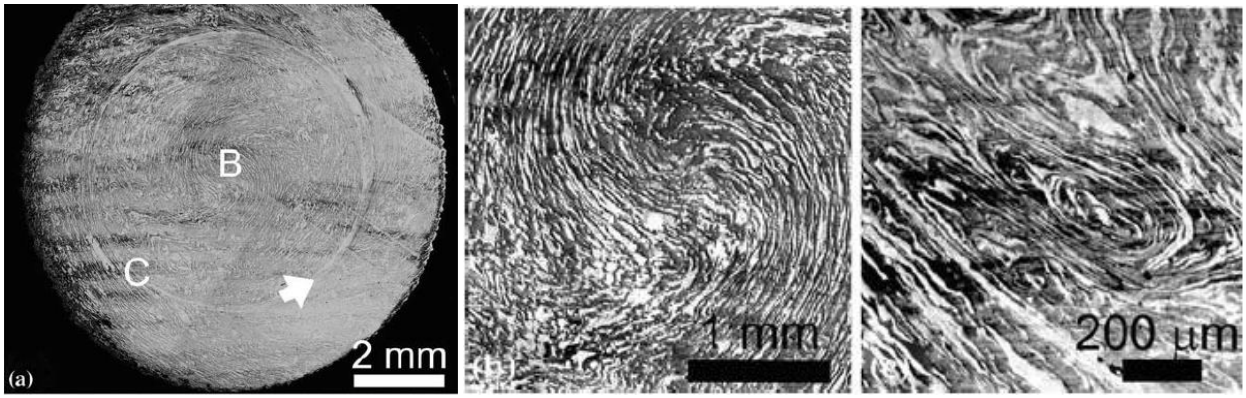

Fig. 4.13: (a) An optical image of the 5-revolution HPT disc of a duplex stainless steel with a two-phase microstructure with initial feature size on the order of tens of microns: a white arrow indicates a circular macroscopic shear strain track. (b) A magnified image of the central area marked B in (a). (c) A magnified image of the area marked C in (a) [20].

As mentioned previously, there are two regimes in which the multilayers deform under shear strain; the deformation mechanisms for layers oriented near-parallel to the shear direction have been thoroughly discussed. Now we will discuss the deformation mechanisms for layers oriented off-parallel to the shear direction. When layers are oriented this way, they deform more easily and are likely the reason a three-dimensional structure is formed. This is strongly consistent with molecular dynamics simulation that showed a direct correlation between shear mixing of Cu and Nb in {111}KS interfaces and the closeness with which the shear direction is oriented normal to the interface plane [6]. Layers are oriented off-parallel due to uneven stacking of film pieces, swirls formed by the HPT process, and kink and shear banding, the last of which is a deformation mechanism of shear parallel to the layers. These bent and kinked regions and regions where film

pieces are oriented non-parallel with each other create localized deformation of layers, resulting in the formation of an equiaxed, three-dimensional structure, as seen in the bright field TEM and Z-contrast STEM micrographs in Figs. 4.3(f), 4.4(d), and 4.5(c). The mechanism is visualized more clearly in Fig. 4.14 for Cu-Nb PVD-grown multilayers grown on Cu foil subjected to HPT. In (a), a kink band has formed bending the film, but the layers are still intact. However, as the kink band grows outward, the likelihood that the layers pinch off increases. This is seen in the boxed region in Fig. 4.14(b) as the layers have been completely shorn across the interface, and as the HPT strain increases, these pieces break away from the film entirely, as depicted in Fig. 4.14(c); though they do not deform further because the soft Cu foil deforms preferentially shielding the film pieces. In the present case where the sample disc is entirely from HPT Cu-Nb multilayers, the shorn layers are not shielded by a softer phase, but are likely partially shielded by the low shear strength of interfaces parallel with the shear direction. However, these off-parallel regions eventually deform further into a three-dimensional nanocomposite. It is reasonable that as the microstructure becomes three-dimensional in nature locally, the instability of nearby layers grows with increasing strain; therefore, large shear strains are needed to fully transform the multilayered structure into a three-dimensional nanocomposite, which happens in this study between a shear strain of ~357 and ~685. We note however that at this strain the steady-state microstructure is not likely reached at this strain as not all grains have an equiaxed morphology and there are remnants of the original layered structure even at a high strain of ~685, see Figs. 4.9(c) and 4.9(d) respectively. The fully transformed 3D microstructure has feature size of about 5-10nm, which is the same as Cu-Nb 50/50 materials subjected to HPT with the initial structure formed by ARB, high energy ball milling, and solid-solution growth by PVD [21, 22]; so the final steady-state

structure is independent of the starting structure, but the strain needed to get the steady-state structure is directly related to the starting morphology, length scale, and interface character.

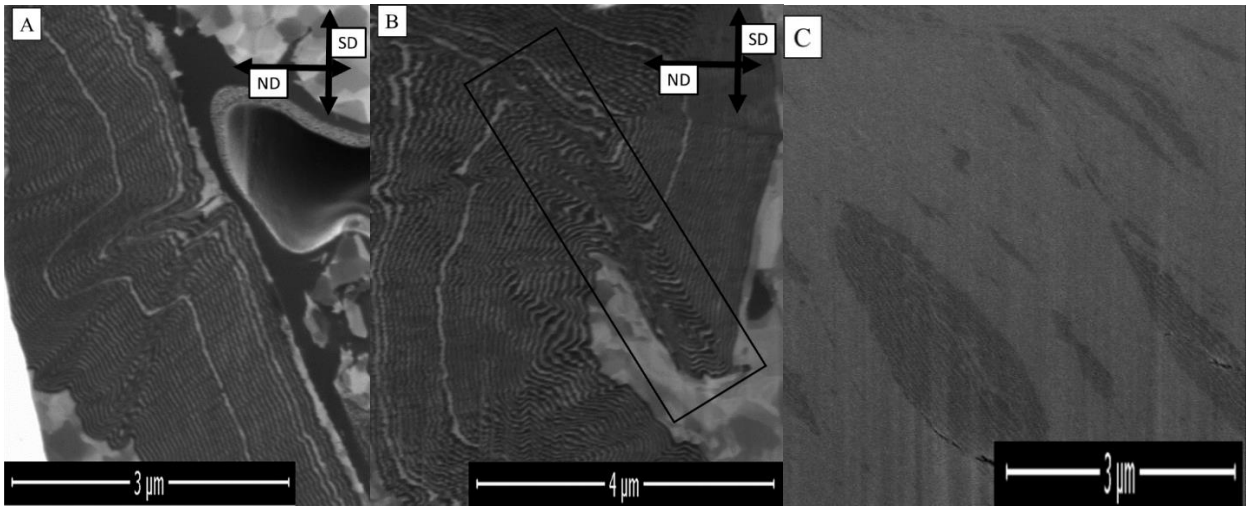

Fig. 4.14: SEM images of Cu-Nb multilayers grown on Cu foil subjected to HPT. Microstructure shows (a) multilayer kink banding, (b) layer pinch-off, and (c) film piece separation.

4.4 Conclusion

In this work, Cu-Nb multilayered nanocomposites with {111}KS interfaces were subjected to large shear strains using HPT at room temperature to investigate the role of interface character on the microstructural stability of the multilayered nanocomposites under severe simple shear strain. The samples were grown by PVD via magnetron sputtering, with a nominal layer thickness of 20 nm. The results were compared to previous HPT experiments on 18 nm thick Cu-Nb multilayered nanocomposites fabricated by ARB, with a dominant {112}KS interface character [9]. The only major difference between the PVD and the ARB materials is the interface character as the composition, morphology, and length scale are nearly identical. An important consequence of this interface character difference is that the interfacial shear strength is to be much lower in the PVD material at 300-550 MPa than in the ARB material at 1500 MPa [10]. As such, the PVD-grown material was expected to remain much more stable under simple shear strain than the ARB-fabricated material. It was observed by SEM, bright field TEM, and Z-contrast STEM imaging that the PVD-grown multilayers remain stable near parallel to the shear direction up to a shear strain of ~81 well above the strain to destabilize the ARB multilayers. Deformation in the PVD-grown multilayers is highly dependent on the orientation of the layers to the shear direction. Interfacial sliding, grain rotation and layer thickness reduction, and shear-induced kink and shear banding are the primary deformation mechanisms when the layers are oriented near-parallel to the shear direction. Interfacial sliding keeps the multilayered structure stable up to a higher strain than the ARB material, but the other mechanisms induce layer instabilities. These instabilities grow in size and change the orientation of the layers relative to the shear direction, thus making it easier for the layer to be sheared, eventually leading to a three-dimensional interconnected microstructure with reduced feature size. This final microstructure was observed to be similar to the steady-state

microstructure found in the ARB material subjected to HPT, further suggesting that the steady-state microstructure is independent of the initial starting condition. The findings in this study confirm that multiphase materials with low shear strength interfaces remain stable up to much higher shear strains than high shear strength interfaces. This is directly useful for structural applications where microstructural stability would be required to insure mechanical integrity. In addition, as will be discussed in the next chapter, these same interfaces serve as excellent sinks for defects created in radiation environments.

4.5 References

[1] I.J. Beyerlein, A. Caro, M.J. Demkowicz, N.A. Mara, A. Misra, and B.P. Uberuaga. *Materials Today* **16** (2013) 443.

[2] W. Han, M.J. Demkowicz, N.A. Mara, E. Fu, S. Sinha, A.D. Rollett, Y. Wang, J.S. Carpenter, I.J. Beyerlein, and A. Misra. *Advanced Materials* **25** (2013) 6975.

[3] S.N. Arshad, T.G. Lach, M. Pouryazdan, H. Hahn, P. Bellon, S.J. Dillon, and R.S. Averback. *Scripta Materialia* **68** (2013) 215.

[4] J.Y. Zhang, X. Zhang, R.H. Wang, S.Y. Lei, P. Zhang, J.J. Niu, G. Liu, G.J. Zhang, and J. Sun. *Acta Materialia* **59** (2011) 7368.

[5] I.J. Beyerlein, J.R. Mayeur, S. Zheng, N.A. Mara, J. Wang, and A. Misra. *Proceedings of the National Academy of Sciences* **11** (2014) 4386.

[6] N.Q. Vo, R.S. Averback, Y. Ashkenazy, P. Bellon, and J. Wang. *Journal of Materials Research* **27** (2012) 1621.

[7] N.Q. Vo, J. Zhou, Y. Ashkenazy, D. Schwen, R.S. Averback, and P. Bellon. *Journal of Materials* **65** (2013) 382.

[8] J. Zhou, R.S. Averback, and P. Bellon. *Acta Materialia* **73** (2014) 116.

[9] E. H. Ekiz, T.G. Lach, R.S. Averback, N.A. Mara, I.J. Beyerlein, M. Pouryazdan, H. Hahn, and P. Bellon. *Acta Materialia* **72** (2014) 178.

[10] N.A. Mara and I.J. Beyerlein. *Journal of Materials Science* **49** (2014) 6497.

[11] E. Vasco, C. Polop, and J.L. Sacedon. *Physical Review Letters* **100** (2008) 016102.

[12] R.G. Hoagland, J.P. Hirth, and A. Misra. *Philosophical Magazine* **86** (2006) 3537.

[13] J. Wang, A. Misra, R.G. Hoagland, and J.P. Hirth. *Acta Materialia* **60** (2012) 1503.

[14] E.H. Ekiz. Doctoral Dissertation: *Microstructural Evolution and Phase Stability of Cu-Nb Nanolaminates subjected to Severe Plastic Deformation by High Pressure Torsion* University of Illinois at Urbana-Champaign. (2014)

[15] M.G. Llorens, P.D. Bons, A. Griera, E. Gomez-Rivas, and L.A. Evans. *Journal of Structural Geology* **50** (2013) 209.

[16] J. Carreras, E. Druguet, and A. Griera. *Journal of Structural Geology* **27** (2005) 1229.

[17] S.M. Schmalholz and D.W. Schmid. *Philosophical Transactions of the Royal Society A* **370** (2012) 1798.

[18] G.W. Hunt, T.J. Dodwell, and J. Hammond. *Philosophical Transactions of the Royal Society A* **371** (2013)

[19] Y. Cao, M. Kawasaki, Y.B. Wang, S.N. Alhajeri, X.Z. Liao, W.L. Zheng, S.P. Ringer, Y.T. Zhu, and T.G. Langdon. *Journal of Materials Science* **45** (2010) 4545.

[20] Y. Cao, Y.B. Wang, S.N. Alhajeri, X.Z. Liao, W.L. Zheng, S.P. Ringer, T.G. Langdon, and Y.T. Zhu. *Journal of Materials Science* **45** (2010) 765.

[21] E.H. Ekiz. Doctoral Dissertation: *Microstructural Evolution and Phase Stability of Cu-Nb Nanolaminates subjected to Severe Plastic Deformation by High Pressure Torsion* University of Illinois at Urbana-Champaign. (2014)

[22] M. Wang. Doctoral Dissertation: *Severe Plastic Deformation in Highly Immiscible Cu Alloys* University of Illinois at Urbana-Champaign. (2014)

CHAPTER 5

ROLE OF INTERFACES ON TRAPPING HELIUM IN 2D AND 3D CU-NB NANOCOMPOSITES

5.1. Introduction

Immiscible metal nanocomposites have shown great promise for applications requiring materials with high resistance to radiation damage [1-3]. In particular, these nanocomposites have the ability to trap large amounts of point defects and He atoms at interfaces; however, the importance of interface character and microstructure to radiation damage tolerance has not been fully evaluated and quantified experimentally, thus impeding the design of materials with optimized radiation-tolerance. As previously discussed in Chapter 2, atomistic simulation and experiments suggest that interfaces play an important role in trapping point defects and He atoms, and therefore preserving microstructural stability [4]. One important result of the atomistic simulations is that interfaces with a large constitutional vacancy concentration, or free volume based on interface structure, are able to trap an exceptional concentration of He atoms before bubbles form. One such material is Cu-Nb multilayer nanocomposites with {111}KS interfaces. Experiments, by Demkowicz et.al [5], have shown that these interfaces do trap He at orders of magnitude greater concentrations than bulk pure metals. However, this work did not prove the trapping ability was necessarily a result of the interface character. Therefore, in this study, the He trapping ability of Cu-Nb nanocomposites with {111}KS interfaces was compared to that of Cu-Nb nanocomposites with {112}KS interfaces. Specifically we studied the damage tolerance and He trapping ability of PVD-grown Cu-Nb multilayers with {111}KS interfaces in comparison with bulk nanocomposites of Cu-Nb fabricated by accumulative roll bonding (ARB) with {112}KS interfaces [6-8]. As reviewed in Chapter 2, these materials are very similar as they have the same KS orientation relationship but with a different habit planes. The density of interface misfit

dislocation intersections in each material's habit plane is similar, but due to the different structure of the misfit dislocation intersections, the {112}KS interface does not contain significant amounts of localized excess free volume, or constitutional vacancies, compare to the {111}KS interface [4]. Nevertheless, recent studies have concluded that the ARB material has a trapping efficiency for point defects similar to that of the PVD-grown material [9, 10], and it has therefore been proposed that they will also be good traps for He. In addition to studying the role of interface character, we also investigated the role of morphology and interface area density on the trapping ability of Cu-Nb nanocomposites. Thus, we investigated the He trapping ability of three-dimensional Cu-Nb nanocomposites obtained imposing large shear strain via HPT on the Cu-Nb ARB material resulting in a 3D nanocomposite with more than five times the interfacial area density of the initial ARB material. Thus it is potentially more effective in trapping He on a volumetric basis than the 2D multilayer composites. We also study He trapping in these ARB/HPT samples but after heat treatment at 500 ˚C. The heat treatment reduces the total interface area due to coarsening, somewhat, but it also changes the interface structure. As we will show, this treatment has a very positive effect on the He trapping efficiency.

5.2 Results

The five sample sets investigated in this study include the ARB sample with an average individual layer thickness of 25 nm, two PVD-grown samples with 20 nm and 90 nm individual layer thicknesses, the ARB material that was subsequently processed by HPT, and this same HPT-processed material subsequently annealed at 500 ˚C for an hour. For each sample, under-focus and over-focus TEM micrographs were taken to determine the depths at which the first and last bubbles are visible. The widths of these regions were then compared to the He implantation profile from SRIM simulation. The critical He concentrations for bubble formation could then be obtained from the SRIM profile as the He concentration where the measured width of the bubble distribution equals the calculated width in the He implantation profile. The implant dose, the distance between the first and last visible bubbles, and the effectiveness for trapping He are collected in Table 5.1 for the five sample sets.

Table 5.1: The characteristics of each sample viewed in through-focus TEM. Error bars correspond to local variations in visibility range of He bubbles.

	Implant Dose (cm^{-2})	Visible He-filled Bubble Range (nm)	Critical He Concentration (He-nm^{-3})	Specific Interfacial Area (nm^{-1})	Interfacial He Storage Capacity (He-nm^{-2})
ARB	1.4×10^{17}	950 ± 165	0.06 ± 0.04	0.040	1.4 ± 1.0
ARB + HPT	1.4×10^{17}	580 ± 40	0.33 ± 0.06	0.30	1.1 ± 0.2
ARB + HPT + Annealed	1.6×10^{17}	555 ± 25	0.42 ± 0.08	0.075	5.8 ± 1.0
PVD – 20nm	1.6×10^{17}	600 ± 60	0.31 ± 0.12	0.050	6.4 ± 2.6
PVD – 90nm	0.8×10^{17}	730 ± 55	0.08 ± 0.02	0.011	7.0 ± 2.0

The PVD samples are the most efficient in terms of suppressing bubble formation per unit interfacial area. The ARB sample is significantly less efficient among the three 2D samples. It holds the least amount of helium before bubbles are visible, about five times less per unit interfacial area than that of the PVD samples. The qualitative differences in the bubble structure in the PVD

and ARB samples, however, appear small; for example, the bubble sizes and densities are similar in the regions where bubbles are observed and they preferentially form on interfaces. Fig. 5.1, specifically, shows under-focus and over-focus TEM micrographs of the PVD – 20 nm sample and the ARB (without HPT) sample near the deep end of the range where bubbles are observed. In both cases the bubbles are ≈ 1-2 nm in diameter. As seen on each image in Fig. 5.1, bubbles form at the interfaces and within the layers at the peak of the helium implant profile, but mostly at or near interfaces when the helium concentration is reduced. In these lower He concentration regions, bubbles "decorate" the Cu/Nb interfaces, forming on the Cu-side of the interface; similar behavior was reported in ref. [5]. The He bubble density within the Cu layers is higher than in Nb layers except at the highest He concentration, in which case the density is approximately the same in the two layers.

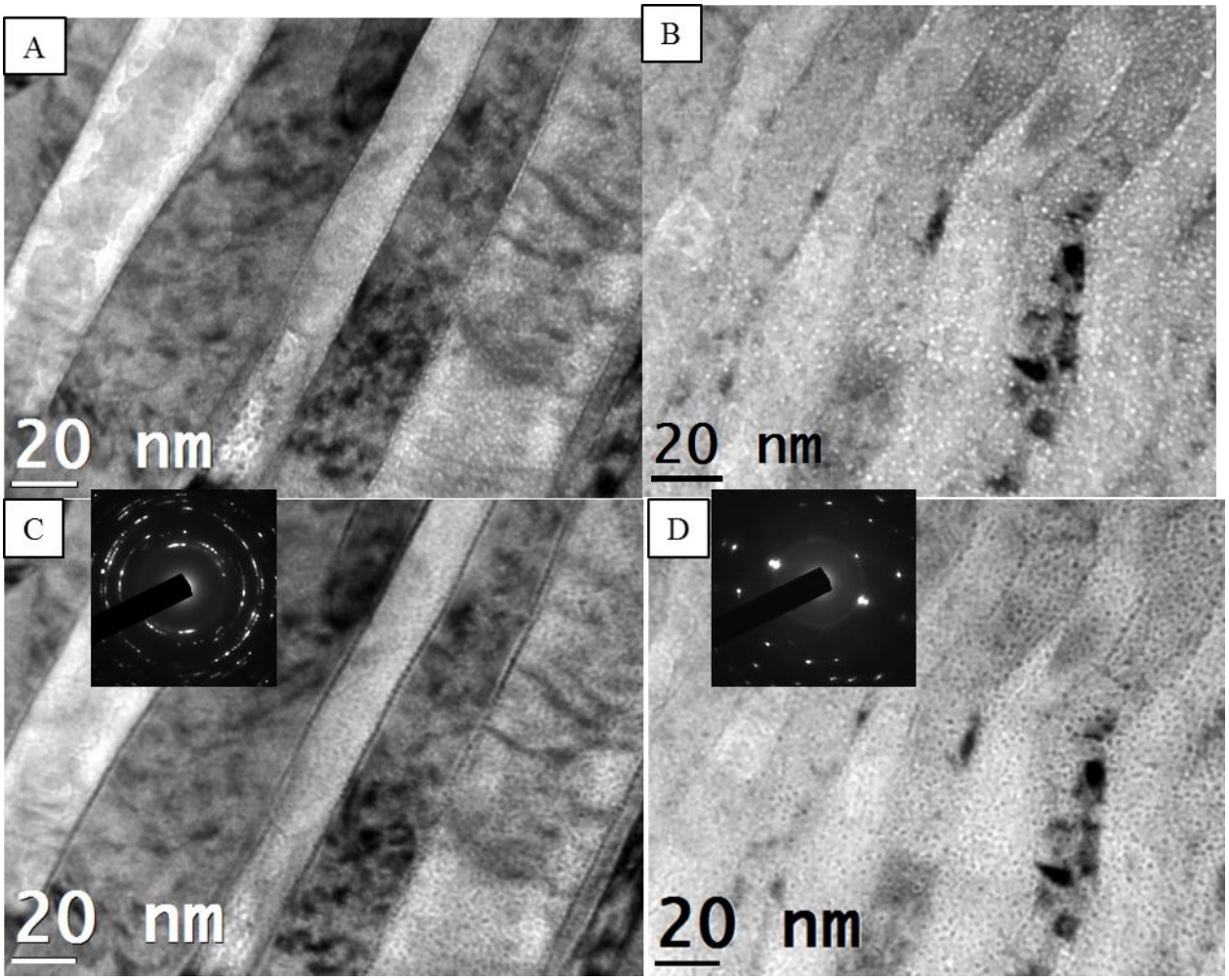

Fig. 5.1: Under-focus bright field TEM micrographs of (A) ARB sample and (B) PVD-20nm sample at deep end of visible bubble range. Sample surface and peak of implant profile is to the right. Images (C) and (D) are of the same regions in over-focus bright field TEM.

In the PVD-grown material with 90 nm individual layer thickness, the density of the ~1-2 nm diameter bubbles is approximately the same in both Cu and Nb layers as seen in Fig. 5.2. A difference with the thinner 20 nm sample is that it is evident that bubbles frequently form along the boundaries of the columnar grains of both Cu and Nb, which is best seen in the over-focus image in Fig. 5.2(b). This shows that grain boundaries also serve as good sinks for He atoms, particularly if the distance to an interphase boundary is beyond the diffusion distance of a He atom or point defect.

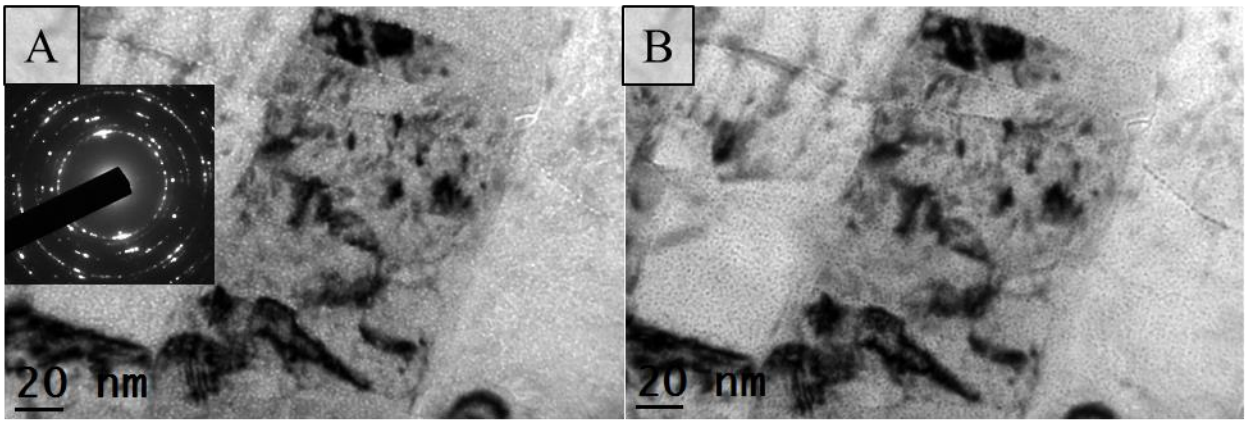

Fig. 5.2: (A) Under-focus and (B) over-focus bright field TEM micrographs of the PVD-90nm sample. Implanted surface is towards the bottom-right.

Fig. 5.3 shows the critical He concentration per unit volume as a function of specific interfacial area in PVD grown films. Here data from samples with 20 nm and 90 nm individual layer thicknesses are plotted together with data from ref. [5] for samples with much smaller layer thicknesses, 2.8 nm and 5.6 nm. The critical He concentration decreases inversely with layer thickness, and thus increases linearly with specific interfacial area. This finding agrees with the conclusion in ref. [5] that the critical He concentration per unit interfacial area does not depend on layer thickness. The current work extends this conclusion to much thicker films. This is significant since it demonstrates that for room temperature implantation He reaches the interfaces for layer thicknesses greater than 90 nm. This critical He concentration per unit area was determined from the slope of the linear fit of the present data, see Fig. 5.3, and the value of 6.25 He-nm^{-2} agrees well with that found in ref. [5], 8.5 ± 2.5 He-nm^{-2}.

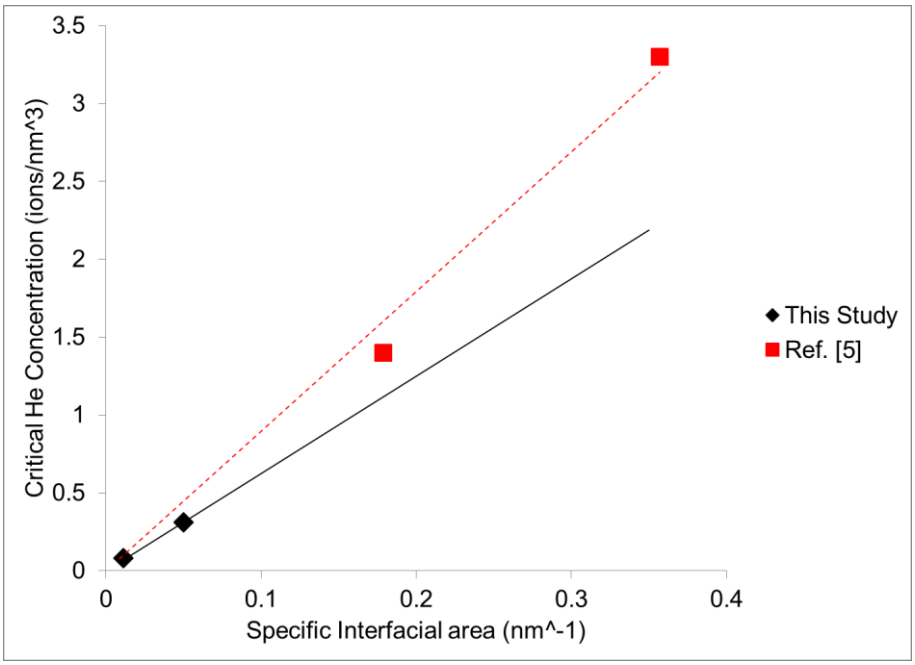

Fig. 5.3: Critical He concentration per volume as a function of specific interfacial area of samples with (111)KS orientation relationship; the samples with 0.18 nm^{-1} and 0.36 nm^{-1} specific interfacial area are from ref. [5].

The three-dimensional nanocomposite Cu-Nb sample obtained from the ARB material using HPT had a critical helium concentration per unit volume that was ~5 times larger than that of the untreated ARB material. The HPT treatment, however, also increased the interfacial area by a factor of 7.5 such that its critical interfacial efficiency is somewhat reduced from that of the as-prepared ARB materials, 1.1 He ions/ nm^2 compared to 1.4 He ions/ nm^2. The TEM micrographs in Fig. 5.4 show the region of the sample spanning from near the peak He concentration to the end of the visible range. Bubbles are clearly observed in Fig. 5.4(a) (under-focus) and Fig. 5.4(b) (over-focus), but the three-dimensional, interconnected nature of the microstructure prevents a definitive evaluation of whether the bubbles reside at interfaces or in the bulk. It is quite clear that the bubble density decreases quickly from the peak He concentration on the right to the end of range on the left.

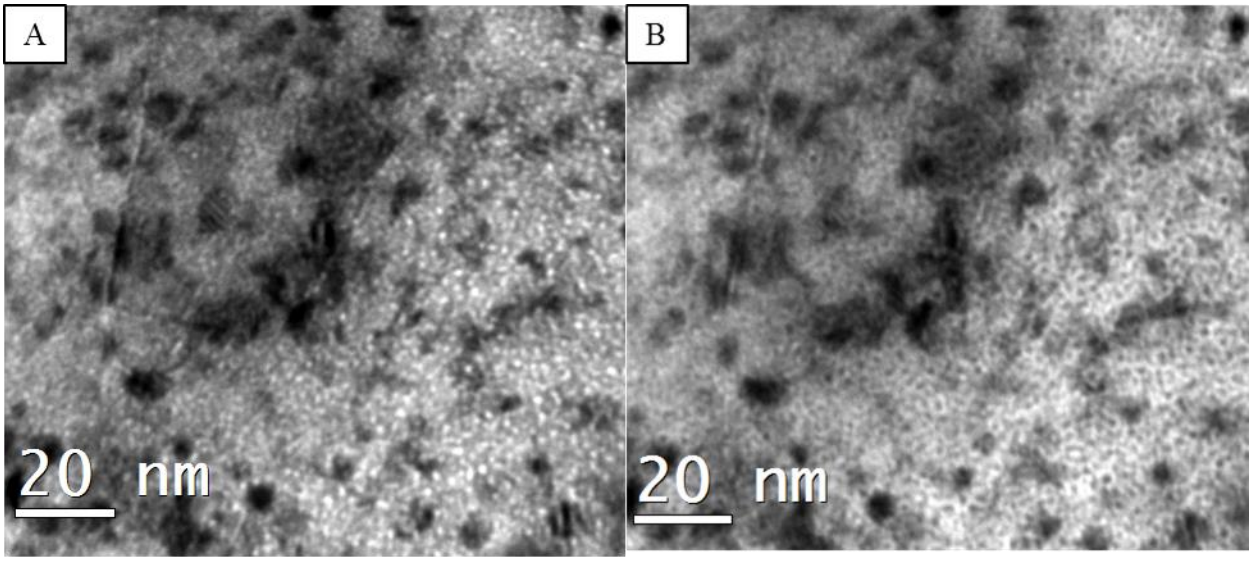

Fig. 5.4: (A) Under-focus and (B) over-focus bright field TEM micrographs of HPT sample with strain of ~2000. Implanted surface is towards the bottom-right. Due to the small interconnected three-dimensional nature, it is not possible to tell if bubbles form primarily at interfaces.

Annealing the HPT sample increased the grain size and decreased the specific interfacial area by a factor of ~ 4. The critical helium concentration, nevertheless, increased slightly. The TEM micrographs in Fig. 5.5 show the region at the peak He concentration and at the end of range in this sample. Again it is difficult to assess whether bubbles form predominantly at Cu/Nb interfaces, but in some locations there is a tendency to reside at boundaries; whether these are phase boundaries or grain boundaries is presently unknown.

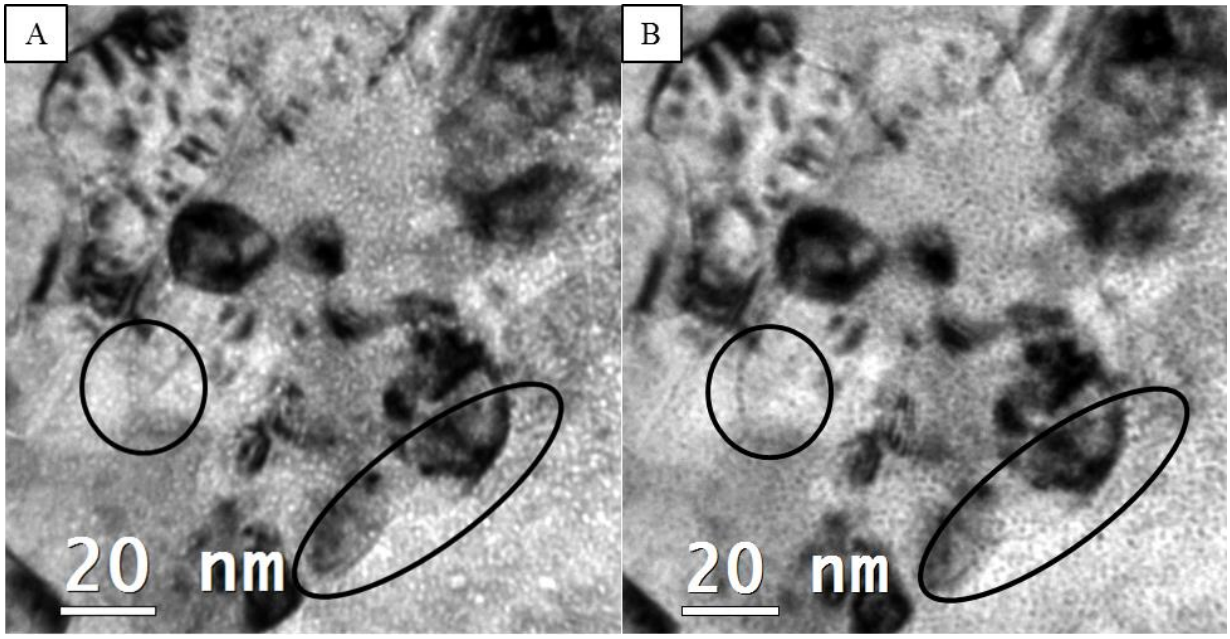

Fig. 5.5: (A) Under-focus and (B) over-focus bright field TEM micrographs of the HPT and annealed sample. Implanted surface is towards the bottom-right. In some regions, identified by circles, bubbles seem to "decorate" boundaries.

5.3 Discussion

Among the studied materials, He-storage capacity has a distinct dependence on both the type of interface and the quantity of interfacial area. This phenomenon is best represented by the HPT and PVD samples. Although the HPT sample is capable of storing large quantities of helium per unit volume, the interfaces are considerably less efficient in storing He than those of samples with effective interfaces such as the (111)KS , which the PVD samples possess.

To further illustrate the evidence provided, the bubble density distributions for the four differently treated samples are plotted together in Fig. 5.6. As can be seen in the plot, the distributions are asymmetric about the mean range, falling off faster at the deep end following the asymmetry of the helium implant profile, see Fig. 3.5. The asymmetry is most dramatic in the ARB sample. Each set is fitted with a quadratic fit, which shows that the HPT-annealed sample has the narrowest region of bubbles followed by the PVD – 20 nm sample and the HPT sample, and the ARB sample clearly has the widest range of bubbles. Furthermore the widths of the quadratic fits are very close to the range where bubbles are no longer seen, in table 5.1.

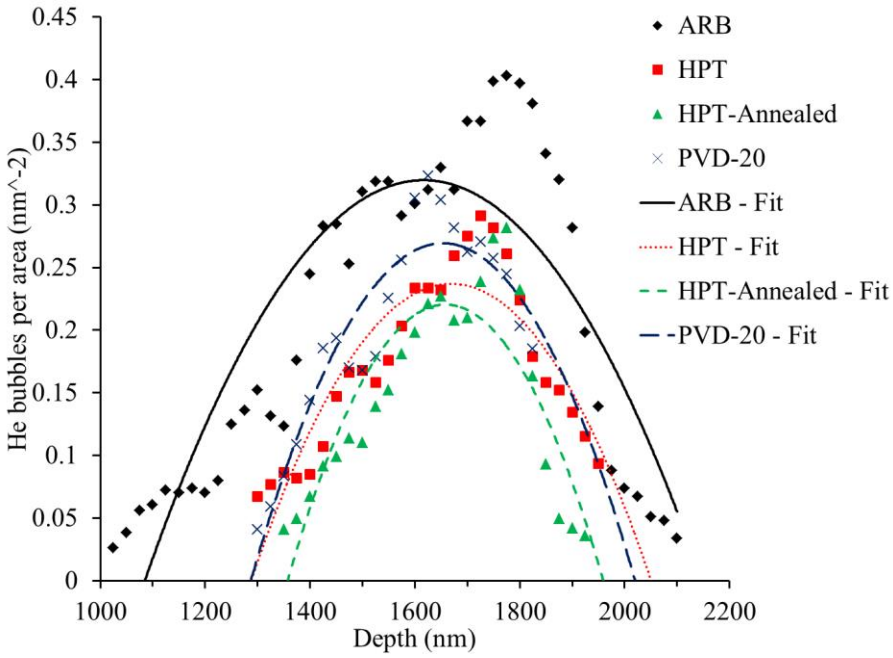

Fig. 5.6: Bubble density per area vs. depth. Polynomial fits for each sample set are indicated.

Bubbles form preferentially on the Cu-Nb interfaces of the ARB sample, which has dominant (112)FCC||(112)BCC habit plane, but this is not the best interface for trapping He atoms. Computer simulations have shown that the local structure where misfit dislocations intersect plays a very important role, and that it is different for the two interfaces, (111)KS and (112)KS [4]. The (111)KS interface has constitutional vacancy concentrations up to 5 at% in Cu-Nb, as opposed to zero in the (112)KS interface, and it is at these vacancies where He is strongly trapped [4]. It is thus reasonable that the PVD sample with (111)KS interfaces has a higher efficiency for trapping helium than the ARB sample of comparable layer thickness; consequently it suppresses bubble formation more effectively.

An important finding in this work is that three-dimensional nanocomposite Cu-Nb structures formed by SPD are also very effective in suppressing He bubble formation. In fact, the critical He concentration in the sample processed by HPT was over five times larger than the ARB sample with 25 nm individual layer thickness, and indeed comparable to the PVD sample with similar individual layer thickness. In the present experiment, the HPT samples were processed from the ARB samples, but we point out that the steady state microstructure of Cu-Nb during SPD is independent of its initial structure [11]. Thus, bulk nanocomposites of Cu-Nb with microstructures very similar to the ones investigated in this study can be obtained without the need for ARB. For example, samples prepared by ball milling followed by HPT, will have similar microstructures. A second important finding of this study is that the HPT sample retains its ability to suppress bubble formation, even after thermal annealing at 500 $^{\circ}$C. In this case some grain growth occurs, which leads to a reduction in specific interfacial area, but the interfacial storage capacity increases by nearly the same factor. This suggests that such materials can be employed for high temperature applications without loss of its ability to suppress He bubble formation.

In order to better understand He trapping in annealed HPT samples, texture analysis was performed on HPT samples annealed at 500 ˚C for 1 hour. By using a micro-beam XRD system, areas as small as 100 μm^2 were analyzed. This small spot size is important because the strain in our HPT samples varies linearly with radial position, to a maximum radius of only ≈ 4 mm. The procedures employed for texture measurements and analyses were reported elsewhere [6]. The results are displayed as orientation distribution functions (ODF) represented by three Euler angles ($\varphi_1, \Phi, \varphi_2$) in Bunge notation; the frequently used ODF sections $\varphi_2 = 0^o$ and $\varphi_2 = 45^o$ are displayed in Fig. 5.7. Common shear components for BCC and FCC metals are included for reference.

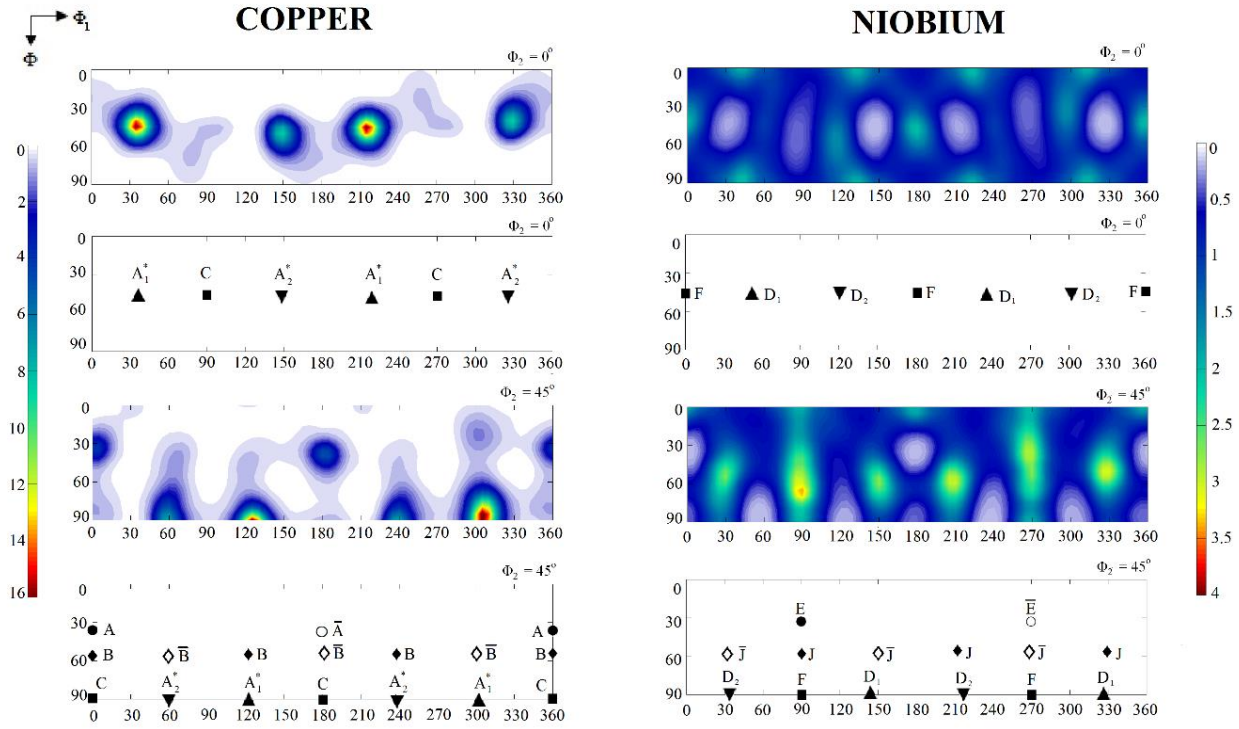

Fig. 5.7: ODF sections for Cu and Nb phases in the HPT and annealed sample for $\varphi_2 = 0^o$ and $\varphi_2 = 45^o$. Scale bars shown are in multiples of random distribution (min=0, max=16 for Cu and min=0, max=4 for Nb). Locations of common shear texture orientations are shown below each ODF section.

The present results are compared to the final texture reported previously on an as-deformed HPT sample [6]. The texture analysis of the annealed sample indicates an overall increase in

texture intensity compared to as deformed HPT sample, more significantly for Cu where the maximum intensity rose from about 4 times to about 16 times the random intensity. As seen in Fig. 5.7, copper texture developed a strong A-fiber texture with ND//{111}, where ND is the direction normal to the surface of the sample (i.e., parallel to the torsion axis during HPT). The main texture components present for Cu were the A_1^*/A_2^* components, corresponding to $(111)[11\bar{2}]$ and$(111)[\overline{11}2]$, and the $A/\bar{A}$ ones, corresponding to $(1\bar{1}1)[110]$ and $(111)[\overline{11}0]$.The texture intensity of Nb also increased after annealing, transforming from a nearly random texture in as-deformed HPT samples to the main texture components at $J//\bar{J}$, corresponding to $(110)[1\bar{1}2]$ and $(\overline{11}0)[\bar{1}1\bar{2}]$ and at $E/\bar{E}$, corresponding to $(110)[1\bar{1}1]$ and $(\overline{11}0)[\bar{1}1\bar{1}]$, followed by a weak F component corresponding to $\{110\} < 001 >$.

After annealing, the texture of the HPT sample, with predominantly (111)FCC||ND||(110)BCC, is consistent with the KS-relationship, although the three-dimensional phase co-existence at small scale prevented us from determining the dominant interface habit planes. Nevertheless, this texture change results in a 30% increase in the trapping efficiency of the sample, despite the ≈ 4 times decrease in interfacial area. The total processing of the ARB sample by HPT plus annealing thus leads to an increase in the critical He concentration by a factor of seven.

5.4 Conclusion

In this work, Cu-Nb nanocomposites of different interface character, morphologies, and feature size were implanted with He-ions to investigate and quantitatively compare the role of these characteristics in the irradiation damage tolerance and trapping ability of He atoms into nanoscale bubbles. Two-dimensional multilayer nanocomposites, PVD-grown with {111}KS interface character and ARB-fabricated with {112}KS interface character, were compared with three-dimensional nanocomposites fabricated by HPT of ARB multilayers. The type and orientation of the Cu-Nb interphase interface was shown to be of utmost importance. There is good agreement with previous research that the ability to store helium in PVD-grown samples with the {111}KS orientation relationship scales with layer thickness and is constant per interfacial area. The {111}KS interface, the preferred interface character in the PVD samples, compared favorably with the {112}KS interface in the ARB samples and the more random orientation relationship found in the HPT nanocomposites with shear texture, and the three-dimensional structured nanocomposites formed by HPT increase the amount of trapped He compared to the two-dimensional nanocomposites formed by ARB. This confirms experimentally that interfaces with a large constitutional vacancy concentration, such as in the {111}KS interface, serve as excellent sinks for defects, and large interface density is required to trap large amounts of He. Also, a sample with a reduced ability to store helium, such as the ARB sample, can be processed by severe plastic deformation using HPT and annealing to greatly improve the storage ability of the sample, or by using simpler methods such as ball milling of metal powders can be employed to form materials with improved defect trapping ability. This shows great promise for the design of bulk alloys to improve radiation damage tolerance and other structural properties that previously could only be achieved by thin film growth.

5.5 References

[1] K. Hattar, M.J. Demkowicz, A. Misra, I.M. Robertson, and R.G. Hoagland. *Scripta Materialia* **58** (2008) 541.

[2] E.G. Fu, A. Misra, H. Wang, L. Shao, and X. Zhang. *Journal of Nuclear Materials* **407** (2010) 178.

[3] K.Y. Yu, Y. Liu, E.G. Fu, Y.Q. Wang, M.T. Myers, H. Wang, L. Shao, and X. Zhang. *Journal of Nuclear Materials* **440** (2013) 310.

[4] M.J. Demkowicz and L. Thilly. *Acta Materialia* **59** (2011) 7744.

[5] M.J. Demkowicz, D. Bhattacharyya, I. Usov, Y.Q. Wang, M. Nastasi, and A. Misra. *Applied Physics Letters* **97** (2010) 161903.

[6] E. H. Ekiz, T.G. Lach, R.S. Averback, N.A. Mara, I.J. Beyerlein, M. Pouryazdan, H. Hahn, and P. Bellon. *Acta Materialia* **72** (2014) 178.

[7] S. Zheng, I.J. Beyerlein, J.S. Carpenter, K. Kang, J. Wang, W. Han, and N.A. Mara. *Nature Communications* **4** (2013) 1696.

[8] J. Wang, K. Kang, R.F. Zhang, S.J. Zheng, I.J. Beyerlein, and N.A. Mara. *Journal of Materials* **64** (2012) 1208.

[9] W. Han, M.J. Demkowicz, N.A. Mara, E. Fu, S. Sinha, A.D. Rollett, Y. Wang, J.S. Carpenter, I.J. Beyerlein, and A. Misra. *Advanced Materials* **25** (2013) 6975.

[10] W. Z. Han, N.A. Mara, Y.Q. Wang, A. Misra, and M.J. Demkowicz. *Journal of Nuclear Materials* **452** (2014) 57.

[11] M. Wang, R.S. Averback, P. Bellon, S.J. Dillon. Acta Materilia 62 (2014) 276.

CHAPTER 6

CONCLUSIONS AND FUTURE DIRECTION

This dissertation focuses on the investigation of the role interface structure in immiscible metal nanocomposites plays in deformation tolerance and radiation tolerance. Commonly in materials science, microstructure is one of the primary aspects of a material to change to affect properties; though as materials are processed to finer length scales down to the nanoscale, interfaces play a much larger role in a material's properties. Interface structure, just like microstructure, can vary within the same material system depending on the processing route; the properties of a material can also vary greatly depending on the interface structure. The role of interface structure on the tolerance to severe plastic deformation in Cu-Nb nanocomposites was investigated by comparing the microstructural evolution after high pressure torsion (HPT) of multilayer nanocomposites grown by physical vapor deposition (PVD) with low shear strength interfaces and fabricated by accumulative roll bonding (ARB) with high shear strength interfaces. And the role of interface structure on the trapping of He was studied by comparing He-bubble formation in nano-multilayers grown by PVD, nanolaminates fabricated by ARB, and three-dimensional nanocomposites obtained by high pressure torsion (HPT); each of these has a different preferred orientation relationship.

In the first aspect of this dissertation, Cu-Nb multilayered nanocomposites grown by PVD via magnetron sputtering, with a nominal layer thickness of 20 nm, which has the {111}KS interface character, were subjected to large shear strains using HPT at room temperature to investigate the role of interface character on the microstructural stability of the multilayered nanocomposites under severe shear strains. The results here were compared directly to previous HPT experiments on Cu-Nb multilayered nanocomposites fabricated by ARB, which has the

{112}KS interface character [1]. The only major difference between these materials is the interface character as the composition, morphology, and length scale are nearly identical. It was observed by SEM, bright field TEM, and Z-contrast STEM imaging that the PVD-grown multilayers, with low shear strength interfaces, largely remained stable up to a shear strain of ~81, and flat layers were still present up to a strain of ~357, a much greater strain needed to destabilize the layers than the ARB multilayers with high shear strength interfaces. Deformation mechanisms in the PVD-grown multilayers depended strongly on the orientation of the layers with respect to the shear direction. When the interfaces are near-parallel to the shear direction, the layers deformed primarily by interfacial sliding, grain rotation and layer thickness reduction, and shear-induced kink or shear banding. Interface sliding was likely present up to a strain of ~81 before the layer thickness was reduced and texture changed. Simultaneously, local plasticity of the multilayers was induced by kink or shear banding resulting in large bends and foils in the film pieces. The latter layer instability along with improperly stacked film pieces oriented the layers off-parallel to the shear direction. At this orientation, the interface was easier to shear, thus the layered structure was broken apart and gradually changed into a three-dimensional interconnected microstructure with reduced feature size. This final microstructure was observed to be similar to the steady-state microstructure found in the ARB material subjected to HPT, further suggesting that the steady-state microstructure is independent of the initial starting condition. However, the strain required to reach steady-state largely depends on the initial composition, morphology, feature size, and lastly based on this study, interface character. The findings in this study confirm that multiphase materials with low shear strength interfaces remain stable up to much higher shear strains than high shear strength interfaces. This is directly useful for structural applications, such as in nuclear power plant materials, that require microstructural stability to keep mechanical integrity. In

addition, these same interfaces serve as excellent sinks for defects created in radiation environments, as discussed below.

In the second aspect of this dissertation, Cu-Nb nanocomposites of different interface character, morphologies, and feature size were implanted with He-ions to investigate and quantitatively compare the role of these characteristics in the irradiation damage tolerance and trapping ability of He atoms into nanoscale bubbles. Both two-dimensional and three-dimensional Cu-Nb nanocomposites, regardless of interface character, were shown to be good traps for He atoms. However, multilayer nanocomposites with {111}KS interfaces trapped more He at interfaces than the nanocomposites with predominantly {112}KS interfaces; a similar trend that was shown for the interfaces subjected to shear strain. While the interface character of the multilayers was of great importance in trapping defects, the large interface density in the three-dimensional nanocomposites also trapped a large amount of He before bubbles formed because the interface area was increased by more than a factor of five from the multilayer nanocomposites. These results confirm experimentally that a high density of efficient interfaces, such as the {111}KS interfaces with high constitutional vacancy concentration, serve as excellent sinks for defects and He atoms. However, nanocomposites with a reduced ability to store He, such as the ARB sample, can be processed further by severe plastic deformation to greatly improve the storage ability of the sample, or by using simpler methods such as ball milling of metal powders can be employed to form materials with improved defect trapping ability.

The results of both high shear strain using HPT and radiation damage using He implantation indicate that the (111)FCC||(110)BCC Kurdjumov-Sachs (KS), or {111}KS, interfaces predominant in PVD provide more effective traps for both point and line defects than the {112}KS interfaces predominant in ARB nanolaminates. These results show promise for

designing the interface structure of materials to improve radiation and deformation tolerance. The steady-state microstructural stability, good trapping efficiency, and high interface area of 3D structures processed by severe plastic deformation provide evidence that there is great potential for the design of bulk alloys to improve radiation damage tolerance and mechanical structural properties that previously could only be achieved by thin film growth.

Beyond the relatively small scope changes that could be done to optimize the results presented here, such as performing HPT on one Cu-Nb multilayer film grown to more than 100 μm, this research could continue in several directions. Applying what has been learned to steels, it could be interesting to investigate and quantify the role of interfaces and interface structure on the effects of high shear strain and ion irradiation within duplex stainless steels, ferritic/martensitic steels, and oxide dispersion strengthened steels [2, 3]. These materials are used in current reactor environments and in proposed future reactor components; it could be interesting to investigate the role of these interfaces in their response to these conditions, especially as the interfaces are structurally semi-coherent to incoherent, but the phases are only moderately immiscible for the duplex steels and F/M steels [4]. Looking beyond the FCC-BCC systems, current research is being conducted on the accumulative roll bonding of BCC-HCP interfaces like those in Nb-Zr composites [5]. These materials behave differently under ARB than FCC-BCC interfaces like Cu-Nb – in that they respond similarly to the bulk pure metal counterparts; it would be interesting to study their response to large shear strain and ion irradiation in these materials.

6.1 References

[1] E. H. Ekiz, T.G. Lach, R.S. Averback, N.A. Mara, I.J. Beyerlein, M. Pouryazdan, H. Hahn, and P. Bellon. *Acta Materialia* **72** (2014) 178.

[2] S.J. Zinkle and L.L. Snead. *The Annual Review of Materials Research* **44** (2014) 241.

[3] J. Brodrick, D.J. Hepburn, and G.J. Ackland. *Journal of Nuclear Materials* **445** (2014) 291.

[4] S.M. Gonzalez de Vincente, S. Dudarev, and M. Rieth. *Fusion Science and Technology* **66** (2014) 38.

[5] J.S. Carpenter, T. Nizolek, R.J. McCabe, M. Knezevic, S.J. Zheng, B.P. Eftink, J.E. Scott, S.C. Vogel, T.M. Pollock, N.A. Mara, and I.J. Beyerlein. *Acta Materialia* **92** (2015) 97.

Published Works

The results found in this dissertation have in part been published in peer-reviewed journals:

T.G. Lach, E.H. Ekiz, R.S. Averback, N.A. Mara, and P. Bellon. "Role of Interfaces on the Trapping of He in 2D and 3D Cu-Nb Nanocomposites." *Journal of Nuclear Materials* **466** (2015) 36.

S.N. Arshad, T.G. Lach, J. Ivanisenko, D. Setman, P. Bellon, S.J. Dillon, and R.S. Averback. "Self-organization of Cu-Ag during Controlled Severe Plastic Deformation at High Temperatures." *Journal of Materials Research* **30** (2015) 1943.

E.H. Ekiz, T.G. Lach, R.S. Averback, N.A. Mara, I.J. Beyerlein, M. Pouryazdan, H. Hahn, and P. Bellon. "Microstructural Evolution of Nanolayered Cu-Nb Composites subjected to High Pressure Torsion." *Acta Materialia* **72** (2014) 178.

S.N. Arshad, T.G. Lach, M. Pouryazdan, H. Hahn, P. Bellon, S.J. Dillon, and R.S. Averback. "Dependence of Shear-Induced Mixing on Length Scale." *Scripta Materialia* **68** (2013) 215.